UNIVERSIDADE DO ALGARVE

Faculdade de Ciências e Tecnologia

SELF-ASSEMBLED NANOPARTICLES AS NEW SMART CONTRAST AGENTS FOR MAGNETIC RESONANCE IMAGING

Teresa Fragoso Rocheta Simão

Master's Degree in Biomedical Sciences

Faro, Portugal

2010

UNIVERSIDADE DO ALGARVE

Faculdade de Ciências e Tecnologia

SELF-ASSEMBLED NANOPARTICLES AS NEW SMART CONTRAST AGENTS FOR MAGNETIC RESONANCE IMAGING

Teresa Fragoso Rocheta Simão

Master's Degree in Biomedical Sciences

Project and thesis supervised by:

Fouzi Mouffouk, Ph.D (CBME, IBB)

Nuno Rodrigues dos Santos, Ph.D (CBME, IBB)

Faro, Portugal

2010

*"*The secret of getting ahead is getting started. The secret of getting started is breaking your complex, overwhelming tasks into small manageable tasks, and then starting on the first one.*"*

Mark Twain

Dissertação de Candidatura ao Grau de Mestre em Ciências Biomédicas

Área de Bionanotecnologia pela Universidade do Algarve

MSc Thesis in Biomedical Scienses

Area of Bionanotechnology by the Universidade do Algarve

As opiniões expressas nesta publicação são da exclusive responsabilidade do seu autor

The contents of this dissertation are of the exclusive responsibility of the author

(Teresa Fragoso Rocheta Simão)

ACKNOWLEDGEMENTS

The work described in this thesis would have been almost impossible without the support and help of many people.

First, I would like to express my gratitude to my supervisors, Dr. Fouzi Moffouk and Dr. Nuno Rodrigues dos Santos. Thanks to Dr. Fouzi Mouffouk for the opportunity to work in this great project, for teaching me and trust in my capabilities to perform this task. Thanks to Dr. Nuno Rodrigues dos Santos for receiving me in his laboratory, for being such a dedicated professor, with who I learned so much, thanks to patiently listen to my ideas and doubts, to advice, assist and support me all over this work.

A special thank you to Dr. Ana Costa, for being present whenever I needed, for gently teaching and conducting me during this work.

Thanks to Dr. Ana Grenha, Dr. Gabriela Silva and Dr. Álvaro Tavares for being always there and to supply me so many precious informations.

To my lab colleagues, Mónica Fernandes, Marinella Ghezzo and Ricardo Silva, thanks so much for sharing their knowledge, for their friendship, company and for always supporting me. Thanks to everyone at Dr. Guilherme Ferreira's, Dr. José Belo's and Dr. Ana Grenha's laboratories for their suggestions and for helping me every time I needed.

Thanks to my work colleagues for several schedule shifts, support and friendship.

To all my friends, special tanks for their encouragement to continue and also for their companionship. I salute them for understanding and forgiving my lack of time to be with them.

Lastly, I am very grateful to my parents and sister for being always a constant and unconditional source of support, affection, patience and understanding.

Thank you very much to everyone!

Teresa Simão

ABSTRACT

The aim of this thesis is to develop smart and targeted nanoparticle contrast agents for Magnetic Resonance Imaging. These nanoparticles were designed to improve the sensitivity of this high resolution imaging technique and thereby improve early cancer detection, which is a major factor for the reduction of cancer mortality. The designed nanoparticles are expected to accumulate in the tumor through passive and active targeting. In addition, when exposed to the characteristic low pH of the cancer microenvironment, the nanoparticles will release the contrast agent, which will turn on its imaging capability. This contrast agent consists of pH-sensitive polymeric micelles formed by self-assembly, loaded with Gadolinium (III) complexes and bioconjugated with the C595 monoclonal antibody against the human MUC1 protein, which is overexpressed during tumorigenesis since its early stages.

The capability of micelles to disintegrate and release the encapsulated contrast in acidic conditions was proved by 1.5T MRI experiments. The MRI study showed no image signal from the sample with intact micelles whereas a signal enhancement was observed from the sample at low pH. After one mouse has been intramuscularly injected with Gadolinium(III)-loaded micelles in both hind legs, the MR image demonstrated a stronger signal from the right hind leg, which was previously injected with an acid solution. To assess *in vitro* cytotoxicity of free and encapsulated Gadolinium (III) complexes in polymeric micelles, MTT assays were performed on different cancer cell lines. Encapsulated Gadolinium (III) complexes showed significantly lower cytotoxicity than free Gadolinium (III) complexes, even at the highest concentration. To verify the target capability of nanoparticles, fluorescent dye-loaded polymeric micelles were incubated with breast cancer cells expressing MUC1 (verified by semi-quantitative RT-PCR, Western blotting and flow cytometry) and mouse bone marrow stroma cells. Antibody-conjugated micelles had superior affinity for MUC1-expressing human breast cancer cells than for mouse bone marrow cells.

Key words

Smart contrast agent; Magnetic Resonance Imaging; Nanoparticles; Amphiphilic diblock copolymers; Mucin-1

RESUMO

A presente Tese de Mestrado aborda a criação e síntese de um agente de contraste "inteligente" para imagiologia por Ressonância Magnética.

A Ressonância Magnética (RM) é uma técnica de imagem médica que apresenta excelente resolução espacial e contraste entre tecidos diferentes. No entanto, por vezes a resolução de contraste não é suficiente para demonstrar alterações patológicas no mesmo tecido, especialmente quando as alterações ainda só estão presentes a nível celular e molecular. Para aumentar a sensibilidade desta técnica de imagem e potenciar a sua aplicação ao nível da imagem molecular desenvolveram-se nanopartículas com agente de contraste, específicas para detectar cancro.

Este agente de contraste "inteligente" é constituído por polímeros anfifílicos, sensíveis ao pH, que por *self-assembly* se organizam formando micelas. Estas, devido à característica particular do polímero que as forma, irão responder, desintegrando-se e libertando o seu conteúdo que consiste em quelatos de gadolínio (III) hidrofóbicos, exclusivamente perante ambientes com valores de pH relativamente ácidos, permanecendo intactas noutros meios. Enquanto o meio de contraste estiver encapsulado no centro hidrofóbico das micelas, elas restringem o acesso das moléculas de água ao quelato de gadolínio, o que impede a interacção dos protões da água com o ião metálico. Assim, não há diminuição do tempo de relaxação longitudinal (T_1) das moléculas de água circundantes. Pretende-se, por isso, utilizar o pH extracelular relativamente ácido dos tecidos tumorais como despoletador específico da desintegração destas micelas e assim permitir que os quelatos de gadolínio aumentem o contraste da imagem de RM unicamente nestas situações. Esta diminuição localizada e específica do pH verifica-se desde as fases mais precoces do desenvolvimento tumoral, principalmente devido ao aumento da taxa de glicólise aeróbica das células cancerígenas.

As micelas foram bioconjugadas com um anticorpo monoclonal, C595, contra a proteína Mucina-1 (MUC1) humana. Esta proteína tem um papel importante no desenvolvimento de certos tipos de cancro, demonstrando alterações relativamente aos seus níveis de expressão e localização na superfície celular, assim como no seu grau de glicosilação, desde as primeiras alterações tumorais verificadas ao nível da célula. Com esta abordagem, pretende-se tornar mais específica e intensa a acumulação deste tipo de

partículas em tecidos cancerígenos, que ocorre devido à arquitectura vascular anómala, caracterizada por amplos espaços entre as células endoteliais. A referida acumulação de nanopartículas em tecidos tumorais é devida à sua dimensão reduzida que lhes permite extravasar pelos espaços endoteliais aumentados, à drenagem linfática ineficaz dos tecidos tumorais e ao longo tempo de permanência na circulação sanguínea que aumenta a probabilidade e a frequência do extravasamento.

Utilizaram-se quelatos de gadolínio como agente de contraste, pois o contraste positivo produzido por este ião paramagnético em imagens de RM ponderadas em T_1 é mais fácil de assinalar que o contraste negativo induzido pelos contrastes superparamagnéticos em imagens ponderadas em T_2. A quantidade relativamente elevada de quelatos de gadolínio encapsulada nas micelas, a retenção e acumulação destes transportadores na lesão tumoral vão aumentar a concentração local do meio de contraste. Este fenómeno resultará numa amplificação da intensidade de sinal emitida pela lesão tumoral, o que aumenta a sensibilidade para a sua detecção, mesmo quando apenas existe um número limitado de células alteradas. Enquanto se aumenta a biodisponibilidade local do meio de contraste, diminui-se a concentração total de contraste necessária para a obtenção de imagens com acuidade diagnóstica.

Mediante o descrito, este trabalho foi desenvolvido com o intuito de testar o mecanismo de resposta das micelas à diminuição do pH, de perceber se os quelatos de gadolínio hidrofóbicos produziam um aumento de contraste em imagens de RM compatíveis com aplicação clínica, de testar a toxicidade *in vitro* dos quelatos de gadolínio livres ou encapsulados nas micelas e de avaliar a especificidade deste novo sistema para as células-alvo. Para este fim sintetizaram-se micelas com complexos de gadolínio, micelas com o fluoróforo 1-metilpireno encapsulado e micelas bioconjugadas com o anticorpo anti-MUC1 e com fluoróforo encapsulado. As nanopartículas foram caracterizadas por Dispersão Dinâmica de Luz (DLS). A distribuição de tamanho mostrou que as micelas com 1-metilpireno encapsulado têm cerca de 24 nm de diâmetro. Obtiveram-se curvas de calibração para os quelatos de gadolínio e para o fluoróforo para se estimar a concentração total de cada um dos compostos numa dada suspensão de micelas. Demonstrou-se a capacidade destas micelas para se desintegrarem em pH ácido e libertarem o agente de contraste através da aquisição de imagens de duas amostras com micelas com meio de contraste encapsulado e com diferente pH, num equipamento de RM de 1.5 T. Outra experiência semelhante foi realizada, através da injecção intramuscular de micelas com meio de contraste

encapsulado em ambos os membros posteriores de um ratinho. Sendo que, previamente havia sido injectado uma solução ácida no membro posterior direito. As imagens da primeira experiência demonstraram um aumento da intensidade do sinal proveniente da amostra com pH baixo, enquanto a amostra com pH neutro não demonstrou qualquer alteração de sinal relativamente ao meio envolvente. Relativamente à segunda experiência, verificou-se que a intensidade do sinal proveniente do membro direito era superior à do no membro esquerdo. A citotoxicidade dos complexos de gadolínio foi observada *in vitro* através de ensaios de MTT em diferentes linhas celulares de cancro. Verificou-se que a encapsulação dos complexos de gadolínio nas micelas diminuiu significativamente a sua toxicidade comparativamente com o complexo livre. O valor de IC_{50} para estes quelatos de gadolínio variou entre 10.2 e 12.8 μM consoante a linha celular em estudo. As experiências de verificação da especificidade das micelas bioconjugadas com C595 para linhas celulares de carcinoma mamário que expressavam MUC1 foram realizadas através de citometria de fluxo e microscopia de fluorescência. As micelas tinham 1-metilpireno encapsulado para facilitar a sua observação por ambos os métodos. Utilizaram-se como controlo células estromais da medula óssea de ratinho. Observou-se que as partículas conjugadas ao anticorpo mostraram maior afinidade para as células que expressavam MUC1 do que as partículas sem anticorpo. A expressão de MUC1 nas linhas celulares utilizadas foi comprovada através de RT-PCR semi-quantitativo, PCR em tempo real, Western blotting e citometria de fluxo.

Os resultados obtidos demonstraram que estas micelas têm potencialidade para ser utilizadas em RM como agente de contraste, pois, relativamente aos agentes de contraste actualmente utilizados, combina a capacidade de acumular passivamente (devido à dimensão) e activamente (devido à bioconjugação com o anticorpo) em tumores que expressem a proteína MUC1. Além disso, possibilita a amplificação do sinal da imagem de RM em microambientes com pH relativamente ácido, que são habitualmente característicos de lesões cancerígenas.

Palavras-chave

Agente de contraste inteligente; Imagiologia médica; Nanopartículas; Polímeros dibloco anfifílicos; Mucina-1

TABLE OF CONTENTS

LIST OF FIGURES

LIST OF TABLES

LIST OF ABBREVIATIONS

CA	contrast agent
CT	cytoplasmic tail
CTA	chain transfer agent
DCE	dynamic contrast enhancement
DCIS	ductal carcinoma *in situ*
DMF	N,N-Dimethylformamide
DLS	dynamic light scattering
DOTA	1,4,7,10-tetraazacyclododecane-1,4,7,10-tetraacetic acid
DTPA	diethylenetriaminepentaacetic acid
DTPA-BMA	{bis-[2-(carboxymethylmethylcarbamoylmethylamino)ethyl]amino} acetic acid
EGFR	epidermal growth factor receptor
EPR	enhanced permeability and retention
ER	estrogen receptors
Gd (III)	gadolinium ion
HER2	human epidermal growth factor receptor 2
HP-DO3A	1,4,7,10-tetraazacyclododecane-1-hydroxypropyl-4,7,10-trisacetic acid
HPMA	N-(2-hydroxypropyl)methacrylamide
IC_{50}	inhibitory concentration that reduces cell viability by 50%
IDC	invasive ductal carcinoma
LIN	lobular intra-epithelial neoplasia
LMWCA	low molecular weight contrast agent
MAb	monoclonal antibody
MMWCA	macromolecular weight contrast agent
MR	magnetic resonance
MRI	magnetic resonance imaging
MTT	3-(4, 5-dimethylthiazol-2-yl)-2, 5-diphenyl tetrazolium bromide
NMR	^{1}H Magnetic Resonance
OD	optical density

PBS	phosphate-buffered saline
PBST	phosphate-buffered saline/0.1% Tween 20
PD	proton density
PEG	poly (ethylene glycol)
PR	progesterone receptors
RAFT	reversible addition-fragmentation chain transfer
RES	reticuloendothelial system
RF	radiofrequency
SPIO	superparamagnetic particles of iron oxide
T	Tesla
TE	echo time
TEM	transmission electron microscopy
THF	tetrahydrofuran
TR	repetition time
T_1WI	T_1-weight image
T_2WI	T_2-weighted image
UV	ultraviolet

Symbol	Definition
A	UV-Vis absorption
$\boldsymbol{B_0}$	external magnetic field
$\boldsymbol{M}$	net magnetization vector
$\mathbf{T_1}$	longitudinal magnetization time
$\mathbf{T_2}$	transversal relaxation time

CHAPTER I: INTRODUCTION

1. NANOTECHNOLOGY

Nanotechnology has emerged in the last few years as a new multidisciplinary scientific field, which not only benefits from but also has an impact on such diverse domains as chemistry, physics, electronics, optics, energy, materials science, space technology and biomedicine (Porter & Youtie, 2009; Choi & Baker, 2007). Nanoscience offers the exceptional possibility to produce nanoscale devices with approximately 1–100 nm and containing multiple integrated properties (Liu, Kiessling, & Gatjens, 2010; Yezhelyev, Gao, Xing, Al-Hajj, Nie, & O'Regan, 2006).

1.1. NANOPARTICLES IN MEDICINE

Great progress has been made regarding nanomaterial applications to medicine. These compounds have not only been tested in *in vitro* experiments but also been applied clinically (Tiefenauer, 2007). The development of this research area will provide extraordinary opportunities for future individualized diagnostic strategies and therapeutic approaches for humans (Liu et al., 2010).

Nanoparticles are complex compounds made of multiple molecules and polymers that may present single or multiple functions (Bulte & Modo, 2008). They have been developed as contrast agents for medical imaging, for therapeutic applications such as target carriers for drug controlled release and for gene delivery (Kairemo, Erba, Bergström, & Pauwels, 2008; Peer et al., 2007).

An area under intensive research is the application of nanoparticles for molecular imaging (Young-wook, Jae-Hyun, & Jinwoo, 2007). Molecular imaging is an interdisciplinary research field, which covers chemistry, biology, pharmacology, and medicine, aiming to detect early, to visualize and to characterize physiological and disease processes *in vitro* and *in vivo* (Weissleder & Mahmood, 2001). This application provides valuable clinical information to help guiding therapy against a variety of diseases, such as cancer (Mankoff, 2007). The issue of early cancer diagnostics has been the object of much research. Several types of nanoparticles with variable characteristics have been engineered to optimize cancer detection through noninvasive imaging modalities, such as magnetic resonance imaging (MRI), computed tomography, ultrasound, positron emission tomography, single photon emission computed tomography and near-infra-red fluorescence imaging (Weissleder, 2002).

Critical features for successful preparation and application of nanoparticles to biological environments are reproducibility of synthesis method, creation of well-defined nanoparticles with monodispersity populations, low immune system reactions and reduced cytotoxicity and elimination from the biological system (Choi & Baker, 2007). Novel challenges have also emerged, such as the elimination of nonspecific uptake of nanoparticles by macrophages and other cells of the reticuloendothelial system (RES); the development of more specific nanoparticles that target just molecules of interest, and the design of particles small enough to penetrate endothelial barriers (blood-brain barrier and dermal tight junctions). At the same time, nanoparticles should be able to maintain long-circulating blood half-lives, allowing accumulation at the target location and release of their contents to get a localized high drug/contrast agent (CA) concentration with far less systemic effects. Another new approach is the use of diagnostic "smart" agents that behave as sensors and act in response to several biological phenomena (Bulte & Modo, 2008; Kairemo et al., 2008).

Depending on the application intended, the surface of nanoparticles can be decorated with various molecules to avoid the recognition by the immune system and can be functionalized with targeting ligands to create specificity for a receptor of interest. Several molecule-specific ligands have been used, including antibodies and their fragments, aptamers, peptides, peptidomimetics, vitamins and carbohydrates (Mulder, Strijkers, van Tilborg, Griffioen, & Nicolay, 2006; Allen, 2002). To target exclusively cancer tissues, several nanoparticles have been functionalized to bind tumor biomarkers such as transferrin receptors (Choi, Alabi, Webster, & Davis, 2010), folate receptors (Hong et al., 2008), $\alpha_v\beta_3$ integrin (Winter et al., 2003), epidermal growth factor receptor (EGFR) (Yan et al., 2009), human epidermal growth factor receptor 2 (HER2) (T. Chen et al., 2009), prostate specific membrane antigen (Wang et al., 2007) and somatostatin receptors (Li et al., 2009).

Despite the increasing diversity of nanoparticles, most can be classified into two major types: inorganic or organic. Inorganic nanoparticles have an inorganic core that confers specific fluorescence, optical, electronic and magnetic properties. The surface core is coated with a protective biocompatible organic layer that stabilizes the structure, avoids uncontrolled growth, aggregation and delays blood elimination of the nanoparticles (Yezhelyev et al., 2006). Some examples are quantum dots, superparamagnetic, silver, gold, silica and calcium nanoparticles (Tiefenauer, 2007; Xing, Chang, & Kang, 2010). These nanoparticles are disadvantageous for systemic

cancer cell targeting, because they are neither biodegradable nor small enough to be efficiently cleared from the blood through the kidneys, and can thus accumulate in the body and cause long-term toxicity (Peer et al., 2007). Organic nanoparticles such as liposomes, micelles, dendrimers, carbon nanotubes and other polymers are composed of organic materials (Lee, MacKay, Fréchet, & Szoka, 2005; Yezhelyev et al., 2006). These nanoparticles have been extensively used as drug and CA carriers. They present an increased hydrophilic and hydrophobic content, bio-availability, a high surface-area-to-volume ratio, which allows attachment of several targeting ligands to the surface, and have shown an efficient accumulation at pathological locations (Kairemo et al., 2008; Peer et al., 2007).

Polymers are the most commonly explored materials for the design of organic nanoparticles. These biomaterials are long-chain molecules composed of a large number of small repeating units (monomers), and can be derived from natural sources or from organic synthesis (Cooper, Visser, Hergenrother, & Lamba, 2004).The methods of synthetic polymer preparation can be classified into two groups: addition polymerization and condensation polymerization. In addition polymerization, monomers have to be activated by an initiator (free radicals, cations, anions or catalysts) to react through the stages of initiation, propagation, and termination to form the final polymer. For condensation polymerization, the monomers contain functional groups, so the initiator is not required. Two monomers react to form a covalent bond, usually with elimination of a small molecule such as water, hydrochloric acid, methanol, or carbon dioxide. The reaction is continuous until one of the reactants finish (Park & Lakes, 2007, pp.173-177). The choice of polymerization method strongly affects the polymer obtained. For example, considering addition polymerization of free radicals, the molecular weights of the polymer chains are difficult to control while in anionic polymerization the molecular architecture can be easily controlled. Recent methods of living free radical polymerizations called atom transfer radical polymerization and Reversible Addition-Fragmentation chain Transfer (RAFT) polymerization have been used to create amphiphilic block copolymers with well-defined structures. These methods proved to achieve low polydispersity indexes, which enable well-controlled composition, size and morphology of polymeric micelles (Zhang, Zhang, Wen, Li, & Li, 2008; Stenzel, 2008).

Polymers can be classified as homopolymers, which are composed by one type of repeat unit, or as copolymers, which are made by two or more types of repeat units.

Regarding copolymers, the structure of polymer chains can be alternating (monomers alternate along the chain), random (monomers are randomly distributed along the chain), graft (main chain is made up by one type of monomer to which are bounded small chains of another monomer), or block copolymers (the polymer chain is formed by blocks of each monomer). As block copolymers have separate segments they display the individual features of each homopolymer (Cooper et al., 2004).

1.1.1. MICELLES

Micelles are self-assembling nanosized colloidal particles with a hydrophobic core and hydrophilic corona (Figure 1) (Torchilin, 2007). There are several composites able to form micelles. However, amphiphilic block copolymers have received a great deal of attention. These polymers are composed by hydrophilic and hydrophobic monomer units. These molecules form micelles spontaneously when they are dissolved in selective solvents, under a narrow concentration interval (critical micelle concentration) and temperature (critical micellization temperature) (Palivan, Vebert, Axthelm, & Meier, 2006; Jones & Leroux, 1999). Polymeric micelle formation involves a decrease of free energy in the system due to elimination of hydrophobic blocks from the aqueous environment. The hydrophobic region of the amphiphilic polymer forms the micelle core, while the hydrophilic region composes the micelle corona that stays in contact with water (Kwon & Okano, 1999).

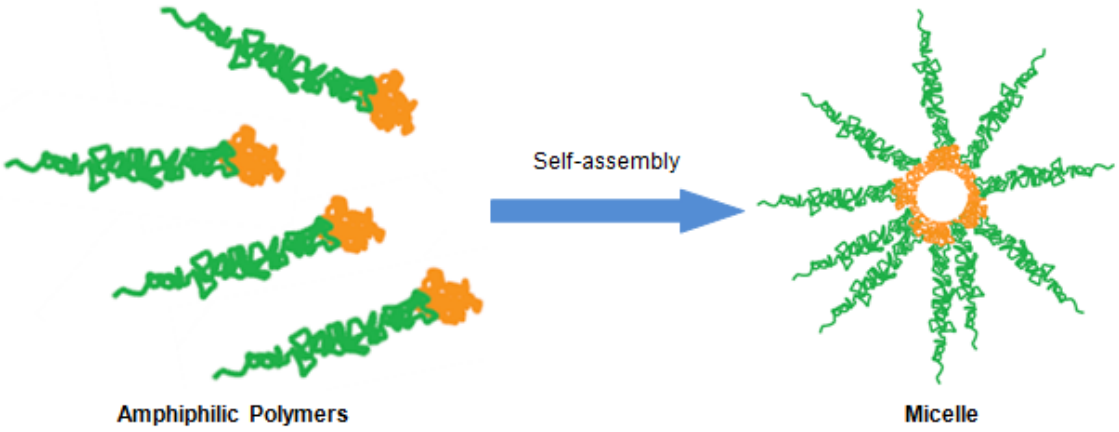

Figure 1 - Micelle structure. Polymeric micelles are composed by a hydrophobic core (orange) and a hydrophilic corona (green). Adapted from (Peer et al., 2007).

Polymeric micelles have been successfully used as drug carriers due to their high stability *in vitro* and *in vivo* and improved bioavailability of the content. Micelle content can be released by surface erosion, by diffusion through progressive degradation of the hydrophobic core, or in response to environment (pH, temperature, or salt concentration sensitivity) (Rutkaite, Swanson, Li, & Armes, 2008). In addition, their smaller size compared to other particulate carriers allowed a superior permeability across physiological barriers and improved biodistribution (Nakamura, Makino, Okano, Yamamoto, & Yokoyama, 2006; Hong et al., 2008; Maeda, Wu, Sawa, Matsumura, & Hori, 2000). The use of copolymers having a poly (ethylene glycol) (PEG) extends the micelle half-life in blood. A direct correlation between the longevity of a particulate drug carrier in the circulation and its ability to reach its target site has been observed on multiple occasions (Maeda, Sawa, & Konno, 2001; Torchilin, 2001). Micelles have also a reasonably narrow size distribution, and are very easy to prepare and to load drug or CA (Heller & Hoffman, 2004). By changing the copolymer chain size and chemical nature, the type of solvent used to dissolve the copolymer, and the critical micelle concentration of the copolymer, it is simple to modify the shape and size of polymeric micelles. Several formulations of drug-loaded micelles are currently at different stages of preclinical and clinical trials (Torchilin, 2007).

The transport of CA by micelles is a relatively new approach, which have been experimented just for diagnostic/imaging or for monitoring the drug delivery by micelles (Liu, Zeng, & Allen, 2007; Zhang et al., 2008).

A promising approach on medical imaging is the use of stimuli-sensitive micelles whose degradation and resultant content release is due to pH or specific temperature values (Nakamura et al., 2006; Torchilin, 2007). Stimulus-sensitive micelles are made of "smart" polymers, which respond to slight alterations in physical, chemical or biochemical environmental conditions with significant changes in their physical properties (Hoffman, 2004). Consequently, micelles composed by these special polymers are able to dissociate the core and release their content only under certain pathological features (Palivan et al., 2006). Several approaches using pH-sensitive micelles, which release their content in conditions of low tumor cell pH, have been studied and used successfully to improve the efficiency of chemotherapy and to decrease the side effects and toxicity of free chemotherapeutics (Lee, Na, & Bae, 2003; Lee, Na, & Bae, 2005; Gillies & Fréchet, 2005; Hrubý, Konák, & Ulbrich, 2005).

1.1.1.1. pH-SENSITIVE MICELLES FOR EARLY CANCER DETECTION

This new kind of pH-sensitive nanoparticles seemed to be a very promising approach for early cancer detection because they disassemble exclusively in a specific pH value, have proven to be stable and are efficient carriers for hydrophobic drug molecules. Therefore a new class of nanoparticle-based CA has been developed.

The proposed pH-sensitive polymeric micelles are able to encapsulate a large number of CA molecules (hydrophobic Gadolinium ion [Gd(III)] chelates) during its self-assembly from simple building blocks (Poly(ethylene glycol-b-trimethylsilyl methacrylate). The pH-sensitive mechanism of the designed polymeric micelles is generated by amphiphilic polymer silicon moieties that can be cleaved in a slightly acidic environment. This cleavage turns the polymer hydrophilic, which triggers micelle disassembly and release of its content (Figure 2). This pH-sensitive amphiphilic diblock copolymer was synthesized by RAFT polymerization from trimethylsilyl methacrylate using α-(O-ethylxanthate)-ώ-methylPEG 2'000 as a macro-chain transfer agent (macro-CTA), and a monomer to macro-CTA ratio of 45:1. Azobis-isobutyronitrile (AIBN) (1 mol% of the monomer), was used as radical initiator (Chiefari et al., 1998). The CA was synthesized and characterized via well known synthesis routes to generate hydrophobic Gd(III) complexes with ligands such as bipyridine (Bechara, Leygue, Galaup, Mestre, & Picard, 2009).

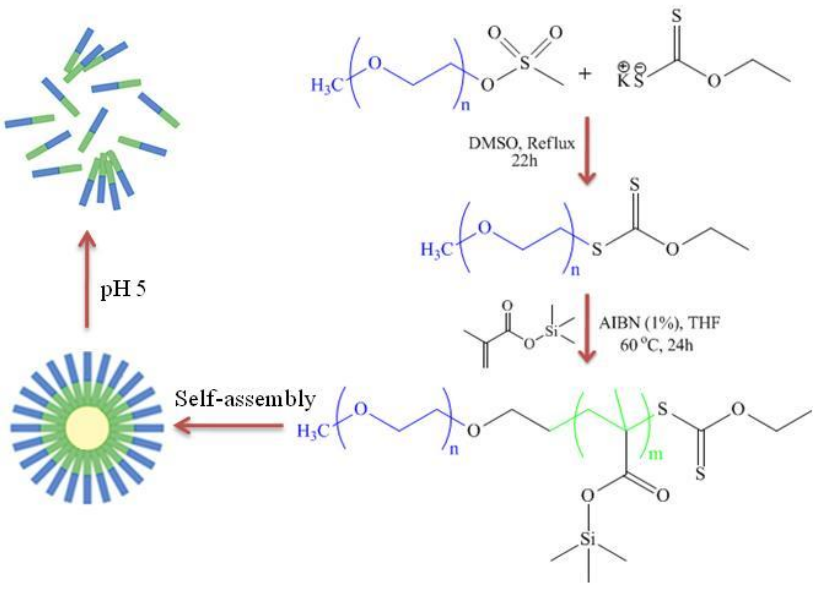

Figure 2 – Schematic representation of amphiphilic diblock copolymer synthesis and micelle pH-sensitive disaggregation. Synthetic approach for the synthesis of poly(ethylene glycol-*b*-trimethylsilyl methacrylate) and schematic representation of its self-assembly into micelles and their disaggregation due to pH decrease.

These polymeric micelles were designed to remain intact during circulation and if the target is absent, the CA remains switched-off until their removal from the system. However if micelles reach the target site (cancer tissue), they disassemble due to low pH. When micelles are intact, they restrict water access to the hydrophobic Gd(III) chelates that are located in the micelle core. Consequently, the relaxivity of nearby water molecules remain unchanged, however when these Gd(III) complexes are released from the micelle core, they will have access to water molecule protons and thus reduce the longitudinal magnetization time (T_1) of the water surrounding the targeted tissue. This new approach will therefore provide the medicine with better tools to understand the causes and mechanisms of disease and the associated structural and functional alterations.

The size distribution profile of the novel micelles (with encapsulated 1-methylpyrene) was found to be around 24 nm (Figure 3), as measured by dynamic light scattering (DLS) (Figure 3-A). These micelles were also visualized under transmission electron microscopy (TEM) (Figure 3-B) and the size matches the values obtained from DLS.

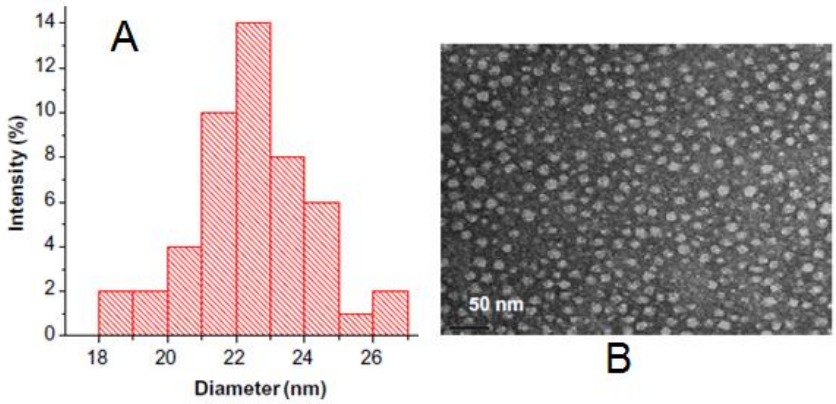

Figure 3 – Micelle size characterization. (A) Dynamic Light Scattering results showing the size distribution profile of 1-methylpyrene loaded polymeric micelles. (B) Transmission electron microscopy of 1-methylpyrene loaded polymeric micelles after the self assembly of poly(ethylene glycol-*b*-trimethylsilyl methacrylate), bar scale 50nm.

To establish the amphiphilic aggregation of the copolymer and its disaggregation, with parallel tracer release under pH change, it was used the 1-methylpyrene fluorescence spectrum. When 1-methylpyrene is dissolved and encapsulated inside micelles, it reaches a threshold concentration ($\approx 10^{-4}$ M) that induces the formation of excimers, which have a different emission wavelength than 1-

methypyrene monomers. The monomer emission occurs in less concentrated solutions and in aqueous solutions due to the low solubility of 1-methylpyrene. The emission spectrum of 1-methylpyrene-loaded micelles in a pH=7 aqueous solution revealed both monomer (at 375 nm) and excimer (at 480 nm) emission bands, indicating that micelles existed in the aqueous solution. On the other hand, the emission spectrum of 1-methylpyrene-loaded micelles in a pH=5 aqueous solution showed only the monomer emission band, indicating that nanoparticles were decomposed and had release their content. The release causes contact of excimer with water and consequent decrease of the threshold concentration required to form them (Figure 4).

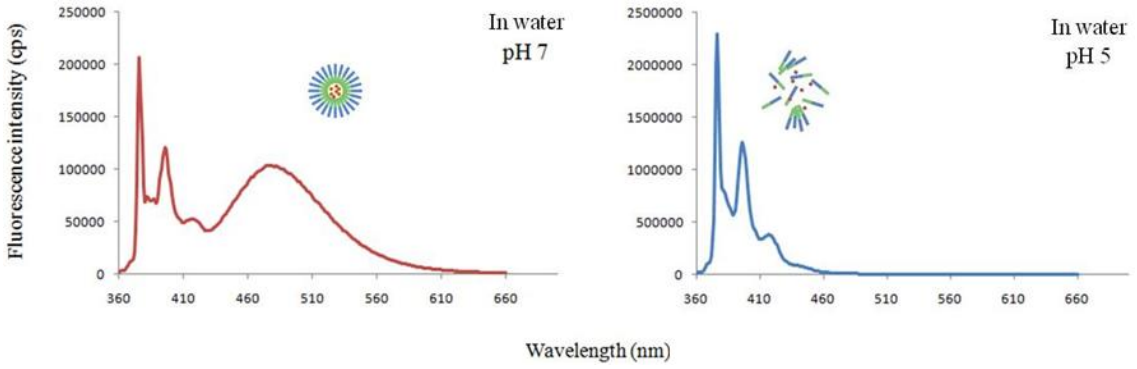

Figure 4 - Spectroscopic proof of polymeric micelles formation and disassembled with parallel release of 1-methylpyrene due to low pH. At pH=7 the polymeric micelles are stable as the excimer band (480 nm) holds. However at pH=5.5 only the monomer emission (375 nm) stands due to complete release of 1-methypyrene.

After proving the ability of these nanoparticles to release their content in acidic conditions, we demonstrated by ^{1}H Magnetic Resonance (NMR) Spectroscopy that the CA (tetraaquodichloro(4,4'-ditBu-2,2'-bipyridine)gadolinium(III) chloride) encapsulated within the micelle core was shield from water molecules in solution (Figure 5). This conclusion stems from the observation that the T_1 measured in a pH=7 aqueous solution with Gd(III) complex-loaded micelles was 3.4 seconds, while at pH=5 the T_1 time obtained was 1.7 seconds. At pH=7, intact polymeric micelles restrict the water access to the Gd(III) complexes and the T_1 value is the same as the T_1 measured in pure water (switched-off state). In contrast, micelles disassembled due to low pH (similar to those found in cancer tissue) and the water molecules had accessed and exchanged with Gd(III) complexes, thus significantly decreasing the T_1 of the aqueous solution surrounding these nanoparticles (switched-on state).

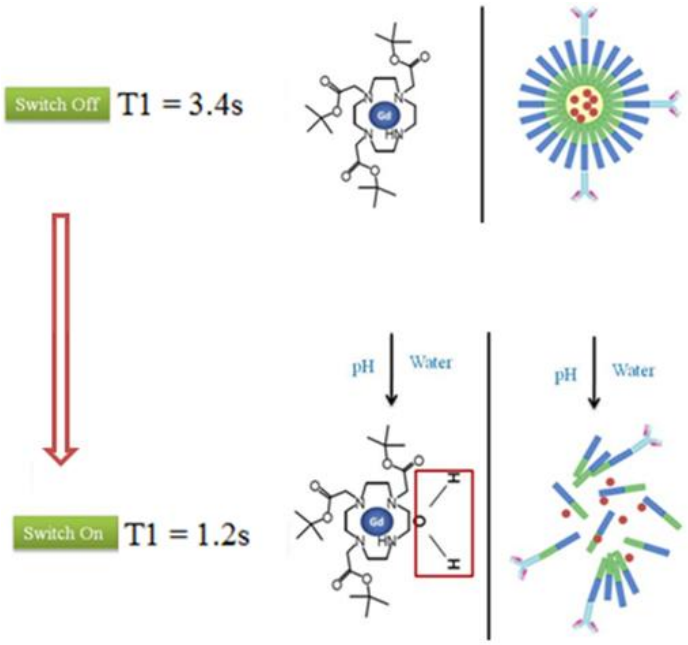

Figure 5 - Schematic representation of switch off/on mechanism. Relaxometric experiment that measures the T_1time before and after the release of the contrast agent from the polymeric micelle using NMR.

Because the existing imaging techniques are generally unsatisfactory for many molecular imaging applications, it is important to develop high-performance imaging systems capable of identifying detailed biological processes at the molecular and subcellular levels. Currently, MRI is one of the most powerful medical diagnostic tools available mainly due to its high spatial resolution and by the fact that physiological and anatomical information can be acquired simultaneously (Li, Fraser, & Meade, 1999; Medarova, 2009). However, in terms of sensitivity MRI lags behind other tools (Massoud & Gambhir, 2003). To overcome this hurdle, several attempts have been made to improve the sensitivity of MRI using CAs. With the increasing ability of nanotechnology to create devices at the cellular and molecular scale, more powerful imaging CAs for MRI such as superparamagnetic particles of iron oxide (SPIO) and magnetodendrimers nanoparticles have developed. SPIO have gained great attention for molecular MRI and has been experimentally and clinically used to detect infarction, inflammation, angiogenesis, primary malignant lesions, and lymph node metastasis (Priest et al., 2006; Russell & Anzai, 2007; Gambarota et al., 2006; Corot, Robert, Idée, & Port, 2006). Although much progress has been made to develop these nanoparticles during the past few years, their successful use has been limited to *in vitro* systems,

except for a few *in vivo* cases. These difficulties lie on two factors: poor MRI contrast effects and limited stability and biocompatibility under *in vivo* conditions.

The new micelles have therefore a great potential to be used as CA for MRI. They present the advantage over other CAs of imaging cancer tissues only and not normal cells, because they expose Gd(III) chelates to the aqueous surroundings and enhance the relaxivity of the paramagnetic metal only under characteristic low pH cancer environments. These micelles should increase the half-life in blood of the Gd(III) complexes, by providing a protection from the outside elements via their encapsulation within their the core. Furthermore, this CA system will provide an increase in sensitivity through signal amplification of the targeted tissue. The signal is amplified via the massive amount of the CA that has been encapsulated within these micelles. This last feature allows detecting cancer in very early stage when cancer related molecular and cellular changes are minor, and reduces the amount of CA required for imaging.

2. MAGNETIC RESONANCE IMAGING

MRI is a non-invasive medical imaging technique with several advantages over others, such as the ability to obtain direct multiplanar images and physiological data and to avoid ionizing radiation. In addition, MRI allows submillimeter spatial resolution, which is the capacity to identify an object as a separate and different element from another object. It has an excellent contrast resolution, which is the ability to differentiate tissues with low contrast, and has a good sensitivity, which reflects how well an imaging system can detect slight differences in anatomy (Bushong, 2003, pp.3-15).

2.1. BASIC PHYSICAL PRINCIPLES

The human body is constituted by approximately 80% of hydrogen atoms. MRI collects the signal from the nuclei of hydrogen atoms to produce images (Bushong, 2003, pp.3-15). The proton of the hydrogen atom has a spin movement, which means that it turns around an axis. The orientation of its rotational axis is normally random during the rotation movement. Since the proton is a mass with an electrical charge in movement, it has a magnetic moment and acts as a bar magnet (Weishaupt, Kochli, & Marincek, 2006, pp.1-5). When the protons are exposed to a strong external magnetic field (B_0) they align themselves approximately with the direction of B_0 in two possible ways:

parallel or anti-parallel (Figure 6). These alignments imply distinct levels of energy, so the one that takes less energy, the parallel alignment, is the one which has a slight larger number of protons (Westbrook & Kaut, 2000, pp.1-11). The protons have now a wobble movement, called precession. This precession movement has a characteristic speed, which is positively correlated with the strength of the applied B_0 and is named precession frequency or Larmor frequency (McRobbie, Moore, Graves, & Prince, 2006, pp.137-144). When the protons are in precession movement, their individual magnetic moments add together and cancel each other as some protons align parallel and others antiparallel. However, there are more protons aligned parallel than antiparallel. Consequently, some magnetic moments are not cancelled and the resultant magnetization is represented by a vector in the z-direction, aligned with B_0 direction, called net magnetization vector (M) (Brown & Semelka, 2003, pp.1-9). This vector originates the signal for the MR image but while it has the same direction of B_0 it is impossible to measure it directly. For this purpose M has to be perpendicular to B_0. To obtain this, the system needs to have an energy supply, so an electromagnetic wave with the same frequency as the Larmor frequency will be applied to the system (McRobbie et al., 2006, pp.137-144).

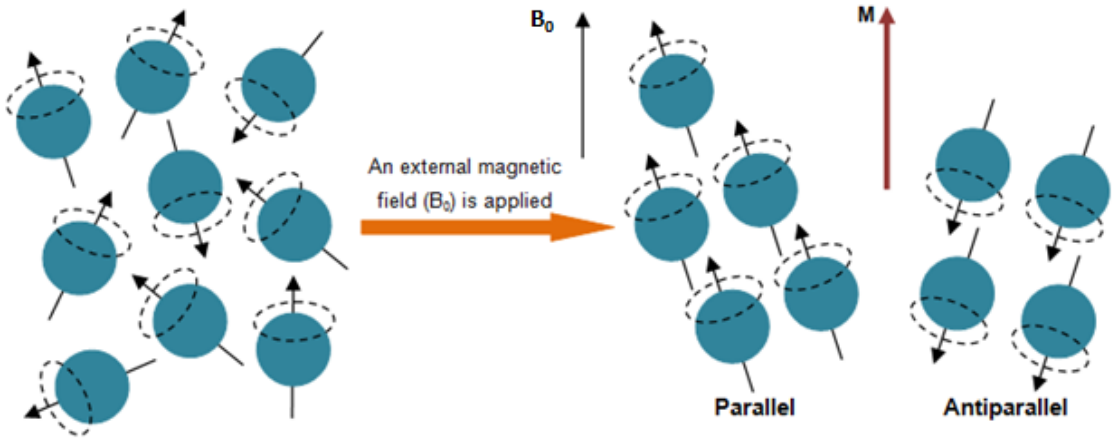

Figure 6 – Schematic representation of hydrogen nuclei behavior under the influence of a magnetic field (B_0). Protons usually spin with a random direction, however when applied B_0, they aligned in two ways: parallel and antiparallel. As little more protons align parallel to B_0, they create a longitudinal magnetization (M). Adapted from (Weishaupt et al., 2006, pp. 1-5).

The radiofrequency (RF) pulse, emitted from a radio antenna, called coil, will perturb the stable aligned precession movement of the protons and make them obtain energy, a process named resonance (Bushong, 2003, pp.3-15). The energy transfer has two consequences on the protons: changes the energy state of each proton and some will

raise to a higher level of energy, being into the negative z-direction (antiparallel to B_0) and also makes the protons to precess in phase coherence, which means that they all have an equal position on the precession movement (McRobbie et al., 2006, pp.137-144). These changes will traduce in a decrease of the longitudinal magnetization and in an appearance of a new magnetization in the xy-plane that is perpendicular to the direction of B_0, called transversal magnetization (Figure 7). The transverse magnetization precesses around the z-axis, being a constant oscillating magnetic field, which induces a voltage varying at the Larmor frequency. This signal, known free induction decay (FID) will be collected as a radio signal emitted from the human body by a receiver coil and processed by computers, giving rise to the MR image (Nitz & Reimer, 1999). The MR signal is fluctuating and decreases with time due to the proton spin relaxation in order to get the original state and is represented by time constants called relaxation times (Westbrook & Kaut, 2000, pp.1-11).

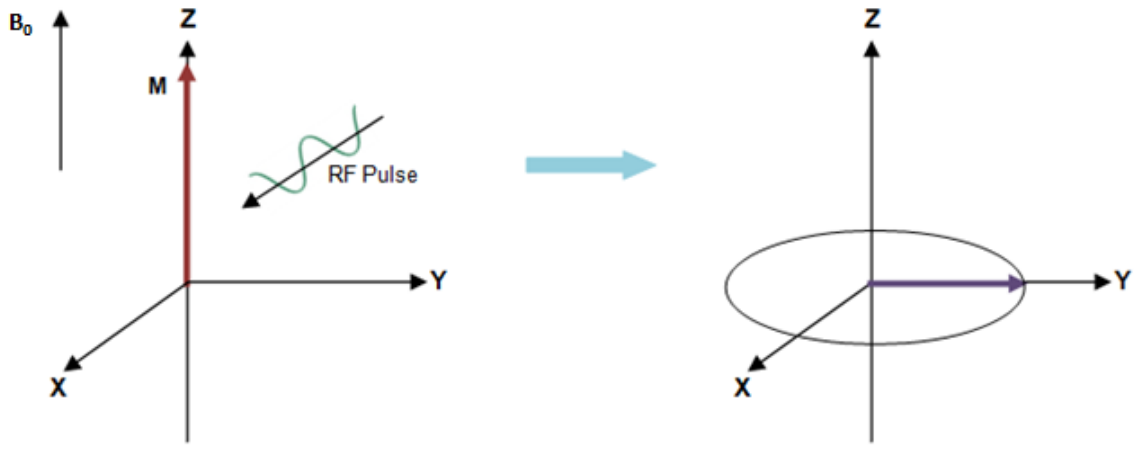

Figure 7 – Schematic representation of the behavior of the net magnetization vector, *M*, after the system received energy from a RF pulse. The RF pulse tips some protons to a higher level of energy and make the protons to precess is phase. As a consequence there is a decrease in longitudinal magnetization and appear a new transverse magnetization vector in xy plane, which rotate around z-axis. Adapted from (McRobbie et al., 2006).

2.2. RELAXATION TIMES

When the RF pulse is turned off, the system relaxes and returns to its lower state of energy, consequently the transversal magnetization diminishes until extinction (transversal relaxation) and the longitudinal magnetization increases until its original value (longitudinal relaxation) (McRobbie et al., 2006, pp.148-153).

Longitudinal or spin-lattice relaxation happens due to energy transfer for the environment or lattice and the time constant that represents how quickly is the recovery of longitudinal magnetization is named longitudinal magnetization time or T_1. This time constant is dependent on the strength of B_0 and the inner movement of the molecules (Brownian motion). Transversal or spin-spin relaxation is caused by internal magnetic field variations such as different proton precession frequencies because of inhomogeneity in B_0 and the influence of the magnetic field of each proton in the nearby nuclei. The different precession frequencies cause the protons to be out of phase. This will cause the decrease of transversal magnetization and the constant time which describes this process is the transversal relaxation time or T_2 (Brown & Semelka, 2003, pp.21-31). These two relaxations times T_1 and T_2 represent two independent processes which occur at the same time (Bushong, 2003, pp.64-71).

2.3. MAIN TYPES OF IMAGE CONTRAST

Contrast in MR images is reached based on tissue differences in T_1, T_2, and proton density (PD). These parameters are intrinsic features of biological tissues which using different RF pulse sequences can produce an image intensity that can be weighted with respect to T_1, T_2 or PD (Figure 8) (Nitz & Reimer, 1999). As these parameters are very different from one tissue to another, this allows soft-tissue discrimination and diagnostic potential of MRI. To create an MR image, a slice of the body has to be excited with more than one RF pulse (a succession of RF pulses is a pulse sequence) and the emitted signal recorded many times. The repetition time (TR) is the interval between two successive excitations of the same slice and consequently the duration of the relaxation period between two excitation pulses. The echo time (TE) is the time-period between application of the RF pulse and the collection of the MR signal (Weishaupt et al., 2006, pp. 11-20). The generation of T_1-, T_2-, or PD-weighted images depends on the TR and TE values (Nitz & Reimer, 1999).

The time constant T_1 is short when the change of energy is efficient (the lattice has precession frequencies near the Larmor frequency). When the molecules in the environment do not move at the Larmor frequency, the protons are not able to send its energy fast to the surroundings, so they will be slower to return to their lower energy level. Consequently the longitudinal magnetization will take a long time to recover, and the T_1 time will be long (Westbrook & Kaut, 2000, pp.12-20). To get advantage of this

biological characteristic one can use a short TR to create a difference in signal intensity between different tissues. This difference will be possible because the tissues with short T_1 will recover faster than others with long T_1. However, if a long TR is used, all tissues recover its longitudinal magnetization and the signal differences disappear. So the resulting MR image of a short TR is classified as T_1-weight image (T_1WI) (Figure 8-A), since tissue contrast is mostly created by their difference in T_1 times. Tissues with short T_1 appear bright and others with a long T_1 present a weak signal (Nitz & Reimer, 1999).

The T_2 time constant represents the velocity of decrease in transversal magnetization vector after the RF pulse excitation. When the image contrast is almost dependent of the T_2 times of the tissues, the image is classified as T_2-weighted image (T_2WI) (Figure 8-B). If a long TE is used, the tissues show different signal intensities and a good contrast on the MR image. The tissues with short T_2 lose their transversal magnetization and appear dark, while tissues with a long T_2 maintain the magnetization longer and produce a stronger signal appearing bright (Nitz & Reimer, 1999).

PD is the number of hydrogen atoms in a particular volume. To get a PD-weighted image (Figure 8-C) the influence of the other two parameters, T_1 and T_2, has to be suppressed. To this end, a long TR and a short TE is used, so that the collected signal is neither T_1WI nor T_2WI, but mostly influenced by differences in proton density. Thus, tissues with large content in hydrogen emit a stronger signal (McRobbie et al., 2006, pp.32-36).

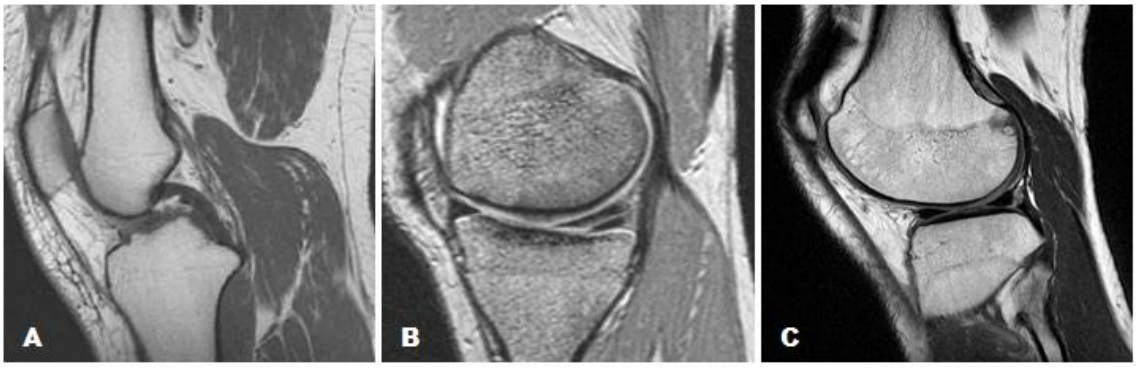

Figure 8 - Sagittal images of the knee. (A) T_1-weight image. (B) T_2-weight image. (C) PD-weight image. Adapted from (McRobbie et al., 2006, pp.32-36).

3. MAGNETIC RESONANCE IMAGING WITH CONTRAST AGENTS

MRI easily creates a distinction between different tissues based on differences in T_1, T_2 and PD. However, healthy and pathological tissues as well as distinct diseases show similar magnetic moments producing a poor image contrast. To get a better anatomical differentiation and to improve sensitivity, CAs are used. Due to their physico-chemical properties, CAs induce different effects on image signal intensities by modifying the intrinsic contrast properties of biological samples (Weishaupt et al., 2006, pp.103-123). CAs can also increase image quality, allow higher resolution, and provide kinetic information about an enhanced lesion (McRobbie et al.,2006, pp.42-44).

CAs act by shortening T_1 and T_2 relaxation times, however, some tracers decrease specially T_1 time. Consequently, tissues with a short T_1 appear bright on T_1WIs. These CAs are called positive because they enhance the image signal. They are also classified as T_1 CAs because effects of lower concentrations are easily observed on T_1WIs. On the other hand the contrasts which have a greater change in T_2 time of tissues are called negative, because they cause a decrease in image signal (Figure 9-B). They are T_2 CAs, because their effect is clearly evident on T_2WI (Gandhi, Brown, Wong, Aguirre, & Sirlin, 2006)

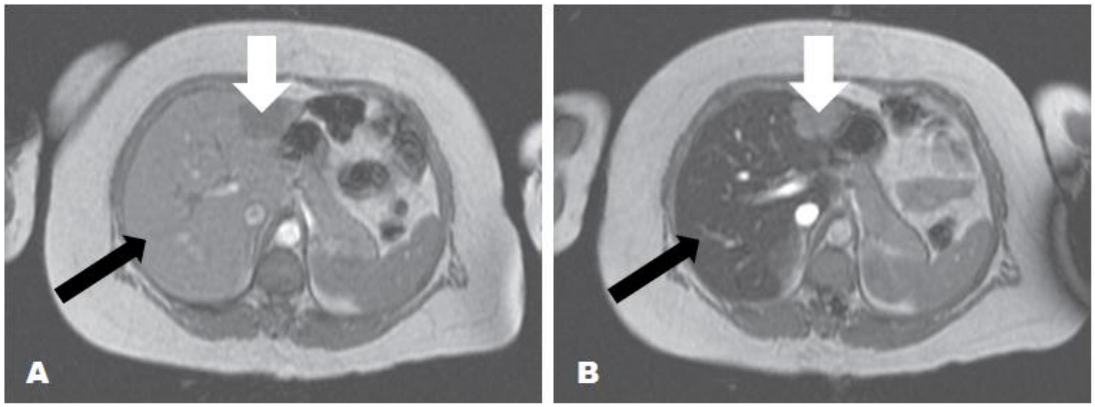

Figure 9 – Negative contrast provided by uptake of SPIO by Kupffer cells (RES). (A) Axial T_2WI obtained before the administration of SPIO. (B) Axial T_2WI after injection of SPIO demonstrates signal image decrease on normal liver parenchyma due to uptake of iron oxide nanoparticles (black arrow) and maintenance of the enhancement by metastatic liver lesion (white arrow), which tumor cells replaced kupffer cells. Adapted from (McRobbie et al., 2006, pp.42-44).

The present thesis is about a T_1 CA based on Gd(III) chelates. Therefore the mechanism of action and classification will be detail describe for Gd(III)-based CAs.

3.1. MECHANISM OF SHORTENING T_1 AND T_2 TIMES

In the human body, the water molecules possess a rotation movement faster than Larmor frequency, consequently their relaxation is inefficient and they have a long T_1. The spin molecules used as CA have a high magnetic moment and in close contact with the protons of water they will induce a fluctuation in the neighboring magnetic fields near the Larmor frequency. This influence will facilitate the water molecules to decrease the energy that have previously gained from the RF pulse. Therefore the relaxation time T_1 of the neighbor water protons is reduced and water will appear bright in a T_1WI. There is also a decrease of T_2 due to the magnetic moments of unpaired electrons, which alter the local magnetic field strength, causing a faster dephasing of the protons (Westbrook & Kaut, 2000, pp.193-197). The magnetic field inhomogeneity created by Gd(III) has a very small distance of action, however the newly affected protons will also exchange with other protons further away from Gd(III). So there is an overall reduction of T_1 and T_2 (Gandhi et al., 2006).

The interference in the local magnetic field strength is due to dipole-dipole interactions between the unpaired electron spins or protons of the CA and the neighboring excited hydrogen nuclei of the water, fat, or protein molecules which compose the tissue. Therefore, a fraction of the action mechanism of the CA is based on the electron shell and not simply due to nuclear interactions. The magnetic moments of the electrons are much higher than those of protons, thus the electron shell contains powerful paramagnetic properties. The relaxation produced by contrast on surrounding tissues is a result of inner-sphere and outer-sphere effects. The first one is caused by the relaxation of the hydrogen nuclei of water molecules directly bound to the paramagnetic ion of the CA, and the second is caused by interactions between paramagnetic ions and closely diffusing water molecules (McRobbie et al., 2006, pp.162-166).

The interaction efficiency of CA with nearby water molecules is translated by the measure of relaxivity or relaxation rate (R_1 and R_2). This parameter is the inverse of the relaxation time, so it is determined by measuring T_1 or T_2, respectively, in a one molar solution. A higher relaxivity reflects an efficient interaction between the CA and the water protons, thus a faster relaxation of the protons and an increase in signal on T_1WI (Weishaupt et al., 2006, pp.109-112).

3.2. CONTRAST AGENTS FOR T_1WI

Paramagnetic substances are atoms or molecules which have a strong magnetic moment due to unpaired electrons in their outer electron shells or unpaired nucleons in their atomic nuclei (Westbrook & Kaut, 2000, pp.193-197). When these paramagnetic materials are under an external magnetic field, their magnetic moments align, add up and create a positive and strong net magnetization, while most body tissues, which are diamagnetic, become only weakly magnetized. Some metal ions that can be used as CA are Gd(III) and Manganese (II) and Manganese (III) (Kozlowska et al., 2009).

Gadolinium belongs to the lanthanide series of rare earth elements. It has seven unpaired electrons, and therefore very strong paramagnetic properties (Que & Chang, 2006). Free Gd(III) is toxic because its diameter is close to that of calcium ions. Indeed, gadolinium ions bind to calcium channels, preventing binding of calcium ions. For this reason Gd(III) cannot be used in their elemental state but have to be chelated to a ligand. Some examples of ligands used for complexing the Gd(III) are DTPA, DOTA, DTPA-BMA, HP-DO3A. These ligands reduce significantly Gd(III) toxicity and influence the pharmacokinetics of the complex. Several Gd(III) formulations are available for commercial use and others are under experimental scrutiny (Weishaupt et al., 2006, pp.107-109).

3.2.1. NONSPECIFIC Gd(III)-BASED CONTRAST AGENTS

The most frequent CAs used in clinical MRI are small molecule Gd(III) chelates that can distribute uniformly to all perfused tissues throughout the vasculature, and can diffuse across endothelial wall vessels into the extracellular spaces (Gandhi et al., 2006; Gillies, Raghunand, Karczmar, & Bhujwalla, 2002). These molecules are however too large to cross the blood-brain barrier, except when this is disrupted by pathological conditions (*e.g.* primary tumors and metastasis). In these settings, low molecular weight contrast agents (LMWCA)s can enter and accumulate in the affected brain tissue, resulting in increased visibility of the lesion. After systemic body distribution, these tracers are rapidly eliminated by kidneys (Padhani, 2002).

LMWCAs have been extensively used to improve tumor localization and characterization through dynamic contrast enhancement (DCE) MRI. Some examples are cancers of the breast (Turnbulla, 2009), liver (Goshima et al., 2009), bone (Reddick

et al., 2001), lung (Hunter et al., 1998), pancreas (Murakami, Nawano, Moriyama, & Onuma, 1998), prostate (Ocak et al., 2007), and brain (Padhani, 2002).

DCE MRI consists in the acquisition of data after intravenous administration of CA. This method provides anatomical images and physiologic data such as a time-enhancement curve, which is used to assess the enhancement of the lesion during the CA uptake and washout. Analysis of the curve shape aids the physician in the diagnosis of the tumor and in the distinction between a benign or malignant lesion (Rausch & Hendrick, 2006). A large portion of invasive breast cancers usually exhibit a quick and strong enhancement, and this is followed by either stabilization or fast loss of the signal intensity. On the other hand, benign lesions show a weaker but continuous enhancement. Contrast enhancement analyses are an excellent diagnostic tool for breast cancer in that more than 90% of breast cancers lesions show a strong enhancement (Kuhl, 2007). However, contrast enhancement is nonspecific because of considerable common contrast enhancement features between benign and malignant lesions (Rausch & Hendrick, 2006). For this reason, LMWCAs showed a high sensivity for tumor detection (*e.g.* breast tumors) but lack of specificity (Mattrey & Aguirre, 2003).

LMWCAs are not taken up by particular organs, do not target specific tissues or pathological areas, and do not respond to the cellular microenvironment. They enhance all vessels and high vascular tissues (Figure 10-B). Thus only lesions with significant blood flow volumes can be distinguished by MRI, making it almost impossible the detection of primary cancer or metastasis when they measure just a few millimeters. Also, since these contrast agents leak through both normal and neoplastic vessels, it may be difficult to distinguish between normal and angiogenic vessels (Hartman et al., 2008; McDonald & Choyke, 2003). These CAs have also a short half-life in blood (Mattrey & Aguirre, 2003) and a large part of administered CA is eliminated before images are taken. Therefore, in order to get informative images, a substantial quantity of CA needs to be injected in the patient, which may constitute at times a health risk for some patients (Nakamura et al., 2006).

To overcome the drawbacks showed by LMWCAs, macromolecular weight contrast agents (MMWCA)s are in development. Some examples of MMWCAs are iron oxide particles and Gd(III) bound to larger molecules such as albumin, polylysine, dendrimers, micelles and liposomes (Padhani, 2002).

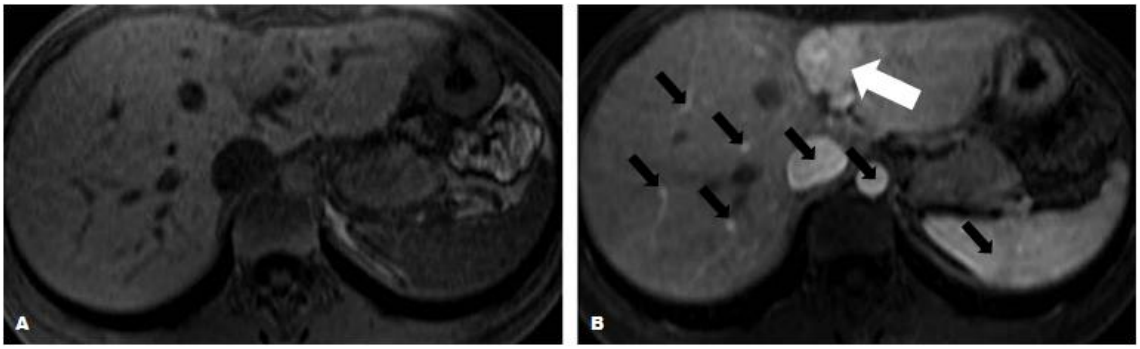

Figure 10 - Nonspecific image signal enhancement following administration of LMWCA. (A) Axial T_1WI obtained before the administration of Gd(III) chelates, image with no apparent lesion. (B) Axial T_1WI after injection of CA demonstrates enhancement of a liver lesion (white arrow), blood vessels and high perfused organs (black arrows). Adapted from (Gandhi et al., 2006).

These MMWCAs diffuse poorly or not at all through normal vessels, leaking only when the vessel wall is abnormal, as is the case for neoangiogenic vessels (Bhujwalla, Artemov, Natarajan, Ackerstaff, & Solaiyappan, 2001). MMWCAs are frequently used to blood pool imaging because of their long circulation times and slower diffusion as well as clearance from interstitial spaces (Gillies et al., 2002). This slower kinetics allows a better quantification of vascular leakage, thus helping to differentiate benign from malignant tumors. MMWCAs have therefore been reported to be better suited for assessment of microvasculature permeability of tumors lesions (Daldrup et al., 1998; Padhani, 2002). However, hyperpermeability to MMWCAs is not exclusive of cancer microvasculature, since it has also been observed in inflammatory, ischemic and transplant rejection tissue models (Mattrey & Aguirre, 2003).

Chen and colleagues created a MMWCA for hepatocellular carcinoma detection in rats. They used self-assembled micelles made by poly lactic acid–PEG and commercial Gd(III)–DTPA. The Gd(III)–DTPA was absorbed onto the surface of the nanoparticles. This MMWCA provided better and prolonged image contrast effects than commercial LMWCA in liver, even with a lower dose of gadolinium per kilogram of body weight (Z. Chen et al., 2009). Zhang and colleagues reported a successful production of micelles based on biodegradable poly(L-glutamic acid)-*b*polylactide block copolymer with DTPA-Gd(III) chelated to the micelle shell. This complex showed two-fold higher relaxivity than LMWCA (Zhang et al., 2008). Bertini and coworkers developed a MMWCA for detection of solid tumors. This probe consisted of PEG-stabilized paramagnetic liposomes, with Gd(III)–DTPA on their surface. This

MMWCA showed increased relaxivity compared to conventional LMWCA and achieved a prolonged visualization of neoplastic lesions in mice (Bertini et al., 2004).

3.2.2. TARGETED Gd(III)-BASED CONTRAST AGENTS

Since current MRI CAs have low specificity and since MRI has proven to be a valuable molecular imaging tool, efforts have been taken to develop targeted and specifically activated CAs. These tracers aim to target distinct molecules related with different pathologies, accumulate selectively in a exact biological site providing an increased local concentration of CAs, allow more specific diagnosis, and have the potential to characterize diseases at the molecular level *in vivo* (Aime et al., 2002; Kozlowska et al., 2009). Targeted CAs identify specific cell types by internalization or interaction with proteins expressed on the cell surface (Lyons, 2005). Most MRI CAs used for molecular imaging are linear polymers and dendrimers conjugated to metal chelates as well as liposomes and micelles containing paramagnetic ions (Liu et al., 2010).

An approach of target Gd(III)-based CA consisted of perfluorocarbon nanoparticles able to detect integrins expressed on neovasculature in nascent Vx-2 rabbit tumors. In this experiment, a small arginine-glycine-aspartic acid-peptidomimetic was covalently attached to the nanoparticle. These nanoparticles showed specific signal enhancement in sites of tumor angiogenesis. Furthermore, the leakage in tumor vessels was greater than in muscle (Winter et al., 2003). Another research group successfully combined a long-circulating liposome with membrane-incorporated Gd(III)-chelates and a cancer specific antibody, 2C5, attached to the liposome surface (Erdogan, Medarova, Roby, Moore, & Torchilin, 2008). To detect tumor cell death after chemotherapy, Krishnan and colleagues produced specific CA based on Gd(III)-chelates conjugated to the C2A domain of synaptotagmin I, which targets the plasma membrane phospholipid phosphatidylserine expressed by apoptotic cells. This probe was able to identify tumor cell death *in vivo* (Krishnan et al., 2008).

3.2.3. SMART Gd(III)-BASED CONTRAST AGENTS

Targeted CAs may greatly improve the accuracy and extent of diagnostic imaging. However, another approach based on physiological activatable or stimulus-sensitive CAs, seems to offer a significant improvement of the MRI potential for disease detection. Unlike standard targeted agents, which enhance MR image constantly, smart

CAs change between two conformational states dependent on a certain stimulus. The change is detected as an alteration in signal, because one of the conformational states has low or no enhancement, the "off state", and other has high enhancement, the "on state". These stimulus-sensitive agents can be detected when switched from one state to another after exposure to a metabolic or physiological event in a specific molecular target (Lyons, 2005). Smart CAs have been built on Gd(III) systems because their relaxivity can be dictated by their environment. The numbers of water molecules in the first coordination sphere, the water exchange rate and the rotational correlation time have a strong effect on the relaxivity of the compounds and can be influenced by many factors. There are CAs responsive to metal ions such as calcium (Li et al., 1999), copper (Que & Chang, 2006) and zinc (Hanaoka et al., 2002), while others are sensitive to oxygenated hemoglobin (Aime et al., 1999b), the presence of radicals (Glogard, Stensrud, & Aime, 2003), or are enzimatically activated to provide a means of measuring enzyme activity and enzyme localization (Moats, Fraser, & Meade, 1997).

The pH-sensitive CAs are of interest to tumor MRI imaging, because a common feature of cancerous tissues is a significantly lower extracellular pH as compared to healthy tissues. Thus, pH seems to be a promising parameter for detecting early stage cancer (Hartman et al., 2008; Gillies, Raghunand, Garcia-Martin, & Gatenby, 2004). To this aim, Zhang and colleagues created a pH-sensitive Gd(III) complex of a DOTA tetramide derivative. They observed an interesting behavior of the complex relaxivity versus pH. Indeed, starting from pH 4, the relaxivity first increased until pH 6 and then decreased until reaching a minimum at pH 8.5. It remained at this minimum between pH 8.5 and 10.5 and then increased again (Zhang, Wu, & Sherry, 1999). Aime and coworkers reported a pH-sensitive CA with Gd(III)-chelates and ornithin residues. The chelates were conjugated to the amino acid chain via squaric esters, which readily reacts with amines. At low pH, the amines are protonated and do not interact with the squaric ester residues. When the pH increases in a range of 4.5 to 8.5, the amine side chains become deprotonated and interact with squaric ester linkers. This interaction rigidifies the polymer creating and increasing relaxivity (Aime et al., 1999a). Also Hartman and colleagues synthetised ultrashort singe-walled carbon nanotube capsules that provided extremely high and pH-dependent relaxivity. These so-called gadonanotubes showed an increased relaxivity upon a decrease in pH from 7.4 to 7.0 (Hartman et al., 2008).

These smart contrast agents have proven to be excellent MRI tools for very specific targets *in vitro*, but failed to show the same performance *in vivo*, due to the

absence of sensitivity and selectivity towards tissues of interest. Several attempts have been made to improve these setbacks, including an increase in the number of contrast agents attached to monoclonal antibodies (MAb). However, these solutions have failed.

The new smart polymeric micelles loaded with Gd(III) complexes, besides exploring the characteristic features of cancer tissues (*e.g.* low extracelular pH and leaky vasculature) they accumulate and specifically image these lesions. Moreover, they can be bioconjugated with MAbs recognizing specifically cancer biomarkers, thus reinforcing their specificity for cancer tissue.

4. CANCER MICROENVIRONMENT

The cancer microenvironment has several characteristics that distinguish it from normal tissues. These features have been explored by smart and targeted nanoparticle-base CA to improve early cancer detection. The abnormal regulation of proliferation and apoptosis in cancer cells originates a pathological and disorganized increase in cell number and density. This results in a decreased access of tumor cells to the circulatory system (Gillies, Schornack, Secomb, & Raghunand, 1999). Consequently, there is a deficient supply of nutrients and oxygen and an insufficient washout of metabolic products (Bristow & Hil, 2008). In addition, the increase in aerobic glycolysis by cancer cells (Reshkin et al., 2000), creates a cancer microenvironment characterized by abnormal physiologic conditions such as hypoxic areas, low levels of serum nutrients, acidic extracellular pH (Penet, Glunde, Jacobs, Pathak, & Bhujwalla, 2008; Gillies et al., 2004), disorganized vasculature and inefficient lymphatic vessels (Rhyner et al., 2008).

In cancer tissues there is a reversed pH gradient across the cell membrane. Cancer cells normally have alkaline intracellular pH values (7.12–7.65 compared with 6.99–7.20 in normal tissues) and acidic interstitial extracellular pH values (6.2–6.9 compared with 7.3–7.4) (Gillies et al., 2002). This pH gradient seems to be present upon cancer cell transformation. The development and maintenance of this gradient is directly due to the ability of the cancer cells to secrete protons and acidify their extracellular environment, which will trigger mechanisms favoring tumor invasiveness and aggressiveness (Cardone, Casavola, & Reshkin, 2005). Indeed, the low extracellular pH of the tumor microenvironment has been shown to promote angiogenesis, accelerate the digestion and remodeling of the extracellular matrix by facilitating the action of acidic

proteases that are secreted by tumor cells, create genomic instability, and radiotherapy resistance (Orive, Reshkin, Harguindey, & Pedraz, 2003; Gatenby & Gillies, 2004).

Angiogenesis is vital for the development of most solid and hematologic cancers. As mentioned above, it occurs in response to metabolic alterations of the tumor microenvironment (Winter et al., 2003; Penet et al., 2008). These changes cause a cascade of cellular events that stimulate the production of angiogenic factors and decrease the production of angiogenesis inhibitors (Elias & Dias, 2008). Angiogenic factors induce endothelial cells to proliferate, invade, and migrate towards cancer cells, establishing the typically fragile, tortuous, disorganized and leaky vascular structure of cancers (Folkman, 2007).

Nanoparticles extravasate and accumulate preferentially at tumor interstitial spaces through the enhanced permeability and retention (EPR) effect. This effect is due to the increased permeability of tumor neovasculature and the dysfunctional lymphatic drainage system (Matsumura & Maeda, 1986; Rhyner et al., 2008). This nanoparticle accumulation through fenestrated capillaries into the tumor interstitial space is designated as passive targeting (Kairemo et al., 2008)., After performing experiments with liposomes of several sizes, Yuan and colleagues proposed that the limit nanoparticle size for extravasation into tumors is 400 nm (Yuan et al., 1995). Passive targeting has been extensively explored to obtain accumulation of nanoparticles in tumor lesions. This approach has however several limitations, such as the heterogeneous permeability of the vessel walls to macromolecules throughout the tumors. Moreover, some tumors do not show the EPR effect, and this kind of targeting is quite random as well as difficult to be controlled (Yuan et al., 1994; Daldrup et al., 1998; Peer et al., 2007). To overcome these hurdles, active targeting has been increasingly used. This is achieved by conjugating nanoparticles with molecules that bind overexpressed antigens or receptors on target cancer cells (Torchilin, 2007).

5. MUC1 PROTEIN

The mucin 1 (MUC1) protein was chosen as a cancer cell receptor for this new targeted MRI nanoparticle-based CA due to its demonstrated great potential for early detection and staging of cancers (Medarova, 2009).

The mucin family comprises proteins with tandem repeat structures rich in prolines, threonines and serines. The human mucin family is composed of many members designated from MUC1 to MUC21, and have been subclassified into secreted and transmembrane forms (Singh & Bandyopadhyay, 2007).

MUC1 (PEM, episialin, EMA, CD227, DF3) is a high-molecular-weight type I membrane glycoprotein with around 150-300 kDa. This glycoprotein is translated as a single polypeptide and is cleaved in the endoplasmic reticulum to form amino- and carboxy-terminal subunits (Levitin et al., 2005). The two MUC1 subunits form a stable non-covalent complex that is heavily O-glycosylated during transit through the Golgi complex. Then, this heterodimeric complex is anchored to the surface of the cell. The MUC1 N-terminal subunit is released from the cell surface into the mucous gel, leaving behind the MUC1 C-terminal portion. This domain functions as a receptor to detect the presence of inflammation and other forms of stress, and thus send signals to the interior of the cell (Kufe, 2009). The N-terminal subunit consist of up to 100 repeats of nearly identical *O*-glycosylated highly conserved variable number tandem repeat (VNTR) units of 20 amino acids (PDTRPAPGSTAPPAHGVTSA), flanked at both sites by a non-repeat region (Murray et al., 2001). Structurally, the C-terminal subunit includes a small extracellular domain, a transmembrane domain plus a cytoplasmic tail (CT). This subunit is 69 amino acid-long and has several tyrosine, serine, and threonine phosphorylation sites that when phosphorylated can bind to several proteins implicated in signaling pathways linked to transformation and cancer progression (Kufe, 2008).

Normally, MUC1 is localized on the apical borders of normal secretory epithelial cells. In response to stress, in order to protect the epithelial cell layer, this protein loses its polarity, being transiently repositioned over the entire cell membrane. The loss of polarity allows MUC1 to interact with cell surface molecules situated at the basolateral membrane and thus trigger cell proliferation and survival (Vermeer et al., 2003). MUC1 is upregulated in response to infection by pathogenic bacteria (McAuley et al., 2007). This is a defense mechanism, but prolonged stimulation of MUC1 in chronic inflammation can lead to deregulated cell growth and survival, as well as the

development of cancer (Kufe, 2009). MUC1 is also overexpressed during lactation (Rahbarizadeh, Rasaee, Moghadam, Allameh, & Sadroddiny, 2004), and when overexpressed in MMTV-MUC1 transgenic mice delays mammary postlactation involution, probably due to reduced apoptosis. Importanly, MUC1 overexpression in these transgenic mice promoted *in vivo* transformation of the mammary gland (Schroeder et al., 2004).

5.1. A TARGET MOLECULE FOR CANCER IMAGING

A valuable cancer biomarker is recurrently overexpressed in tumors and demonstrates negligible expression in normal tissues. To be useful, these tumor antigens should allow cancer detection in asymptomatic patients, thus improving the accuracy of current screening techniques (Brooks, 2009). MUC1 has long been recognized to gather several of these requisites.

This protein has been implicated in malignant cell transformation as well as cancer progression through stimulation of cell proliferation and apoptosis suppression (Bafna, Kaur, & Batra, 2010). Thus the MUC1 CT has been studied to understand its role as an oncoprotein (Huang et al., 2005). MUC1 has also been shown to promote metastasis, and has been associated with biologically aggressive tumors and a worse prognosis (Zhao et al., 2009). Another evidence supporting the notion that MUC1 is involved in malignant disease, is its high level of expression over the entire cell surface and intracellularly in almost all human epithelial cell adenocarcinomas (Figure 11). Some examples are breast, stomach, colorectal, lung, prostate, ovarian, pancreatic, and bladder cancers (Masri & Gendler, 2005; Cheng, Su, Wang, & Yu, 2009; Murray et al., 2001). Certain hematological malignancies (*e.g.* multiple myeloma cells, lymphomas and myeloid leukemias) also present MUC1 overexpression (Singh & Bandyopadhyay, 2007).

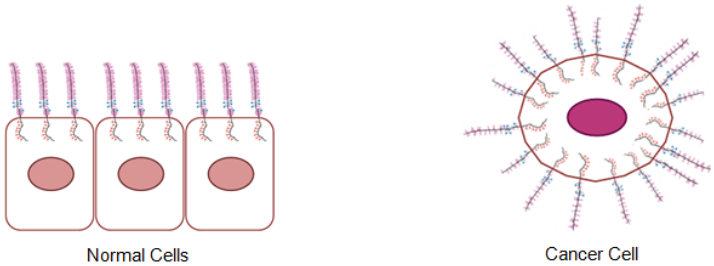

Figure 11 - MUC1 expression on normal and cancer cells. MUC1 is normally localized at the apical border of normal epithelial cells. However in cancer cells it is ubiquitously expressed all over the cell surface. Adapted from (Gendler, 2001).

In addition, the glycosylation pattern of the MUC1 N-terminal tandem repeats is altered in human carcinomas. MUC1 is hypoglycosylated and contains truncated or incomplete oligosaccharide side chains (Xiong, Natarajan, Shi, Denardo, & Denardo, 2006) (Figure 12). The underglycosylated MUC1 tumor-specific antigen has been pinpointed as one of the early hallmarks of tumorigenesis in breast, pancreatic and ovarian cancer (Medarova, Pham, Kim, Dai, & Moore, 2006; Mommers et al., 1999).

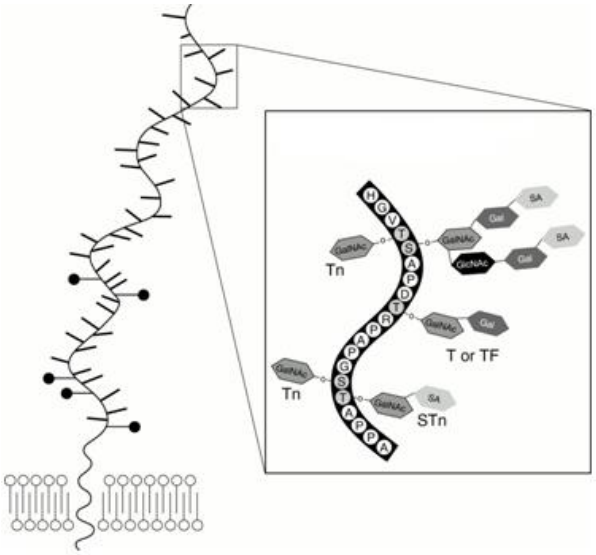

Figure 12 - MUC1 glycosylation pattern at a cancer cell surface membrane. MUC1 is heavily glycosylated on normal cells, whereas in cancer cells it is underglycosylated. The insert shows a MUC1 single tandem repeat unit with O-linked hypoglycosylated side chains. Adapted from (Berge et al., 2001)

Regarding specifically breast cancer, it is known that approximately 90% of these cancers are positive for MUC1 (Mahanta, Fessler, Park, & Bamdad, 2008).

In many cases, large amounts of MUC1 N-terminal subunit are detected in the blood of breast cancer patients, as a consequence of cleavage and shedding of this domain from the cell surface (Mahanta et al., 2008). This finding makes serum assays for MUC1 a potentially useful method for breast cancer detection (Ferreira et al., 2008). There are commercially available serum tumor marker assays using anti-MUC1 antibodies to measure concentration levels of circulating MUC1 N-terminal subunit, such as CA 15-3, Truquant-Br, CASA, CA549, MCA and CA 27.29 (Bon et al., 1997; Gendler, 2001). Determination of the level of this antigen in the blood has been exploited as a measure of tumor burden. In addition, the MUC1 changing levels reflect the response to therapy and allow detection of early disease recurrence (Kufe, 2009).

MUC1 is atypically overexpressed in several cancers. Therefore this protein became a promising target for the development of specific antibodies, vaccines and therapeutic inhibitors. Different types of murine anti-MUC1 MAbs were shown to recognize the MUC1 tumor marker and have recently underwent clinical trials (Kufe, 2009).

The MAb C595 was used as a specific targeting vector for ovarian cancer cells. C595 was labeled with Bismuth-213 and proved to effectively target and kill ovarian cancer cells *in vitro* and in *in vivo* cancer mouse models (Song et al., 2008). In a small clinical study, Hughes and colleagues used Indium-111 -labelled C595 MAb to detect invasive bladder cancer and metastases. This imaging approach demonstrated potential to improve clinical staging and detection of lesions not detected by conventional modalities (Hughes et al., 2001). Saloutia and co-workers labelled the MAb PR81 with Technetium-99m. The visualization of breast tumors in animal models with high sensitivity proved the potential of this new radiopharmaceutical to be used for radioimmunoscintigraphy of human breast cancer (Saloutia, Rajabia, Babaeib, & Rasaeec, 2008).

For imaging and therapy by hyperthermia of MUC1-expressing tumors, another research group conjugated commercial PEG-coated dextran-magnetic nanoparticles with isotope and antibody fragments against MUC1 (Natarajan, Xiong, Gruettner, DeNardo, & DeNardo, 2008). Using short specific peptide sequences derived from a MAb and combining two imaging modalities, another group successfully detected tumors that overexpressed the tumor-specific underglycosylated MUC1 antigen (Moore, Medarova, Potthast, & Dai, 2004). MUC1 was also detected by quantum-dot fluorescence using an aptamer-based approach. This work allowed detection of MUC1 protein and quantification of the amount of protein in a peptide sample (Cheng et al., 2009).

Two vaccines against MUC1 are in different phases of clinical trials for non-small cell lung carcinoma. The L-BLP25 liposome vaccine (stimuvax) was developed to stimulate the immune response against MUC1 tandem repeats, while the TG4010 (Transgene) is a modified vaccine virus expressing MUC1 and Il-2. Patients received the TG4010 vaccine with chemotherapy (Kufe, 2009). Despite these efforts, there are presently no validated agents applied in the clinic that are specific and efficient enough to target MUC1 (Kufe, 2009).

6. BREAST CANCER

The MUC1 protein is aberrantly expressed in the majority of breast cancer cases, even less aggressive early stage cancers. Recognition of tumor-specific expression of this protein by MRI with the new targeted pH-sensitive micelles could be very useful for early breast cancer detection, staging and prognosis (Medarova, 2009).

Breast cancer is the most frequent form of cancer in women and the commonest cause of death among women aged 40–50 years (McPherson, Steel, & Dixon, 2000). For a woman of average risk, it is estimated that the lifetime incidence of breast cancer is one in eight (Brooks, 2009). Breast cancer is particularly difficult to treat when it metastasizes and becomes resistant to antiestrogen therapies (Bernard-Marty, Cardoso, & Piccart, 2004). Therefore, early breast cancer detection has been the major factor in the reduction of mortality and reduction of cancer management costs (Fass, 2008).

6.1. TUMORIGENESIS

Breast cancer carcinogenesis is a multistep process, which takes different pathways, with mutations occurring in different genes and in distinct mammary cell types. This biological diversity is manifest in the existence of distinct clinically important tumor histological subtypes (Barros & Barros, 2009).

The initiation of tumorigenesis is caused by genetic alterations, which can be chromosomal translocations, deletions, point mutations or amplifications, and result in the loss of function of tumor suppressor genes (more frequent) or in the activation of proto-oncogenes (Gasco, Shami, & Crook, 2002). Relatively to its initiation process, breast cancers could be classified as sporadic or nonhereditary, which represent 90 to 95% of the cases and as hereditary or familiar, contemplating 5 to 10% of breast tumors (Samphao et al., 2009). Sporadic breast cancers occur in older women as a consequence of several accumulated somatic gene mutations. Hereditary or familial breast tumors are characterized by young age onset and bilaterality. This is due to a germline mutation in a single allele of high penetrance cancer susceptibility genes, such as *BRCA1*, *BRCA2*, *TP53*, *CDH1*, *CHEK2* or *PTEN*. Inactivation of the second allele of these tumor suppressor genes (loss of heterozigosity) is an early event in this oncogenic pathway (Knudson's "two-hit" model) (Knudson, 2001) .

In the phase of promotion, once the initial changes have occurred, the genetically modified cells stimulated by promoting factors expand and cause tumors

(Barros & Barros, 2009). The most important tumor promoters in mammary carcinogenesis are steroid hormones, whose influence on the breast depends on the stage of maturation and differentiation of duct-lobular unit. Estrogens are the main drivers in stimulating mammary cell proliferation, although its action is potentiated by the presence of progesterone (Osborne & Schiff, 2005).

Progression is associated with a breakdown of cadherin-mediated cell adhesion and consequent local invasion by tumor cells. Neoplastic cells, present in an initial tumor, can cross the subepithelial basement membrane and reach the underlying interstitial stroma. This allows malignant cells to access the lymphatic and/or blood vessels and eventually cause metastasis. These events mark the transition of *in situ* to infiltrating breast cancer. Neoangiogenesis is essential for tumor dissemination and metastasis; however the lymphatic spread of breast cancer is the preferred route (Schneider & Miller, 2005). The newly formed lymphatic vessels are larger than blood capillaries and have an incomplete basement membrane, which facilitates dissemination to the lymph nodes. Once in lymphatic organs, cancer cells can reach others organs. When breast cancer spreads, cancer cells most often seed in the bones (60%), lungs (20%), liver (15%) but rarely in brain, ovary and skin (Engel et al., 2003).

6.2. CLASSIFICATION

Breast cancer is biologically a heterogeneous disease. It encompasses several important tumor subtypes, each one with a distinct origin, genetic composition; evolution history and affected tissues (epithelial, mesenchymal and myoepithelial) (Burstein, 2005).

6.2.1. HISTOPATHOLOGICAL SUBTYPES

The histopathological classification of breast cancers is important for tumor diagnosis and consequently to determine patient prognosis. Each mammary gland is composed of multiple lobules connected to ducts and surrounding tissue (stroma), which includes blood and lymphatic vessels, nerves and adipose tissue. Breast cancers may originate from any of the mentioned tissues (Carvalho, 2009).

Ductal carcinoma *in situ* (DCIS) or non-infiltrative breast carcinoma is characterized by malignant epithelial cell proliferation confined to the mammary ducts, without crossover of the basement membrane (Pinder & Ellis, 2003).

Lobular intra-epithelial Neoplasia (LIN) is an uncommon disease and is characterized by noninvasive proliferative lobular lesions. LIN has been associated with an increased risk for developing invasive bilateral breast cancer (Hwang, Barke, Mendelson, & Susnik, 2008).

Concerning invasive breast carcinomas, the latest classification of the World Health Organization Classification of tumors (2003) distinguishes at least 30 invasive tumor types (Meijnen, Peterse, Antonini, Rutgers, & van de Vijver, 2008). The invasive ductal carcinoma (IDC) or infiltrating ductal carcinoma is the most common type of breast cancer, comprising 70-80% of all cases. It is frequently associated with DCIS. IDC commonly spread to the regional lymph nodes (Hawthorn, Luce, Stein, & Rothschild, 2010). The invasive lobular carcinoma is relatively uncommon, comprising only 8-15% of breast tumors. There are other histological types with distinct biological behavior (Carvalho, 2009).

6.2.2. GENETIC ALTERATIONS

The expression status of ER and progesterone receptors (PR) and the presence of HER2 gene (*HER2/neu*) amplification is important for breast cancer diagnosis. Gene expression profiling of several breast cancers has demonstrated the existence of five major molecular subtypes, including basal-like, luminal A, luminal B, $HER2^{+}/ER^{-}$ and normal breast–like (Perou et al., 2000). Importantly, these molecular divergences were shown to be associated with different clinical behavior and response to treatment (Sorlie et al., 2001).

The luminal types (A and B) are defined by high expression of ER and related genes (Morris & Carey, 2007). Luminal A breast cancers are associated with a better prognosis because patients respond better to hormonal therapy. In contrast, luminal B types are more resistant to this therapy (Rakha, Reis-Filho, & Ellis, 2010). The normal breast-like subtype expresses genes also expressed in adipose tissue and non-epithelial cell types (Sorlie et al., 2001). The HER2-positive subtype is characterized by high specific expression of HER2 (Perou et al., 2000). This protein receptor is important for cell growth regulation. When its gene is amplified, there is an overproduction of HER2 and activation of its downstream signaling pathways, thus leading to increased cell proliferation and concomitant development of aggressive tumors associated with poor patient prognosis. The basal-like subtype is characterized by low expression of the ER,

PR and HER2 genes in microarray analysis. Indeed, using clinical bioassays for breast cancer protein biomarker (ER, PR and HER2) detection, this histological subtype is frequently negative for ER, PR and HER2, so being often designated "triple-negative" (Dawson, Provenzano, & Caldas, 2009; Yezhelyev et al., 2006). There are limited effective options to treat patients with basal-like breast carcinoma, who have therefore poor prognosis (Draheim et al., 2010).

6.3. BREAST CANCER SCREENING AND DIAGNOSIS

Annual screening mammograms of asymptomatic women have been shown to reduce breast cancer mortality (Smart, Hendrick, Rutledge, & Smith, 1995). However, breast screening using MRI is more efficient for women with high risk for breast cancer development due to family history (Turnbulla, 2009). MRI showed a great potential in improving the detection of early stage breast cancers with small sizes in young, high-risk women without symptoms at clinical examination (Samphao et al., 2009).

Cancer cells often express characteristic antigens since their early onset. Using target probes for these molecular cancer markers, one can potentially improve the early diagnosis of cancer and thus treat it more efficiently (Brooks, 2009). Several biomarkers have been under clinical investigation for immunotherapy, targeted imaging of cancer, chemotherapy, and radiation therapy. Some have appeared to be valuable, though few have reached clinical applicability (Rakha et al., 2010).

Current histopathologic evaluation of breast cancer determines the ER/PR status, because their expression usually correlates with an enhanced response to chemo- or hormone therapy and consequently a better prognosis. The overexpression of HER2 is also important, because it enables the use of the trastuzumab (Herceptin) MAb (Yezhelyev et al., 2006). However, *HER2/neu* is only overexpressed in 25–30% of breast cancer patients (Sood, 2009). Other antigens have been used for targeted therapy and imaging of breast cancer, such as the carcinoembyonic antigen (Goldenberg et al., 2000), the tumor-associated antigen L6, the Thomsen-Friedenreich disaccharide (Goldenberg, 2002), the tumor-associated glycoprotein 72 (Macey et al., 1997) and EGFR (Ke et al., 2003).

7. AIMS OF THE PROJECT

The final aim of this research project is to develop pH-sensitive nanoparticles able to target specifically to cancer tissues a contrast agent for MRI. To verify the suitability of the newly designed pH-sensitive contrast agent for MRI molecular imaging, I had the following main goals:

1) Assess the *in vitro* cytotoxicity of free and micelle-encapsulated Gd(III) complexes;
2) Verify by MRI whether pH-sensitive micelles disassemble and release their content;
3) Confirm MUC1 gene and protein expression in breast cancer cell lines to be used as targets;
4) Verify whether micelle bioconjugation with a MUC1 antibody increased their targeting ability towards MUC1-expressing breast cancer cells;

CHAPTER II: MATERIALS AND METHODS

1. BIOCONJUGATION AND POLYMERIC MICELLE PREPARATION

The preparation of polymeric micelles, their bioconjugation, and encapsulation of Gd(III) complexes or fluorophore was performed based on a previously reported procedure (Mouffouk et al., 2008).

Preparation of Gd(III) complex solution

Hydrophobic Gd(III) complexes (tetra-aquodichloro (4,4'-ditBu-2,2'-bipyridine) gadolinium (III) chloride) were synthesized by Dr. André Lopes. The contrast agent was synthesized based on a well-described method to produce hydrophobic Gd(III) complexes with ligands such as bipyridine (Bechara et al., 2009). The resultant Gd(III) complex had a molar mass of 604.067 $g.mol^{-1}$. To obtain a 50 mM stock solution, 5.1 mg of Gd(III) complex were dissolved in 169 μL of ethanol (96%)(AGA). The solution was kept at -20ºC.

Preparation of Gd(III) complex-loaded polymeric micelles

Loaded polymeric micelles with Gd(III) complexes were obtained as follows: 30 mg of poly(ethylene glycol-*b*-trimethylsilyl methycrylate) and 0.5 mg of Gd(III) complexes were dissolved in 0.3 mL of N,N-Dimethylformamide (DMF) (BDH Prolabo). The mixture was stirred for 3 hours at room temperature. Subsequently, 0.7 mL of pure Milli-Q water was added at a rate of one drop every 10 s to induce micellization. The resulting micelle solution was then placed in a dialysis cassette (Thermo Scientific) with a 10 kDa cut-off and dialyzed against Milli-Q water for 1 day at room temperature. Then, 0.5 mL from the solution in the dialysis cassette were collected and the remaining was dialyzed for 3 days at room temperature. The Milli-Q water was replaced twice a day.

Preparation of fluorophore-loaded polymeric micelles

Polymeric micelles loaded with the 1-methylpyrene fluorophore were prepared by adding 30 mg of poly(ethylene glycol-*b*-trimethylsilyl methycrylate) to 0.5 mg of 1-methylpyrene (Fluka) and dissolved in 0.4 mL DMF. The mixture was stirred for 3 hours at room temperature. Subsequently, 1 ml of Milli-Q water was added at a rate of one drop every 10 s to induce micellization. The resulting micelle solution was then

placed in a dialysis cassette with a 10 kDa cut-off and dialyzed against Milli-Q water for 2 days at room temperature. The Milli-Q water was replaced twice a day.

Bioconjugation of polyethylene glycol with anti-MUC1

Bioconjugation of PEG with mouse MAbs against the human MUC1 protein (C595; Santa Cruz Biotechnology) was performed as follows: 3 mg of methoxypolyethylene glycol N-hydroxysuccinimide ester (Sigma-Aldrich) was added to a solution containing 3 µg of C595 (30 µL) in 0.1 M bicarbonate buffer (500 µL, pH=8.3). The mixture was gently stirred for 5 days in slow tilt rotation at 4°C.

Preparation of fluorophore-loaded bioconjugated micelles

Loaded bioconjugated micelles were prepared by adding 30 mg of poly(ethylene glycol-*b*-trimethylsilyl methycrylate) with 0.5 mg of 1-methylpyrene and dissolved in 0.4 mL of DMF. The mixture was stirred for 3 hours at room temperature. Subsequently, 0.5 mL PEG-Anti-MUC1 aqueous solution was added at a rate of one drop every 10 s and, immediately after, 0.5 mL of cold Milli-Q water was added at the same rate to induce micellization. The resulting micelle solution was then placed in a dialysis cassette with a 10 kDa cut-off and dialyzed against cold Milli-Q water for 1 day at 4ºC. The Milli-Q water was replaced once.

2. DETECTION OF NANOPARTICLES-BASED CONTRAST AGENT "ON" AND "OFF" STATES

To image Gd(III) complexes released from Gd(III) complex-loaded micelles a 1.5 Tesla (T) MRI (Signa 1.5T SYS#GEMSOW, GE Healthcare) was used. The same volume of Gd(III) complex-loaded micelles in Milli-Q water was dispensed in two microfuge tubes. Next, hydrochloric acid (HCL) (37%) (Merck) was added to one of these microfuge tubes. Both tubes were positioned above a MRI phantom for calibration**.** MR images were subsequently acquired with a Fast Spoiled Gradient Echo sequence (TR/TE= 150/4.2 milliseconds; Flip angle, 90º; slice thickness, 4 mm; field of view, 24x18 cm; matrix, 256x256).

The Gd(III) complex-loaded micelles were also tested in mice. One mouse was intramuscularly injected (50 µL) in one hind leg with 0.1 M Acetate buffer (pH=4). Subsequently, the mouse was intramuscularly injected (50 µL) with the pH-sensitive

polymeric micelles loaded with Gd(III) complexes in both hind legs. The mouse was then positioned inside a MRI head coil and MR images were subsequently acquired.

3. MEASUREMENT OF Gd(III) COMPLEXES AND FLUOROPHORE CONCENTRATIONS

1-methylpyrene calibration curve

From a stock solution of $2.17x10^{-5}$ M of 1-methylpyrene in tetrahydrofuran (THF, High-performance liquid chromatography (HPCL) grade, Ridel-de-Haën), five standards of concentrations $1.63x10^{-5}$, $1.09x10^{-5}$, $8.68x10^{-6}$, $5.43x10^{-6}$ and $1.09x10^{-6}$ M were prepared. The standard absorbances were measured (Varian Cary 50 UV-Vis spectrophotometer) at 344 nm and the calibration curve obtained by fitting the absorbance with concentration data. A value of $3.01x10^{4}$ $dm^3.mol^{-1}.cm^{-1}$ for the molar absorption coefficient was found. Given the calibration curve, the absorbance from two different samples, one of bioconjugated 1-methylpyrene-loaded micelles and other from non-target micelles was measured. For measurements, THF was added to 30 μL of a sample with unknown concentration until reaching 3 mL in the cuvette, obtaining a 100-fold dilution.

Gd(III) complex calibration curve

A stock solution of Gd(III) complex in ethanol (96%, AGA) $6.62x10^{-5}$ M was diluted to obtain standards with the following concentrations: $3.31x10^{-5}$, $1.66x10^{-5}$, $3.31x10^{-6}$, $1.66x10^{-6}$ and $3.31x10^{-7}$ M, whose absorbances were recorded at 282 nm. The molar absorption coefficient was $1,26x10^{4}$ $dm^3.mol^{-1}.cm^{-1}$.

4. CELL LINES AND CULTURE CONDITIONS

Cell Lines

The Jurkat (human T-cell leukemia), MCF-7 and MDA-MB-468 (human breast adenocarcinoma) cells lines were kindly supplied by Dr. João Barata (IMM, Lisbon), Dr. Raquel Seruca and Dr. Joana Paredes (IPATIMUP, Porto) respectively. The S17 (mouse bone marrow stromal) cell line was provided by Dr. Leonor Parreira (IMM, Lisbon). The HeLa (human cervical cancer) and 293T (human Embryonic Kidney) cell lines were provided by Dr. Guilherme Ferreira (IBB/CBME, Faro), the DND41 (human

T-cell leukemia) cell line by Dr. Hind Medyouf (Terry Fox Laboratory, Vancouver) and the human retinal pigment epithelium cell lines, ARPE19 and D407, by Dr**.** Gabriela Silva (IBB/CBME, Faro).

Cell Culture

The MCF-7, MDA-MB-468, HeLa, 293T; ARPE19; D407 and S17 adherent cell lines were maintained in DMEM medium (LONZA) supplemented with 10% fetal bovine serum (FBS) (PAA), 200 mM glutamine, 10000 units/mL penicillin and 10000 μg/mL streptomycin (LONZA). All cell culture incubations were performed at 37ºC under humidified atmosphere of 5% CO_2, unless stated otherwise. The Jurkat and DND41 suspension cell lines were maintained in RPMI 1640 medium (LONZA) supplemented as above. Cells were thawed at 37ºC and pipetted into 10 mL of pre-warmed medium. Cells were centrifuged at 300 g for 5 minutes to remove dimethylsulfoxide (DMSO) (Merck). Then, the supernatant was discarded and the pellet resuspended in 2 mL of fresh medium. The cells were placed into T25 flasks (Nunc) and 8 mL of medium was added for a final volume of 10 mL. The medium was changed every 2 days. To count adherent cells, these were first detached by removing the medium, followed by washing with phosphate-buffered saline (PBS) (LONZA) and addition of 1 mL of 0.25% trypsin (LONZA) per 59 cm^2. Then, the cells were allowed to detach for 1 to 5 minutes (depending on cell line) at 37ºC, before resuspension in DMEM medium. To dissociate cell aggregates, both suspension and adherent cells were gently pipetted. Then, 30 μL of cell suspension were placed into a microfuge tube together with 30 μL of 0.4% Trypan Blue (Sigma-Aldrich) and mixed. The hemocytometer Neubauer chamber (Hausser Scientific) was filled with the cell suspension and uncolored viable cells were counted on an inverted light microscope (Leica DM IL). The cells were counted in four 1 mm^2 squares. The equation to calculate the cell number per cubic millimeter is the following: number of cells counted per square millimeter × dilution used × 10.

5. IN VITRO CYTOTOXICITY TESTS

Cell counting to assess Gd(III) complex cytotoxicity

Jurkat cells were seeded on 6-well culture plates (BD Falcon) (2 mL in each well with a concentration of $2x10^5$ cells/mL). Different concentrations (1, 5, 10 and 50 μM) of Gd(III) complex solution, diluted in 50 μl RPMI1640, were added to the cells. Each test

was performed in duplicate. Untreated cells served as controls. Cells were incubated for 3 days, and each day cells were collected for counting.

MTT assay to assess cytotoxic Gd(III) complex concentrations

Two different cell lines were used to assess Gd(III) cytotoxicity: Jurkat, and MCF-7. Jurkat cells were seeded on two 96-well culture plates (BD Falcon) (50 μl in each well with a concentration of $4x10^5$ cells/mL). Different concentrations (5, 10, 15 and 20 μM) of Gd(III) complex solution, diluted in 50 μl of RPMI1640, were used. Each test was repeated eight times. As a negative control, cells were treated with ethanol (96%) (the same amount of ethanol given to cells treated with the highest concentration of Gd(III) complex). Incubation was carried out for 3 days. In this experiment the toxicity of Gd(III) complex was evaluated by the 3-(4, 5-dimethylthiazol-2-yl)-2, 5-diphenyl tetrazolium bromide (MTT) assay. This assay is based on the accumulation of formazan crystals inside living cells after their exposure to MTT. The reduction of MTT is attributed mainly to mitochondrial enzymes and electron carriers, so it only occurs in metabolically active cells. Destruction of cell membranes by the addition of an organic solvent resulted in the release and solubilization of the crystals. The amount of crystals can be determined spectrophotometrically and thus estimates the number of mitochondria and hence the number of living cells in the sample (Freimoser, Jakob, Aebi, & Tuor, 1999). At the end of each incubation time 10 μl of 5 mg/mL MTT solution (AppliChem) were added to each well followed by further incubation for 4h. Then, 100 μl of 0.04 N HCL in isopropanol (BDH Prolabo) were added to the wells and formazan crystals were allowed to solubilize for 1 hour at room temperature. The formazan concentration was quantified using a spectrophotometer (Tecan Infinite M200 monochromator-based multi-function microplate reader) by measuring the absorbance at 570 nm and 630 nm. The final optical density (OD) obtained from formazan formation was calculated with the following formula: $OD=L_{(570nm)}-L_{(630nm)}$. The toxicity was assessed by calculating the % of cell survival in relation to the control untreated group. The procedure described above was repeated for the MCF-7 cell line, after being seeded at 5×10^3 cells per each well and allowed to attach for 24h.

MTT assay to assess Gd(III) complex-loaded polymeric micelle cytoxicity

To assess Gd(III) complex-loaded polymeric micelle cytoxicity and to compare it with the toxicity from free Gd(III) complex, Jurkat cells were seeded on a 96-well culture

plate (50 μl in each well with a concentration of $4x10^5$ cells/mL). Different concentrations of Gd(III) complex and Gd(III) complex-loaded polymeric micelles dialyzed for 24 hours or for 96 hours (at concentrations of 10 μM or 50 μM) diluted in 50 μl of RPMI-1640 were added to the cells. Each test was performed in quadruplicate. Untreated cells, or cells treated with solvent (ethanol or Milli-Q water) served as controls. Cells were incubated for 72h. The cytotoxicity of Gd(III) complex and Gd(III) complex-loaded polymeric micelles was evaluated by the MTT assay following the procedure mentioned above. The results were analyzed by Student's *t*-test with $P < 0.05$ significance, using GraphPad Prism software.

6. ANALYSIS OF MUC1 EXPRESSION

6.1. SDS-PAGE AND WESTERN BLOTTING

Cell lysis in RIPA buffer

DND41 and trypsinized MCF-7 cell lines were washed twice in 1 mL of cold PBS. The supernatant was discarded and PBS removed without disturbing the cell pellet. Protein extracts were obtained by lysing cells in ice-cold RIPA buffer [10 mM Tris, pH 7.4; 150 mM NaCl; 1 mM EDTA; 1% Triton (100x); 0.5% Na deoxycholate; 0.1% SDS] with freshly added protease inhibitors (10 μg/mL aprotinin; 10 μg/mL leupeptin and 1 mM PMSF). 100 μL of RIPA buffer were added for each 10 million cells. After homogenization, the tubes were incubated on ice for 10 minutes. The cell debris was removed by centrifugation at 14000 rpm for 10 min and the cleared cell lysate transferred to a new microfuge tube. Samples were stored at -80ºC. For electrophoresis, 60 μL of each lysate were mixed with 60 μL of 2×SDS sample buffer (62.5 mM Tris, pH 6.8; 20% glycerol; 2% SDS; 5% β-mercaptoethanol; bromophenol blue). Subsequently the proteins were denaturated at 95ºC for 4 minutes.

SDS-PAGE

An 8% separating polyacrylamide gel was prepared using 30% acrylamide/bisacrylamide (37.5:1) (ProtoGel), 1M Tris (pH 8.8); 10% SDS, 10% ammonium persulphate (Applichem), N,N,N'N'-tetramethylethylenediamine (TEMED) Electran (BDH**),** and deionized water. A 4.5% stacking gel was prepared with the same reagents with exception of buffer, which was 5.5 M Tris, pH 6.8. The polymerized gels

were prepared on a mini-Protean (Bio-Rad) apparatus, following the manufacturer's instructions. Tris-glycine electrophoresis buffer (25mM Tris, pH 8.3; 192 mM glycine; 0.1% SDS) was added until gel submersion. Equal amounts **(**20 μL**)** of protein from MCF-7 and DND 41 cell lines were loaded onto the gel; and 5 μL of pre-stained high molecular weight protein markers **(**Precision Plus Protein Standards, Bio-Rad**)** were used as molecular weight standards. Gels were ran at 200 V constant voltage for approximately 45 minutes.

Western Blotting

Migrated proteins were electroblotted onto a 0.2 μm nitrocellulose membrane **(**Schleicher & Schuell). To this end, the gel was sandwiched between a pre-wet nitrocellulose membrane, six pieces of filter paper (Whatman 3MM) and fiber pads. The cassette was placed in the modular electrode assembly inside the buffer tank and filled with cooled transfer buffer (25mM Tris, 192mM glycine and 20% methanol). Electroblotting was carried out for 1 hour at 100 V constant voltage. Membrane blocking for 30 minutes and all antibody incubations were done at room temperature with 5% non-fat dried milk dissolved in 10 mL of PBS/0.1% Tween 20 (BDH Prolabo) **(**PBST**).** For protein detection, membranes were incubated sequentially with C595 MUC1 monoclonal antibody (diluted 1/500) for 1 hour and horseradish peroxidase (HRP)-conjugated goat anti-mouse (AbD SEROTEC), (diluted 1/1000) during 45 minutes. Excess antibodies were washed out 3 times during 10 minutes with PBST. All antibody incubations and washes were performed at room temperature with slow tilt oscillation**.** HRP detection was performed using the chemiluminescent detection kit, SuperSignal West Pico Chemiluminescent Substrate (Pierce), following the manufacturer's instructions. Chemiluminescence was revealed by exposing the nitrocellulose membrane to a radiographic film (Amersham Hyperfilm - GE healthcare Life Sciences). For antibody dehybridization, the nitrocellulose membrane was incubated during 30 minutes at room temperature with a solution of 100 mL of distilled water with 570 μL of 100% acetic acid, and submitted to 3 washes of 10 minutes with PBST. Then, it was incubated with α-tubulin monoclonal antibody **(**Sigma-Aldrich) **(**diluted 1/10000) for 1 hour. Signal detection was done as described above for MUC1 antibody.

6.2. RT-PCR

RNA Extraction

Total RNA was extracted from MDA-MB-468, MCF-7, Hela, 293T, ARPE19 and D407 cell lines as described below. The cells were cultured on 60 mm culture dishes and allowed to grow until sub-confluence. The medium was removed, culture dishes were washed with PBS and 1 mL of TRIZOL reagent (Invitrogen) was added directly to the cells. The cells were lyzed by repeated pipetting, and allowed to incubate at room temperature for 5 minutes. Subsequently, 0.2 mL of chloroform (BDH Prolabo) was added to the cells, mixed and allowed to incubate at room temperature for 10 minutes. Next, the tubes were centrifuged at 12000 g, for 10 minutes at 4ºC, and the aqueous phase transferred to a new clean 2 mL microfuge tube. To precipitate RNA, 0.5 mL of isopropanol (BDH Prolabo) was added to the aqueous phase and mixed. The samples were incubated at room temperature for 10 minutes. Then, the samples were centrifuged at 12000 g, for 10 minutes at 4ºC. The supernatant was discarded, and 1 mL of 75% RNase-free ethanol was added, mixed by vortexing and centrifuged at 7500 g for 5 minutes at 4ºC. The supernatant was discarded and the samples were allowed to dry by vacuum for 10-15 minutes. Depending on the size of the obtained visible RNA pellet, 20 to 50 μL of RNase-free water was added to dissolve the pellet, and incubated for 10 minutes at 60ºC. The concentration and purity of isolated RNA was measured by NanoDrop 2000c Spectrophotometer (Thermo Scientific), and its quality assessed by 1% agarose (LONZA) gel migration in TAE buffer (40 mM Tris-Acetate; 0.5 mM EDTA, pH 8.5). The RNA samples were stored at -80ºC.

DNase treatment

Treatment of RNA with DNase I, RNase-free (Fermentas, #EN0521) was performed to obtain DNA-free RNA for RT-PCR. Thus, 1 μg of RNA in 9 μL of DEPC-treated water was added to 1 μL of reaction buffer (10x) [100 mM Tris-HCl (pH 7.5 at 25ºC), 25 mM $MgCl_2$, 1 mM $CaCl_2$] and 1 μL of DNase enzyme (1 U/ μL). The reagents were mixed, centrifuged to collect drops, incubated at 37ºC for 30 minutes and briefly centrifuged again. Then 1 μL of 25 mM EDTA was added, and the solution incubated at 65ºC for 10 minutes to inactivate the enzyme. After incubation the samples were used as templates for reverse transcription.

Reverse transcriptase reaction

Reverse transcription was conducted using the RevertAid First Strand cDNA Synthesis Kit (Fermentas, #K1621) according to the manufacturer's intructions. To the previously obtained 11 μL of DNase-treated RNA, 1 μL of oligo $(dT)_{18}$ primer (0.5 μg/ μL) was added. The sample was mixed, briefly centrifuged to collect drops and incubated at 70ºC for 5 minutes. Then, the mix was cooled on ice and shortly centrifuged. Next, 4 μL of reaction buffer (5x) [250 mM Tris-HCL (pH 8.3), 250 mM KCl, 20 mM $MgCl_2$, 50 mM DTT], 1 μL of RiboLock Ribonuclease Inhibitor (20U/ μL), and 2 μL of dNTP mix (10 mM) were added. The mix was briefly centrifuged and incubated at 37ºC for 5 minutes. Afterwards, 1 μL of RevertAid M-MuLV Reverse Transcriptase (200 U/ μL) was added to the mixture, and this was incubated at 42ºC for 60 minutes. To stop the reaction, the mix was heated at 70ºC for 10 minutes. Finally, the sample was cooled down on ice and stored at -20ºC.

Polymerase chain reaction (PCR)

For PCR amplification a mix was prepared composed of: 2 μL of DNA sample, 5 μL Go Taq Flexi reaction buffer (5x) (without $MgCl_2$), 1.5 μL of $MgCl_2$ (25 mM); 0.5 μL of dNTP (10 mM), 1 μL of forward primer and 1 μL of the reverse primer (12.5 μM), 0.1 μL of GoTaq DNA polymerase (5 U/μL) and sterile deionized water until a final volume of 25 μL. All the reagents mentioned above were from Promega with the exception of dNTPs (Fermentas). The PCR reaction was performed in a thermal cycler (MyCycler, Bio-Rad) with the following program: an initiation step of 95ºC for 2 minutes, followed by 30 cycles of denaturation at 95ºC for 1 minute, annealing at 55ºC for 1 minute and elongation at 72ºC for 30 seconds. A final elongation step of 72ºC for 5 minutes was also performed. The *MUC1* transcript was amplified using the following primer sequences, designed using Primer3 software and synthesized by Sigma-Aldrich: Forward, 5'-GTG CCC CCT AGC AGT ACC G-3'; and Reverse, 5'-GAC GTG CCC CTA CAA GTT GG-3'. After PCR amplification, 10 μL of each PCR reaction product and 5 μL of 100 pb ladder (Bioron) were loaded into a 2% agarose gel and electrophoresed in TAE buffer. The PCR products were visualized with a UV light transilluminator attached to a digital camera (Gene FLASH).

6.3. REAL-TIME PCR

For real-time PCR, we used the iQ SYBR Green Supermix kit (Bio-Rad) following the manufacturer's instructions. The cDNA samples obtained as described before, were used at a 1/20 dilution. A master mix was prepared for each pair of primers with 9.7 μL of H_2O, 0.4 μL of forward primer, 0.4 μL of reverse primer (both at 12.5 μM) and 12.5 μL of SYBRr Green Master Mix (2x). For *MUC1* detection we used the primers described above. For *ACTB* detection, used as a reference gene, we used the following primers: Forward, 5'-AGG CCA ACC GCG AGA AGA TGA C-3' and Reverse, 5'-AGG TCC AGA CGC AGG ATG GCA T-3' (Villablanca et al., 2008), synthesized by Sigma-Aldrich. The master mix was distributed on 96-well ABgene PCR plates (Thermo Scientific, AB-0700), 23 μL per well, together with 2 μL of sample cDNA (each sample in triplicate). Water was used as negative control. The PCR microplate was covered with adhesive PCR film (Thermo Scientific, AB-0558). The real-time PCR was performed on a CFX96 Real-Time PCR Detection System (Bio-Rad). Relative mRNA expression levels were calculated through the $2^{-\Delta\Delta Ct}$ method (Livak & Schmittgen, 2001).

6.4. FLOW CYTOMETRY

Flow cytometry was performed on trypsinized MCF-7 and MDA-MB-468 cells, resuspended in cold PBS. $5x10^5$ cells of each cell line were dispersed by gently aspirating with a pipette, placed in each of three 5 ml FACS tube (BD Falcon) and resuspended in 1mL of cold FACS buffer [3% Calf Serum (CS) (PAA), 10 mM NaN_3 in PBS]. Two of the three FACS tubes of each cell line were centrifuged at 300 g for 5 minutes. The supernatant was discarded, the cell pellet of one FACS tube was incubated with 50 μL of C595 antibody (1:100 in FACS buffer) and the other tube with α-tubulin antibody (1:500 in FACS buffer). The incubation was carried out for 1 hour. Then, the cells were washed twice with 1 mL of FACS buffer and then incubated with phycoerythrin-conjugated goat anti-mouse immunoglobulins (GAM-PEs) (Biolegend) diluted 1:100 in FACS buffer, in the dark for 30 minutes. As a control group, $5x10^5$ cells were incubated with GAM-PE only. The cells were washed as above and resuspended in 1mL of 10 mM NaN_3 in PBS. All the mentioned steps were performed at 4ºC. Finally the cells were analyzed using the BD FACSCalibur (BD Biosciences) equipped with the Cell Quest software package (BD Biosciences).

7. ASSESSMENT OF SPECIFIC TARGETING OF BIOCONJUGATED MICELLES

7.1. FLOW CYTOMETRY

MDA-MB-468 and S17 cells were seeded on 12-well culture plates ($6x10^4$ cells/well in 600 μL of DMEM) and allowed to attach for 24 hours. Then, 200 μL of anti-MUC1-targeted and non-targeted micelles with encapsulated fluorophore were added to each cell line. Cells were incubated with targeted micelles or non-targeted micelles for 15 or 30 minutes at 37ºC. Untreated cells were used as negative control. After incubation, the medium was discarded and the cells were washed 3 times with 1 mL cold PBS. Subsequently, the cells were detached with 0.25% trypsin and resuspended in 1 mL cold PBS. These samples were filtered through a cell-strainer cap (BD Falcon) to 5 mL FACS tubes. The cells were centrifuged at 300 g for 5 minutes and resuspended in 1 mL of cold PBS. All the mentioned steps were performed at 4ºC. Finally the cells were analyzed using the BD FACSAria II Multicolor cell sorter (BD Biosciences) and data were examined by Cell Quest software package (BD Biosciences). Excitation of 1-methylpyrene was at 407 nm, and the emission spectrum was detected from 430 to 470 nm.

7.2. FLUORESCENCE MICROSCOPY

Without cell fixation

MCF-7 cells were seeded in 96-well culture plates (50 μl in each well with a concentration of $5x10^3$ cells per well) and allowed to attach for 24 h at 37ºC. Micelles bioconjugated with C595 (25 μl) and loaded with 1-methylpyrene were added to the cells and incubated for 1 hour at 37ºC. As a control, we used unconjugated 1-methylpyrene-loaded polymeric micelles. Excess micelles were removed by washing three times with PBS. Microscopy observations of cells before and after micelle washing were performed with an inverted fluorescent microscope (Leica DM IL). Images were acquired with a digital CCD camera (Evolution MP-5.1, Media Cybernetics). Images were processed using Adobe Photoshop CS2 software (AdobeSystems).

With cell fixation

Sterile 13 mm glass coverslips (VWR) were placed inside two wells of a 12-well culture plate. On one of those wells, MDA-MB-468 and S17 cells were seeded with the proportion of 1 to 5; on the other well MFC-7 and S17 cells were seeded with the same proportion. To both wells, 600 μL of DMEM medium were added to make a final concentration of $6x10^4$ cells per well. The cells were allowed to attach for 24 hours at 37ºC. Then, 200 μL of anti-MUC1 fluorophore-loaded micelles were added to the cells and incubated for 1h at 37ºC. Then, the cells were washed 3 times with 1 mL of PBS and fixed with 600 μL of paraformaldehyde (4%) (Sigma-Aldrich) for 30 minutes. The cells were washed once with 1 mL of PBS, and each coverslip was collected from the wells with forceps and layed onto a microscope slide (Menzel-Glaser) and covered with a Mowiol mounting (Hoechst). The glass slides were kept cold overnight. Microscopic observations of fixed cells were performed with Axio Observer Z2 Fluorescence microscope (Zeiss). Images were acquired with a digital AxioCam (Zeiss) and were processed using AxioVision is the software (Zeiss).

CHAPTER III: RESULTS

1. DEMONSTRATION OF MICELLE pH-SENSITIVE MECHANISM OF CONTENT RELEASE

The pH sensitivity of Gd(III) complex-loaded micelles was visualized in a clinical MRI. A T_1WI of two microfuge tubes containing Gd(III) complex-loaded micelle solution was imaged using a 1.5T MR scanner.

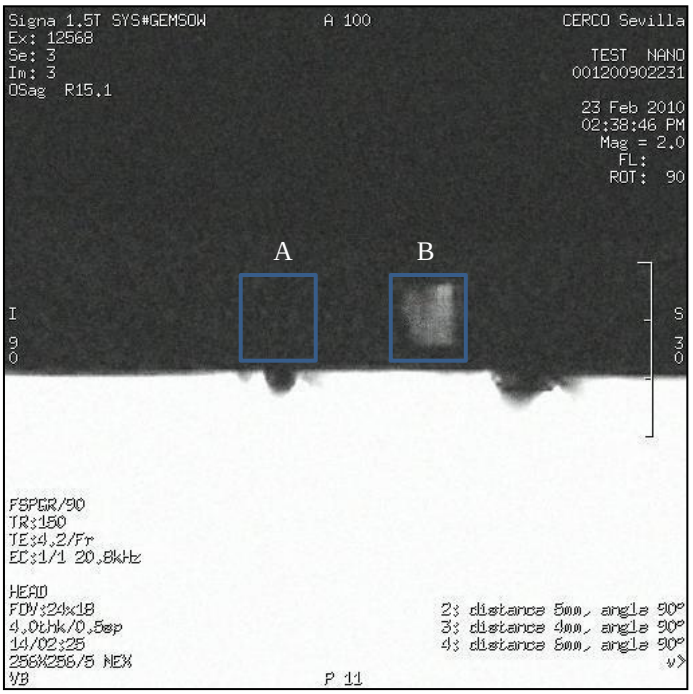

Figure 13 – Demonstration of pH-sensitive nanoparticle content release. A T1WI was acquired using a clinical 1.5T MRI scanner. This image shows the recovery of the imaging capability of the contrast agent at low pH, because no image signal was visible from the sample with intact nanoparticles (square A) whereas the sample at low pH generated a signal enhancement (square B).

The sample with intact micelles did not provide an image signal (Figure 13, square A). In contrast, the sample at low pH presented a signal enhancement which was visible as a bright signal (Figure 13, square B). These results indicate that micelles decomposed and released the Gd(III) complexes, allowing them to interact with surrounding water molecules, thus decreasing their T_1 times and increasing the image signal intensity from that specific area.

The pH sensitivity of Gd(III) complex-loaded micelles was also testedin mice.

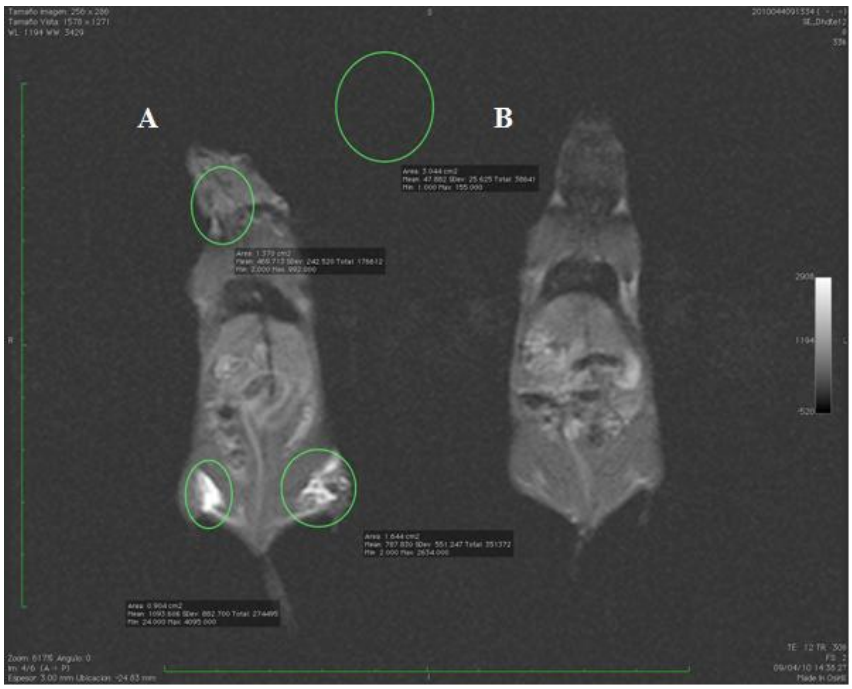

Figure 14 - Demonstration of pH-sensitive nanoparticle content release in *in vivo*. A T1WI was acquired using a clinical 1.5T MRI scanner. This image shows a signal enhancement from both hind legs of mouse injected with pH-sensitive micelles loaded with Gd(III) complexes (A). A stronger signal was obtained from the right hind leg, which was previously injected with an acid solution. A non-injected mouse is shown as control (B).

Both legs of mouse that had been injected with our pH-sensitive micelles loaded with Gd(III) complexes, appeared bright on MR image (Figure 14-A), indicating the release of the contrast from the micelles into the leg muscles. The previous intramuscular injection of an acidic solution in the right hind leg led to increased signal enhancement, indicating that artificially creating an acidic environment facilitated the Gd(III) complex release.

2. IN VITRO CYTOTOXICITY TESTS

To assess the cytotoxicity of free Gd(III) complexes we tested the effect of incremental concentrations of two different cell lines, Jurkat, a suspension leukemia cell line, and MCF-7, an adherent breast cancer cell line. Toxicity was represented as the number of viable cells per mL (Figure 15) or as the percentage of viable cells relatively to the control untreated group (Figure 16 and 18).

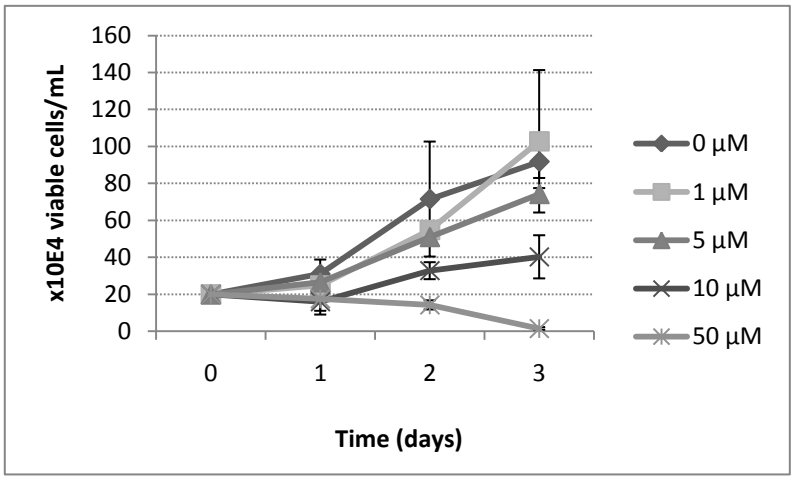

Figure 15 – Cytotoxicity of free Gd(III) complexes by cell count. Comparison of cytotoxicity of varying concentrations of Gd(III) complexes using cell count with Trypan Blue on Jurkat cell line, during 3 days. Data represent the means of duplicate ± standard deviation.

Free Gd(III) complexes were toxic for Jurkat cells at concentrations of 10 to 50 µM (Figure 15). At 10 µM, the complexes were less toxic for the cells, since even after 3 days of incubation a slight increase in cell growth was observed. In contrast, at 50 µM the complexes were very toxic, causing a progressive cell death with time.

We also evaluated the cytotoxicity of Gd(III) complexes using the MTT assay, another method measuring cell viability, on the Jurkat and MCF-7 cell lines (Figure 16 and 18). By doing so, we verified that 10 µM of Gd(III) complexes are toxic for both cell lines , significantly decreasing the number of viable cells (Figure 16). In order to estimate the concentration of Gd (III) complexes able to reduce cell viability by 50% (IC_{50}), we plotted a linear regression line for each cell line studied (Figure 17). Thus, the IC_{50} for the MCF-7 cell line was 12.8 µM of Gd(III) complexes (Figure 17-A). For

Jurkat cells the IC_{50} was 10.2 μM of Gd(III) complexes (Figure 17-B). It appears thus that Jurkat cells are slightly more susceptible to Gd (III) complexes than MCF-7 cells.

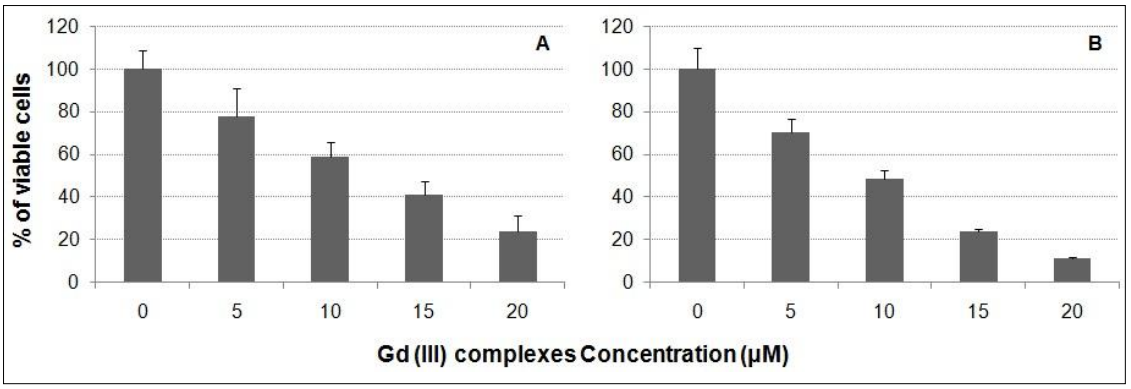

Figure 16 – Cytotoxicity of free Gd(III) complexes by MTT assay. Comparison of cytotoxicity of varying concentrations of Gd(III) complexes using MTT assay on MCF-7 (A) and Jurkat (B) cell lines. The test was performed at the end of 3 days of treatment. Data represent the means of eight testes + standard deviation.

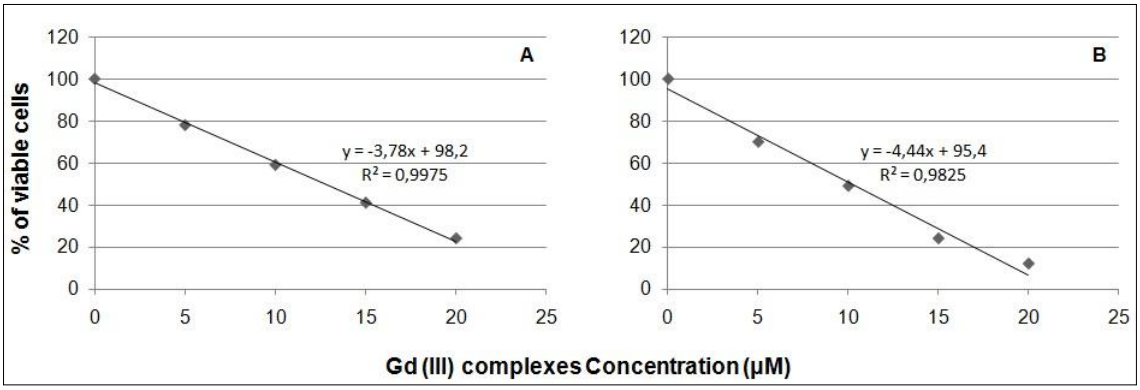

Figure 17 – Linear regression line for cytotoxicity of free Gd(III) complexes. A linear regression line was calculated from data obtained by MTT assay, to be used as a standard curve to find the concentrations of Gd(III) complexes to reduce cell viability to 50% of control values for MCF-7 (A) and Jurkat (B) cell lines.

To compare the cytotoxicity of free and micelle-encapsulated Gd(III) complexes and to verify if the time of dialysis influences polymeric micelle cytotoxicity, we performed the MTT assay on Jurkat cells. The cells were treated with incremental concentrations of the free and micelle-encapsulated Gd(III) complexes. Thus, we verified that encapsulation of Gd(III) complexes inside polymeric micelles greatly decreased their toxicity (Figure 18). The difference in cytotoxicity was most evident at 50 μM, the highest concentration tested. At this concentration, encapsulated Gd(III)

complexes reduced viability to approximately 70-85% of untreated controls, while free Gd(III) complexes killed almost all cells (Figure 18).

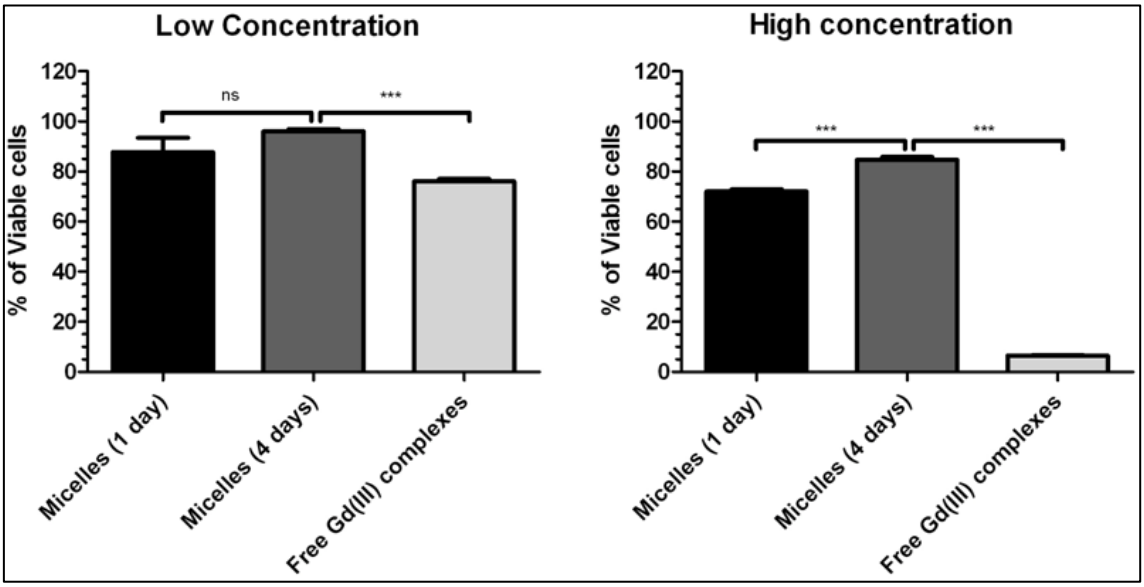

Figure 18 – Cytotoxicity comparison of free and nanoparticle-encapsulated Gd(III) complexes. Comparison of cytotoxicity of low (10μM) and high (50μM) concentrations of free and nanoparticle-encapsulated Gd(III) complexes using MTT assay on Jurkat human leukemia cell line, after 3 days of incubation . Micelles dialyzed for 4 days were compared with micelles dialyzed for 1 day. Data represent the means of quadruplicate + standard error of the mean (***$p \leq 0.0001$; ns, nonsignificant).

Micelles presented at both concentrations significantly less cytotoxicity than free Gd(III) complexes. Micelles that were maintained under dialysis for 4 days were significantly less toxic at 50 μM than those maintained in dialysis for 1 day. However at low concentration (10 μM) the difference in cytotoxicity between the two micelle formulations is not significant (Figure 18). This experiment confirmed that 50 μM of Gd(III) complexes kill all cells, as previously verified by cell counting (Figure 15).

3. ANALYSIS OF MUC1 GENE AND PROTEIN EXPRESSION

Once verified the pH-dependent release mechanism and the little cytotoxicity of the Gd(III)-loaded nanoparticles, we wished to develop micelles bioconjugated with an anti-human MUC1 MAb (C595) to use them for active targeting. However, before initiating specific targeting tests, we verified the levels of MUC1 gene and protein

expression in the cell lines used for targeting. MUC1 mRNA expression was assessed by both standard and quantitative RT-PCR, whereas MUC1 protein expression was detected by Western Blotting and flow cytometry (Figures 19 to 22). (The concentration, purity and quality of RNA isolated from the different cell lines are available on appendix A.

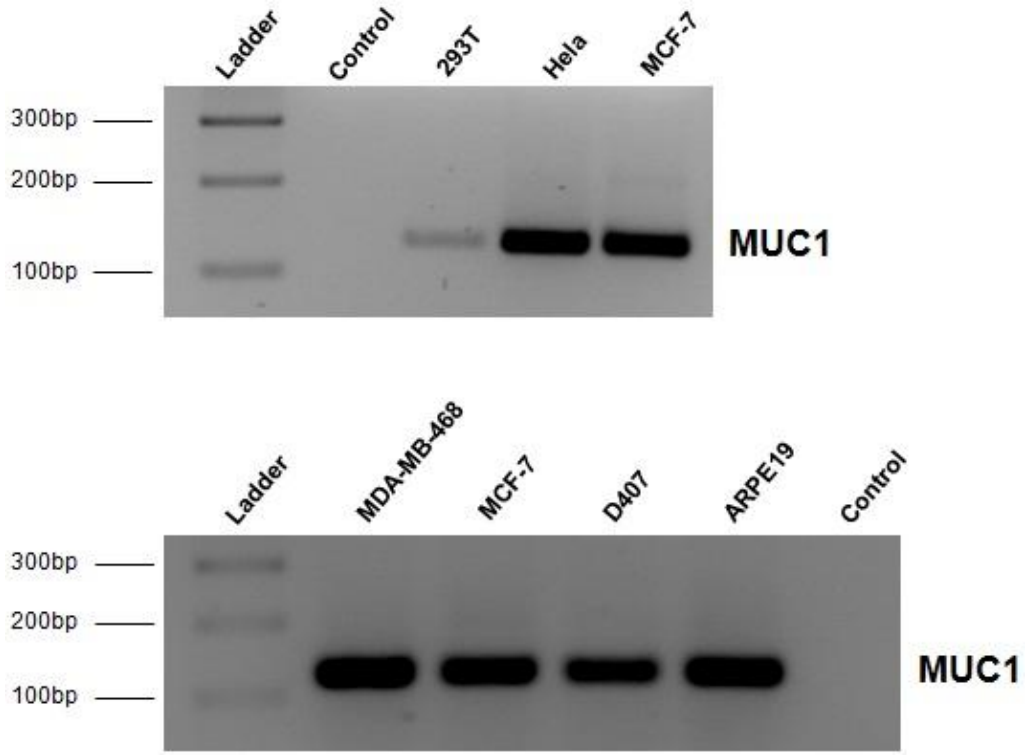

Figure 19 – Detection of *MUC1* expression by RT-PCR. MUC1 mRNA was expressed by all used cell lines; the highest expression was shown by MDA-MB-468 cells. DNA marker (100-600 bp ladder).

RT-PCR analysis revealed MUC1 gene expression not only in the MDA-MB-468 and MCF-7 human breast adenocarcinoma cells but also in other epithelial cell lines, such as Hela, 293T, ARPE19 and D407 (Figure 19). MDA-MB-468, MCF-7 and Hela cells appeared to present stronger RT-PCR signal, compared to ARPE19, D407 and 293T cells. To assess more accurately the expression of *MUC1* in the different cell lines we performed real-time RT-PCR.

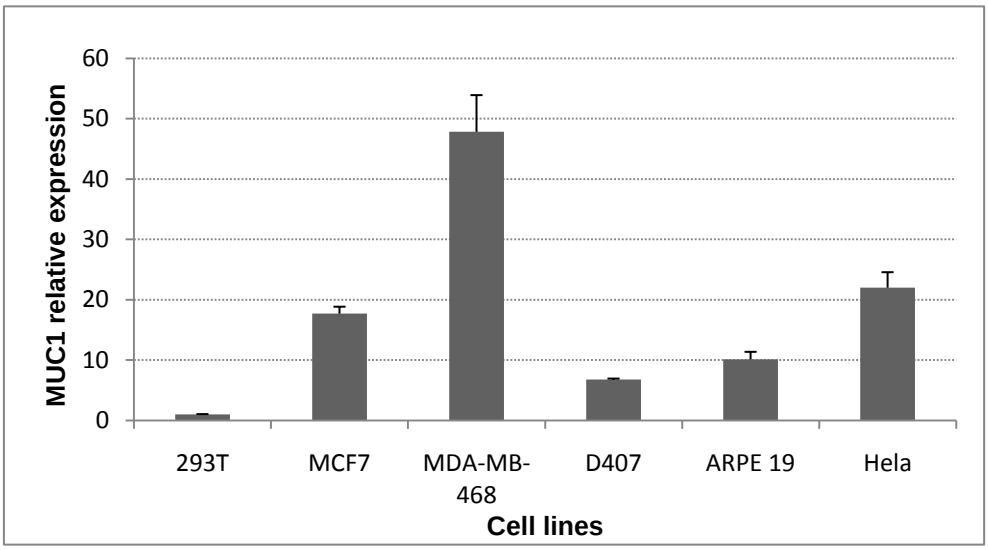

Figure 20 – *MUC1* relative expression, in different cell lines, by real-time PCR analysis. The highest *MUC1* expression was shown by MBA-MB-468 human breast adenocarcinoma cell line, when compared to other examined cell lines.

By doing so, we verified that MDA-MB-468 presented the highest levels of *MUC1* expression, when compared to the other cell lines (Figure 20). Hela and MCF-7 cell lines showed similarly high levels of *MUC1* expression, while the ARPE 19 and D407 retinal epithelial cell lines displayed reduced expression of *MUC1*. The human embryonal kidney 293T cell line had residual expression as compared to other cell lines.

To confirm the RNA expression studies and detect MUC1 protein expression, we performed Western Blotting and flow cytometry. We analyzed the DND41 and MCF-7 cell lines by Western Blot. The α-tubulin detection by Western blotting is shown in appendix B.

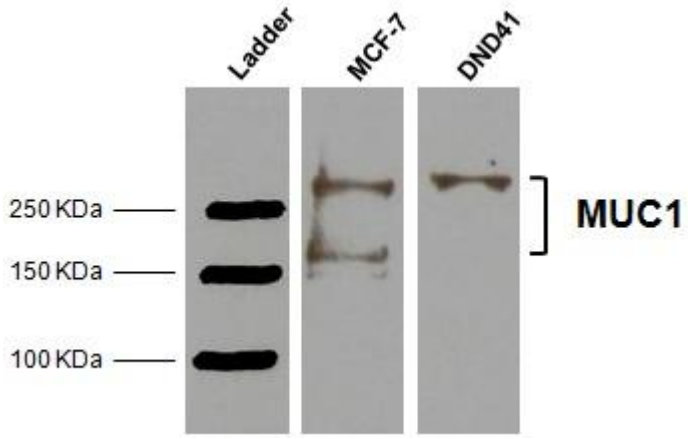

Figure 21 – Detection of MUC1 glycoprotein in homogenates of MCF-7 breast cancer cells and DND41 acute lymphoblastic leukemia cells by SDS-PAGE and Western Blotting. The reaction with anti-MUC1 antibody confirmed the presence of MUC1 in MCF-7 homogenates.

Western blotting using the C595 MAb revealed the expected high-molecular-weight polymorphic MUC1 bands (Figure 21), demonstrating the presence of protein in MCF-7 homogenates. DND41 also expressed MUC1 protein. However, since this cell line presented just one band, only one isoform of MUC1 is present.

To verify the presence of MUC1 protein at the cell surface of breast cancer cell lines and to compare the expression levels between MDA-MB-468 and MCF-7 cells, we performed flow cytometry using the C595 antibody and a fluorophore-conjugated secondary antibody.

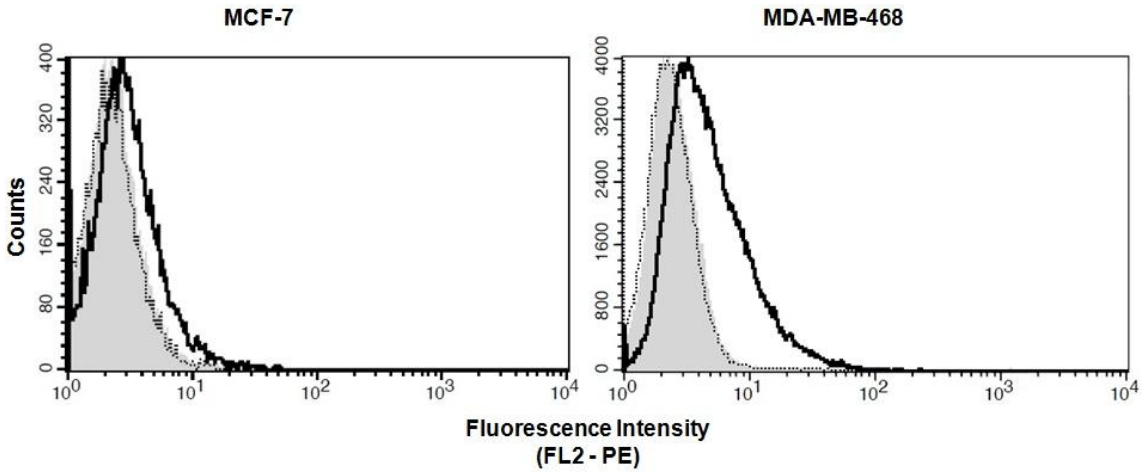

Figure 22 – Analysis by fluorescent flow cytometry to detect MUC1 cell surface expression on MCF-7 and MDA-MB-468 cell lines. MUC1 expression was detected on both cell lines using the anti-MUC1 extracellular domain, C595 MAb (black line). The discontinuous black line indicates reactivity with an irrelevant antibody of the same isotype. The grey shaded region is the control group.

The C595 antibody conferred more fluorescence signal to the cell lines than an irrelevant antibody, indicating that the MUC1 protein is expressed at the cell surface of MCF-7 and MDA-MB-468 cell lines (Figure 22). The MUC1 cell surface expression levels were higher for MDA-MB-468 cells than for MCF-7 cells (Figure 22), which confirms results obtained with quantitative RT-PCR.

4. ASSESSMENT OF SPECIFIC TARGETING OF BIOCONJUGATED NANOPARTICLES

An important feature of the designed nanoparticles, besides the pH-sensitive release mechanism, is the ability to specifically target MUC1-expressing cells. This characteristic should prevent the random accumulation of these nanoparticles on undesired tissues, and confer a real target capability to these nanoparticles. To test this property we used 1-methylpyrene fluorophore loaded into micelles instead of Gd(III) complexes, because of the feasibility of fluorescence detection in cells. The first step towards this aim was to bioconjugate fluorophore-loaded micelles with the anti-MUC1 antibody, C595. The next step was to verify the capability to specifically target MUC1-expressing cells.

For targeting experiments and flow cytometry detection of 1-methylpyrene incorporation, we used the MDA-MB-468 cell line, which displayed the highest levels of MUC1 expression (Figure 22), and the S17 cell line, which derives from mouse bone marrow stroma. Since the antibody used against MUC1 is specific for the human protein, the S17 mouse cells were used as a negative control. For this experiment, bioconjugated and non-targeted fluorophore-loaded micelles were incubated for different periods of time with both cell lines. Before analysis, the cells were thoroughly washed to eliminate unbound nanoparticles.

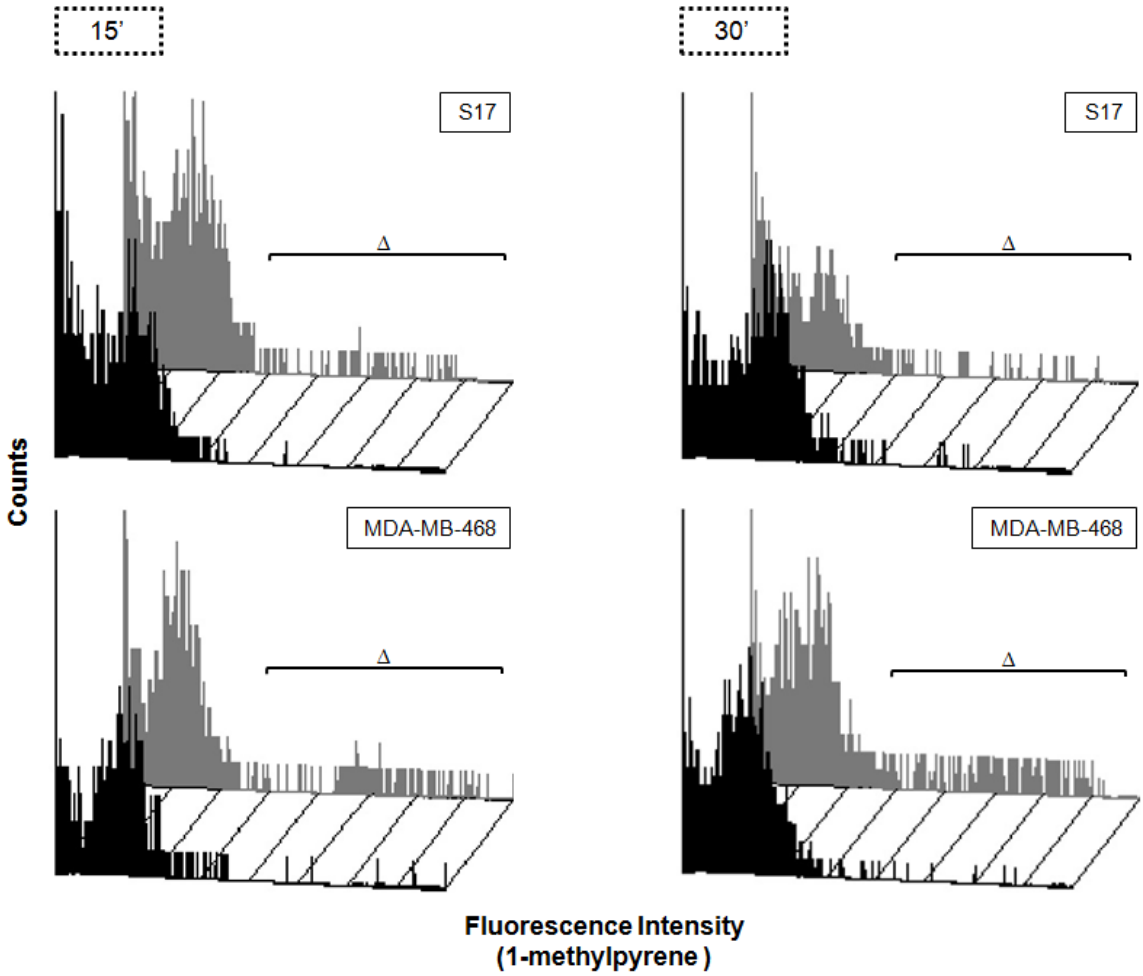

Figure 23 – Fluorescent flow cytometry to assess specific targeting of Anti-MUC1 bioconjugated 1-methylpyrene loaded nanoparticles. An enhancement in fluorescence intensity is evident on MDA-MB-468 cells which were incubated for 15 minutes and for 30 minutes with Anti-MUC1 bioconjugated nanoparticles (gray shaded region) comparing with S17 cells. The black shaded region indicates the fluorescent enhancement due to cell incubation with non-targeted 1-methylpyrene loaded nanoparticles. Delta symbol (Δ) designates the fraction of cells that showed a fluorescent intensity enhancement due to uptake of 1-methylpyrene-loaded nanoparticles. Delta values are presented on table 2.

Table 1 – Delta (Δ) values. Those values represent the fraction of cells (in percentage) which showed a fluorescent intensity enhancement due to uptake or attach of 1-methylpyrene loaded nanoparticles.

Incubation Time (minutes)	S17 cells		MDA-MB-468	
	Non-targeted micelles	**Anti-MUC1 micelles**	**Non-targeted micelles**	**Anti-MUC1 micelles**
15	0.8%	2.17%	2.06%	6.34%
30	2.07%	2.3%	0.74%	8.41%

MDA-MB-468 cell incubation with C595 bioconjugated micelles led to a higher percentage of fluorescent cells than incubation with nontargeted micelles (Figure 23; Table 1). In contrast, incubation of C595 bioconjugated micelles did not increase the proportion of fluorescent S17 cells, which do not express human MUC1, as compared to nontargeted micelles. The superior target capability and consequent fluorescence enhancement in MUC1-expressing MDA-MB-468 cells, was demonstrated by the fluorescent enhancement of 6.3-8.4%. Despite the improved uptake of 1-methylpyrene by MUC1-expressing MDA-MB-468 cells, we also observed some degree of unspecific uptake, as demonstrated by the presence of approximately 2% fluorescent S17 cells after incubation with either C595-conjugated or unconjugated micelles, and 2% fluorescent MDA-MB-468 cells after incubation with non-targeted micelles (Table 1).

We also aimed to visualize by fluorescence microscopy 1-methylpyrene incorporation into cells upon incubation with micelles loaded with this fluorophore. MCF-7 cells were incubated for 1 hour with targeted and non-targeted micelles, and then observed using an inverted fluorescence microscope. MCF-7 cells incubated with anti-MUC1 micelles presented more fluorescent staining than cells incubated with non-targeted micelles (Figure 24).

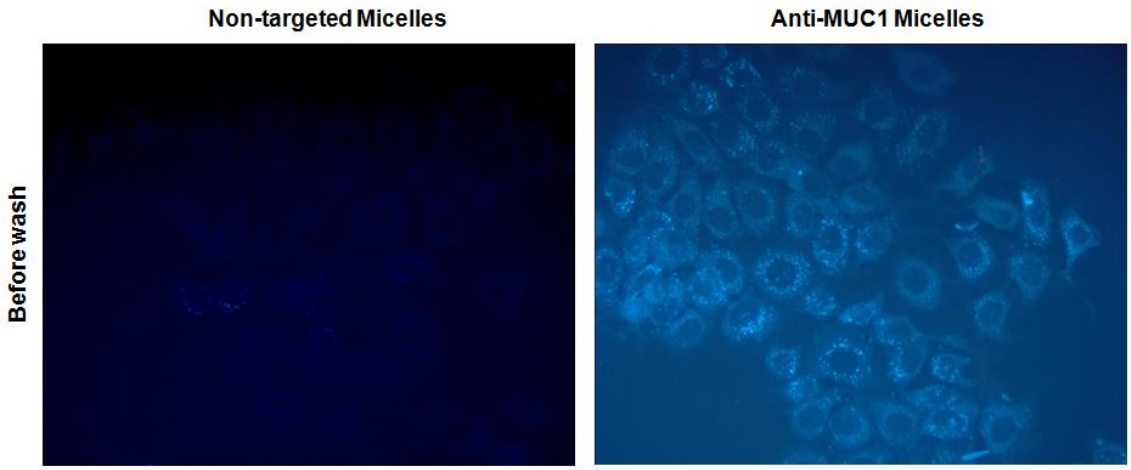

Figure 24 – Specific binding of anti-MUC1 1-methylpyrene-loaded micelles to MCF-7 breast cancer cells. At the end of an incubation period of 1 hour, it was evident the differential uptake of non-targeted and anti-MUC1 micelles by MCF-7 cells.

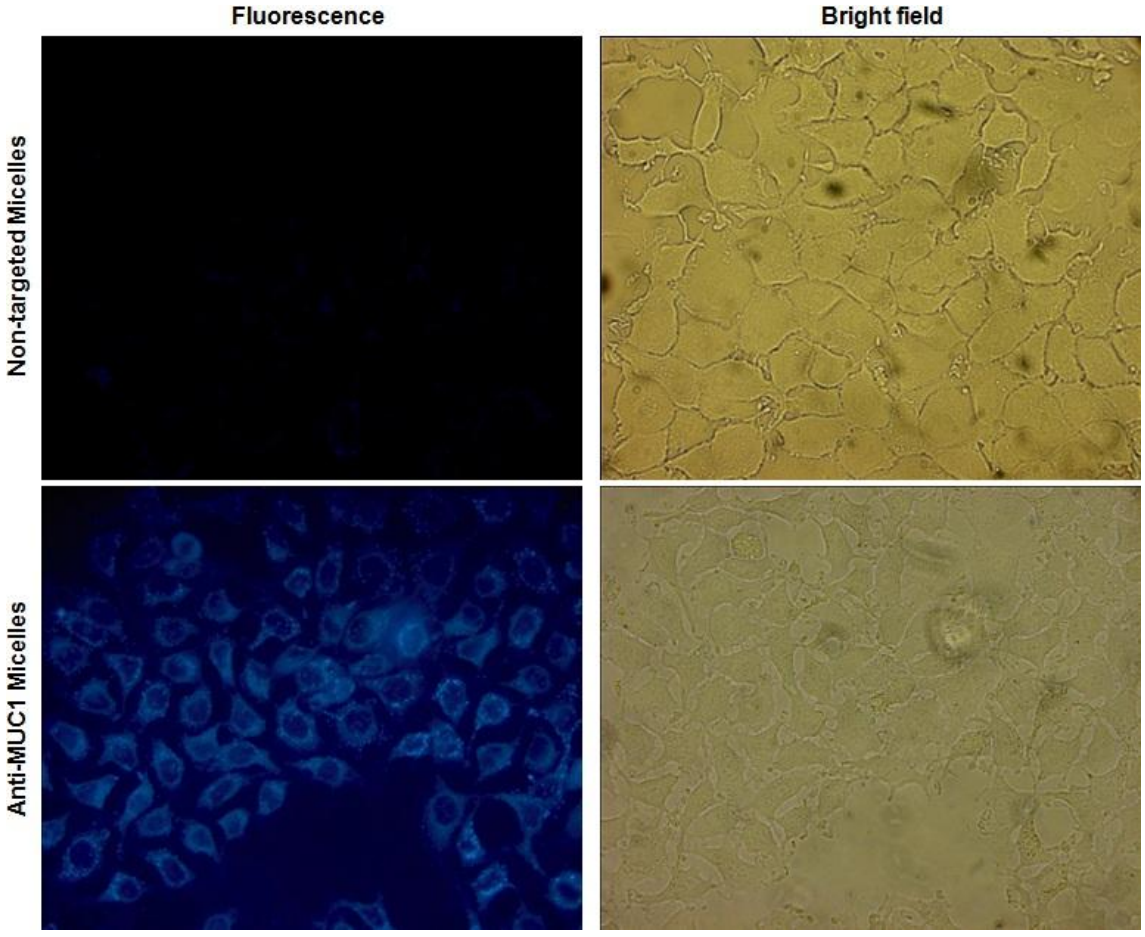

Figure 25 – Specific binding of anti-MUC1 1-methylpyrene-loaded micelles to MCF-7 breast cancer cells, after washes. After washing 3 times high 1-methylpyrene fluorescence was found in cells incubated with anti-MUC1 polymeric micelles, while a low level of background fluorescence was visible in MCF-7 cells incubated with non-targeting micelles.

MCF-7 cells were also observed after washing with PBS, and again cells incubated with anti-MUC1 micelles presented much higher fluorescence levels than cells incubated with non-targeted micelles (Figure 25). Together, these results demonstrate the specificity of the targeted nanoparticles to MUC1-expressing cells and demonstrate that micelles release their content within cells.

Next we used another approach to test the specificity of anti-MUC1 micelles. The goal here was to observe if anti-human MUC1 nanoparticles were able to specifically target MDA-MB-468, even when these cells were mixed in a lower proportion (1 to 5) with mouse S17 cells. The mixed culture was incubated with anti-MUC1 polymeric micelles for 1 hour and washed several times with PBS before observation at the fluorescence microscope. By doing this, we observed that MDA-MB-468 cells, which display rounded morphology (Figure 26-B), incorporated more 1-methylpyrene fluorescence (Figure 26-A) than S17 cells, which display elongated morphology (Figure 26-C). Indeed, round (MDA-MB-468) cells presented bigger and brighter spots than elongated (S17) cells in the mixed cultures (Figure 26-A).

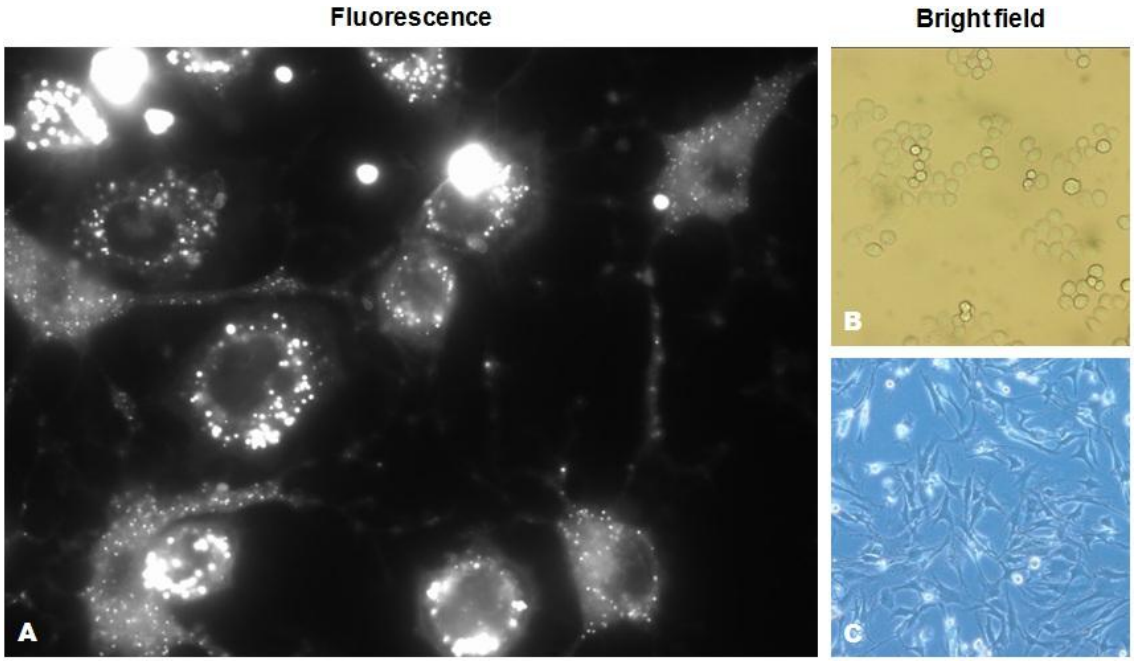

Figure 26 – Increased targeting of anti-MUC1 1-methylpyrene-loaded micelles to MDA-MB-468 breast cancer cells. MDA-MB-468 (B) and S17 (C) cells were seeded with the proportion of 1:5 and incubated for 1 hour with anti-MUC1 bioconjugated micelles. After incubation and cell fixation, it was evident the increased uptake of anti-MUC1 micelles by the human MUC1-expressing MDA-MB-468 cells (A).

5. Gd(III) COMPLEXES AND FLUOROPHORE CONCENTRATIONS IN MICELLE SOLUTIONS

Although the initial amount of Gd(III) complexes or 1-methylpyrene used to synthesize the loaded micelles was known, a fraction of the initial quantity was likely not encapsulated within micelles and was eliminated from the final nanoparticle solution during dialysis. Thus, to estimate the effective concentration of Gd(III) complexes or 1-methylpyrene encapsulated within nanoparticles during self-assembly, we performed a calibration curve plotting the concentration of Gd(III) complexes or 1-methylpyrene and its absorbance spectrum (Figure 27 and 28, respectively).

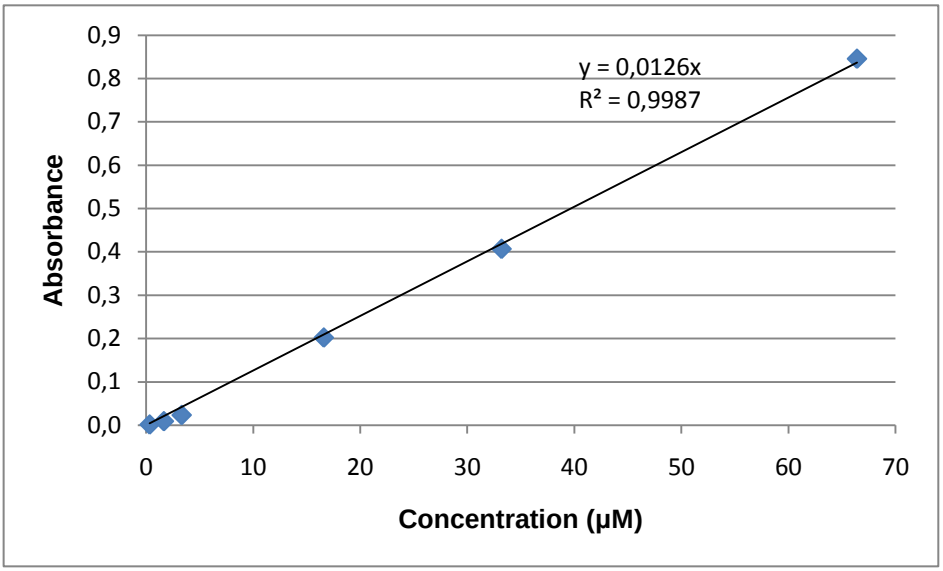

Figure 27 – Calibration curve for Gd(III) complexes. By measuring absorbances of six Gd(III) complex solutions of different concentrations a calibration curve was obtained to estimate the concentration of Gd(III) complex in unknown samples.

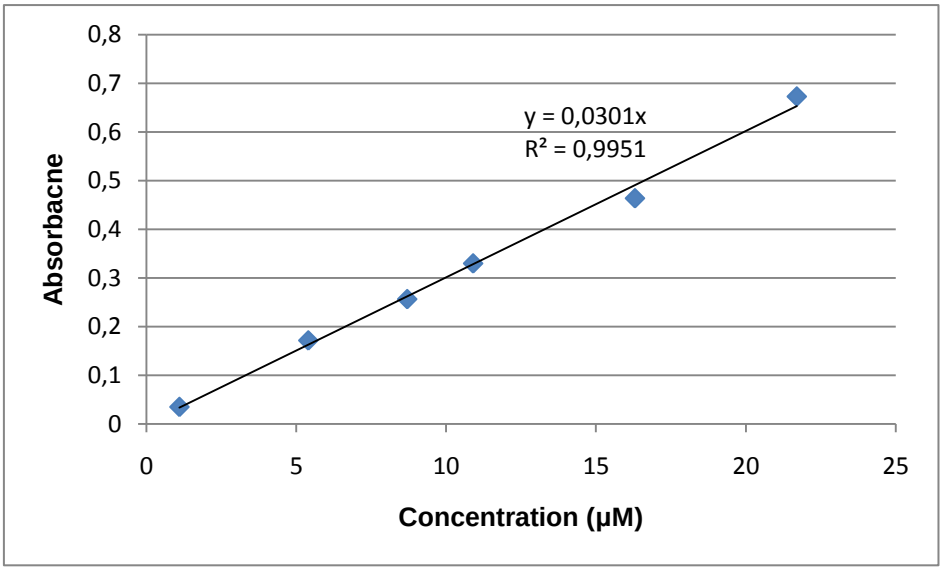

Figure 28 – Calibration curve for 1-methylpyrene. By measuring absorbances of six 1-methylpyrene solutions of different concentrations, a calibration curve was obtained to estimate the concentration of 1-methylpyrene in unknown samples.

Using the obtained calibration curve for 1-methylpyrene, we measured the concentration of bioconjugated and non-targeted 1-methilpyrene-loaded micelle samples (Table 2). Since to obtain the concentration data presented on Table 2 the micelle samples were diluted 100 times, the real concentration of 1-methylpyrene present on the original solutions of non-targeted 1-methylpyrene loaded micelles was 1.61×10^3 µM, while the concentration of the original solution of bioconjugated micelles was 8.3×10^2 µM. Therefore, the solutions containing bioconjugated micelles that we used for cell targeting were approximately half the concentration of nontargeted micelles.

Table 2 – Absorbance measurements of 1-methylpyrene-loaded micelle solutions.

Sample	Absorbance	Concentration (µM)
Fluorophore-loaded micelles	0.4847	16.1
Bioconjugated fluorophore-loaded micelles	0.2509	8.3

CHAPTER IV: DISCUSSION

One of the greatest challenges in medical imaging is to detect cancer early. This has been the major factor in improving successful therapy, in reducing mortality, and reducing cancer management costs (Fass, 2008). Smart CAs seems to offer a significant improvement for disease detection because these agents change their conformational state in the presence of specific stimuli. The change is detected as an alteration in the MR image signal. The smart CAs might detect a change in pH, which is a common feature of cancerous tissues and occurs early during tumor development (Hartman et al., 2008).

Contributing for early cancer detection, we have developed a new MRI contrast agent composed of pH-sensitive micelles with encapsulated hydrophobic Gd(III) complexes. These micelles were bioconjugated with an antibody to target the MUC1 protein, which is a valuable early cancer biomarker (Cheng et al., 2009).

During this research project we have demonstrated that: *i*) encapsulation of Gd(III) complexes within micelles abrogated their cytotoxicity; *ii*) micelles loaded with Gd(III) complexes released their content at low pH; and *iii*) micelles conjugated with an antibody against the MUC1 cell surface protein displayed increased affinity for cultured human breast cancer cells expressing high levels of this protein, than for other cells.

1. NANOPARTICLE SIZE AND pH STABILITY

Important features in nanoparticles production are the achievement of a certain particle size with a narrow size distribution and a good stability (Galindo-Rodriguez, Allémann, Fessi, & Doelker, 2004). The new micelles possessed these characteristics.

The small micelle size is important, because extravasation of nanoparticles from blood vessels into tissues and endocytosis by cells are dependent on nanoparticle size. Yuan and colleagues suggested that the limit size for liposomes extravasation from blood vessels into tumors was approximately 400 nm (Yuan et al., 1995), whereas other authors demonstrated that sizes inferior to 200 nm are more efficient (Hobbs et al., 1998). Others reviewed that nanoparticles with sizes smaller than 100 nm should be preferably used to tumor targeting as they are small enough to escape clearance by macrophages from liver and spleen, and thus are able to circulate long enough to extravasate through fenestrated tumor vasculature (Couvreur & Vauthier, 2006). Regarding the cellular uptake of ligand-coated nanoparticles it has been demonstrated that nanoparticle diameters below 50 nm presented a greater uptake by cells compared

with particles with larger diameters (Gao, Shi, & Freund, 2005). Also Zhang and coworkers theoretically demonstrated that the uptake rate reaches a maximum approximately at diameters of 50 nm, which was in agreement with others experimental studies (Zhang, Li, Lykotrafitis, Bao, & Suresh, 2009).

Since the size of the newly created micelles was estimated to be of approximately 24 nm (see Introduction; Figure 3), these nanoparticles are therefore suitable to be maintained in the blood flow until crossing the leaky cancer vessels, accumulate at interstitial spaces, remain here long enough to allow disassembly and release of the contrast agent in the presence of low pH. It should thus be possible to obtain an image signal from this specific pathological area.

Cancer tissues are characterized by an acidic microenvironment, with extracellular pH values ranging from 6.2-6.9 (Gillies et al., 2002). The performed tests undoubtedly demonstrated that micelles disassembled at pH values near 4-5 and were stable at pH=7. The micelles also released the CA into the hind leg muscles without the presence of the acid solution. However the injected mouse was quite agitated before being anesthetized. Exercising to exhaustion decreases skeletal muscle pH to around 6.6 (Harmer et al., 2000), thus maybe this pH decrease could caused micelles disassembled. Additional tests to better characterize micelle stability at pH range between 4 to 7 should be performed in order to accurately establish the threshold pH for micelle disassembly.

2. Gd(III) COMPLEX AND MICELLE CYTOTOXICITY

The IC_{50} of the newly synthesized hydrophobic Gd(III) complexes ranged from 10.2-12.8 μM depending of the used cancer cell line. At 50 μM Gd(III) complexes killed most cells after 3 days in culture. However, when the Gd(III) complexes were entrapped inside micelles, the toxicity was almost absent, even after 3 days of *in vitro* incubation. This means that the micelles prevented cells from Gd(III) complex toxicity.

The protection from content toxicity provided by these micelles is important for their administration as nanocarriers in *in vivo* studies. This allows reduced toxicity to non-disease tissues, at least until micelles reach the appropriate environment and disassemble. Nevertheless, further tests should be performed to compare the toxicity of our hydrophobic Gd(III) complexes with that of other Gd-based CAs commercially available, and to verify if our smart CA has clinically acceptable toxicity levels,

especially because after release from micelles the CA will be potentially toxic for healthy tissues during body elimination. When comparing the IC_{50} of 10.2-12.8 μM of our Gd(III) complexes with the the IC_{50} greater than 100 μM achieved by HPMA-(DOTA-Gd] complexes and the IC_{50} of approximately 1000 μM achieved by a commercially available CA (Zarabi, Nan, Zhuo, Gullapalli, & Ghandehari, 2008), we conclude that our contrast agent has increased cytotoxicity.

To avoid excessive Gd(III) release and harmful accumulation in body tissues, the Gd(III) chelating system should be stable (Bushong, 2003, pp.365-373). Researchers that attached Gd(III)-based CAs to the surface of nanoparticles had also to increase the stability of the chelating system of their CAs, as compared to commercially available LMWCAs (Winter et al., 2008). More stable Gd(III) chelation was necessary because having targeted nanoparticles higher circulating times than LMWCAs, the CAs attached to the surface of nanoparticles have an increased probability of encountering competing species (metal centers) that cause the exchange of ligands, a reaction designated as transmetallation (Winter et al., 2008). In our case, a stability of the chelating system equivalent to that of commercially available LMWCAs appears sufficient, because the CA will be encapsulated inside micelles, so preventing access to competing species and therefore avoiding transmetallation, at least until micelles disassembled in the target tissue. Only when micelle disassembly occurs in the body and the Gd(III) complex is eliminated, the CA is expected to be susceptible to transmetallation.

As our toxicity study showed, micelles seemed to be stable at least for 3 days *in vitro*. During the incubation time the micelles were in close contact with cells and culture media. Thus we expect that in *in vivo* studies the nanoparticles that do not reach their target will be stable long enough to be eliminated without leakage of CA. However, before proceeding to *in vivo* tests it is important to investigate the micelle stability in the presence of plasma proteins and body temperature.

We have observed slightly higher, but statistically significant cytotoxicity caused by micelles dialyzed for 1 day, as compared to micelles dialyzed for 4 days. This finding indicates that not all of the initial amount of Gd(III) complexes were encapsulated and more than 1 day of dialysis is required to wash off any unencapsulated Gd(III) complexes.

Two different cell lines were used for the cytotoxicity experiments, and we verified that the MCF-7 breast adenocarcinoma cell line showed always a higher percentage of viable cells for each used Gd(III) complex concentration than Jurkat

leukemic cells. This differential susceptibility could be due to different genetic origins and characteristics of the cell lines. Supporting this idea, an experimental study to assess the cell-type-dependent sensitivity to UV-induced apoptosis showed that after exposure to UV irradiation Jurkat cells exhibited faster apoptotic death than MCF-7 cells (Suzuki, Akimoto, Sasai, & Yajima, 2003).

3. MUC1 GENE AND PROTEIN DIFFERENTIAL EXPRESSION BETWEEN CELL LINES

MUC1 was chosen as a target for this new MRI CA due to its great potential for early detection and staging of tumors, as well as for the assessment of tumor responses to therapy and detection of disease recurrence (Kufe, 2009). In addition, the tumoral expression of this protein can be useful for breast cancer differential diagnosis and prognosis (Medarova, 2009).

This potential is based upon the observation that MUC1 is up-regulated in almost all human epithelial cell adenocarcinomas, in few non-epithelial cancer cell lines and in some hematological malignancies (Kufe, 2009; Moore et al., 2004), so MUC1 overexpression is a very frequent phenomenon in cancer. MUC1 is also underglycosylated and ubiquitously expressed throughout the cancer cell surface. The diminished MUC1 glycosylation exposes new epitopes that allow the development of targeting ligands that selectively recognize cancer cells (Ferreira et al., 2008). The MUC1 extracellular domain protrudes 200-500 nm above the plasma membrane, making it an easy target for imaging targeted nanoparticles (Gendler, 2001). Underglycosylated MUC1 was shown to be overexpressed throughout the tumor life and has been detected on primary tumors, as well as on metastases (Medarova, 2009), so it can be a valuable marker for the detection of not only early cancers but also recurring or metastatic cancer.

Concerning breast cancer in particular, MUC1 is expressed in more than 90% of cases (Mahanta et al.; 2008). Immunohistochemical studies revealed membranar expression of MUC1 in benign breast lesions and in DCIS and only poorly differentiated lesions of DCIS showed underglycosylated MUC1. It was reported that membranar expression of MUC1 decreases cell–cell and cell–extracellular matrix interactions (Zhao et al., 2009). Consequently this alteration may facilitate the evolution of pre-invasive lesions such as DCIS to invasive cancers and ultimately to metastases.

Furthermore, MUC1 is often underglycosylated in invasive carcinomas, so detection of underglycosylated MUC1 in pre-invasive breast lesions such as DCIS may be predictive of a higher risk of evolution to invasive carcinoma (Mommers et al., 1999).

MUC1 expression could be correlated with stage progression because in different cancer progression stages, MUC1 displayed distinct molecular features such as increased expression, deglycosylation and alterations in its cell localization. For example benign breast lesions demonstrated slightly elevated levels of MUC1, as compared to healthy tissues, but higher levels were detected in more advanced stages of breast cancer, and in the underglycosylated form (Medarova, 2009).

Since MUC1 protein is expressed in the great majority of breast cancers, it is more advantageous for targeting approaches than other proteins such as HER2, which is overexpressed in only 20–30% of breast cancers (Sood, 2009).

To perform targeting studies it was important to detect and compare the expression levels of MUC1 gene and protein in different cancer cell lines. In agreement with the notion that MUC1 is overexpressed in almost all human adenocarcinomas as well as in some hematological malignancies, we found MUC1 gene and protein expression in all cancer cell lines tested with the exception of the HEK293T cell line, which showed only residual gene expression. This cell line has been used as negative control for MUC1 protein detection (Mahanta et al.; 2008), so the residual gene expression obtained was expected. In another experimental work, authors performed immunocytochemistry to assess the specific binding of newly created recombinant antibody fragments against MUC1 expressed in breast, colon and ovarian cancer cell lines (Rahbarizadeh et al.; 2004). These antibody fragments revealed a differential expression of MUC1 between cell lines, and found also higher expression of this protein in MDA-MB-468 cells than in another breast cancer cell line, the MCF-7 cells (Rahbarizadeh et al.; 2004). Other researchers also reported quite high levels of MUC1 protein expression in the MDA-MB-468 cell line (Schroeder, Adriance, Thompson, Camenisch, & Gendler, 2003). These diferences in MUC1 expression levels between MDA-MB-468 and MCF-7 cells were confirmed by our both experiments detecting MUC1 gene and protein. Western blotting was only performed for MCF-7 cells, so additional experiments have to be performed to detect MUC1 on MDA-MB-468 cell line and compare its levels with those from MCF-7. Nevertheless, protein surface expression, which is more interesting for our work than total cellular expression, was demonstrated for both breast cancer cell lines by flow cytometry.

To target MUC1 we used the mouse monoclonal antibody C595, which reacts with the tetrameric motif, RPAP, present on the VNTR region of the MUC1 protein extracellular domain. This antibody proved to be an efficient and specific targeting vector in *in vitro* studies, in preclinical and clinical trials of radioimmunoscintigraphy and radioimmunotherapy (Song et al., 2008; Simms, Price, Scholfield, & Bishop, 2001; Murray et al., 2001). This antibody was first developed to detect mucins in the serum of cancer patients because it was found in clinical studies that the levels of epithelial mucins in the blood were particularly elevated in patients with metastatic disease from breast cancer (Price, 1988). Another study verified that normal urine was an abundant source of epithelial mucins, so the MAb C595 (IgG3) was raised against the protein core of human urinary epithelial mucin (Price, et al., 1987). The authors of these work concluded that the C595 epitope was present in normal and malignant tissues (Price, et al., 1990), and was therefore not ideal to detect differentially cancer from normal cells.

Consequently this antibody is not specific for underglycosylated MUC1, which is the most frequent form of MUC1 on cancer cell surfaces. Regarding our flow cytometry determination of MUC1 protein expression at the cell surface, we found that MUC1 was expressed in MCF-7 and MDA-MB-468 cells, but however at levels lower than those observed in other reports using antibodies that may have a greater specificity to underglycosylated MUC1 (Akewanlop et al., 2001; Walsh, Luckie, Cummings, Antalis, & McGuckin, 2000). This suggests that the C595 antibody we used detects weakly MUC1 expressed in cancer cells, which is underglycosylated, and rather detects fully glycosylated MUC1 expressed in normal cells. So, if we use the C595 antibody for *in vivo* targeting studies of MUC1-positive breast cancers, perhaps the detection efficiency will not be optimal. The MUC1 N-terminal domain is normaly shedded from the cancer cell surface and consequenlty high amounts of this subunit are found in the blood. Therefore, the C595-conjugated micelles would first interact with shedded MUC1 in the circulation and would not interact efficiently with underglycosylated MUC1 on the surface of cancer cells (Kufe, 2009). In addition, the targeted nanoparticles bound to shedded MUC1 would be quickly cleared from the circulation (Kufe, 2009).

Most commercially available antibodies react against the core protein epitopes that include the sequence PDTRPAP (Rahbarizadeh, et al., 2004). The C595 MAb that we used recognizes the sequence RPAP, which is adjacent to the threonine that undergoes glycosylation. In cancer cells the threonine residue is underglycosylated and

is exposed. Since in underglycosylated MUC1 the APDTRP sequence is exposed and is immunogenic, several monoclonal antibodies against this sequence have been developed. For example the SM3 monoclonal antibody, which recognizes the PDTRP sequence (Burchell, Taylor-Papadimitriou, Boshell, Gendler, & Duhig, 1989), has been found to react specifically against breast carcinomas but not benign lesions (Burchell, et al., 1987).

Because underglycosylated MUC1 is very frequent and specific for breast cancer; antibodies specific for underglycosylated MUC1 should be used in future experiments. Monoclonal antibodies have several advantages for cancer cell targeting. They contain two binding sites, which provide a higher binding avidity for the target antigen. The antibodies can also induce signaling cascades that kill cancer cells (Carter, 2001).

4. BIOCONJUGATION OF NANOPARTICLES POTENTIATES TARGETING TO MUC1-EXPRESSING CELLS

Our experiments performed to assess the specific targeting of bioconjugated micelles showed that their uptake by cells expressing the MUC1 was higher than uptake of non-targeted micelles.

The increased cell internalization of targeted nanoparticles has been verified in other studies using different receptors for targeting, and was shown to be due to receptor-mediated endocytosis (Lee et al., 2003; Gao et al., 2005; T. Chen et al., 2009). Some degree of nonspecific uptake was detected, which could be due to pinocytosis after the adsorption of the nanoparticles to the cellular membrane. Non-specific uptake *in vitro* can be influenced by surface charge and concentration of the nanoparticles as well as by the incubation time with cells (Panyam & Labhasetwar, 2004). However further tests will have to be conducted to prove that the brighter fluorescence spots observed in cells targeted with micelles are endocytic vesicles (endosomes and/or lysosomes).

The results obtained by fluorescence microscopy and flow cytometry indicate that micelle bioconjugation with a MUC1 antibody increased targeting to MUC1-expressing cells. However, several experimental aspects need to be improved to quantify more accurately the specificity of bioconjugated micelles and to obtain more statistical support. An issued to be improved for all procedures is to obtain a more

accurate estimation of the concentration of 1-methylpyrene as well as the micelle aggregation number for targeted and non-targeted micelles. By doing this, we will use equivalent concentration of both types of micelles in experiments. The experiments presented in this thesis were performed with the same amount (μL) of each micelle colloid prepared in parallel, which did not mean exactly the same concentration of micelles. After micelle synthesis it appeared that each sample had different concentrations of nanoparticles due to their different turbidity. The non-targeted micelle dispersion was visibly more turbid than that from targeted micelles, so we assume that the former were more concentrated than the latter. Turbidity appears because the nanoparticles scatter light (Bhalerao, Sinha, Srivastava, & Srivastava, 2009). However, this assumption requires confirmation.

To test the specificity of C595-conjugated 1-methylpyrene-loaded micelles we incubated these with MDA-MB-468 and S17 cells, and found that MDA-MB-468 cells incorporated more fluorescence than the latter. This result was based on the observation that the MDA-MB-468 breast cancer cells have different morphology than S17 cells. Since morphological observation is not very accurate, we could not quantify the percentage of targeted cells. To be able to do this, we plan to stain MDA-MB-468 cells with a red fluorescence before mixing these cells with unstained S17 cells. After incubation with C595-conjugated 1-methylpyrene-loaded micelles, percentage of red fluorescent cells that also present 1-methylpyrene fluorescence will be estimated.

5. Gd(III) COMPLEXES AND FLUOROPHORE CONCENTRATIONS IN MICELLE SOLUTIONS

To estimate the concentration of micelles in solutions, we created calibration curves for Gd complexes and 1-methylpyrene. By doing this, we could estimate that non-targeted 1-methylpyrene-loaded micelle solutions were more concentrated than targeted micelles. This result is therefore in agreement with the observation that non-targeted micelle solutions were more turbid than targeted micelles. In addition, using these calibrations curves, it will be possible to estimate the concentration of 1-methylpyrene and Gd(III) complexes loaded in micelles, before undertaking further *in vitro* and *in vivo* tests. The accuracy of these measurements will not be however fully accurate due to the fact that not all non-encapsulated compounds will be washed off by dialysis. Concerning the Gd (III) complexes, it will be necessary to verify the amount which is

encapsulated and to measure the T_1 relaxivity of these newly synthesized hydrophobic Gd(III) complexes before proceeding to *in vivo* studies. It is important to use equivalent concentrations to those recommended clinically in order to compare the performance of this new contrast agent with others in research or commercially available.

In conclusion, this work demonstrated that this new designed micelles successfully encapsulate hydrophobic Gd(III) complexes or fluorescent dyes and preventing cytotoxicity caused by Gd(III) complexes. These nanoparticles proved to be able to release their content exclusively at low pH environments, causing a signal enhancement in MR T_1-weight images, and were effectively bioconjugated with the C595 MAb.

Conjugation with this antibody potentiated the specific attachment of micelles to the target cells *in vitro*. Therefore our results support the notion that these self-assembled nanoparticles are suitable to be used as MRI contrast agents, by passively and actively targeting cancerous cells. We expect these nanoparticles to increase MRI sensitivity in early breast cancer detection and to improve tumor staging as well as assessment of tumor responses to therapy.

CHATER V: FUTURE PERSPECTIVES

This work describes preliminary data indicating the suitability of this new contrast agent for MRI detection of breast cancer. To reach the final goal, which is to develop a product that can be clinically useful, there are still several experiments to perform.

1) The nanoparticles here described detect glycosylated MUC1 protein. Since underglycosylated MUC1 is characteristic of cancers, we will verify whether an antibody specific for underglycosylated MUC1 (SM3 monoclonal antibody) detects MDA-MB-468 and MCF-7 breast cancer cells with higher affinity than the C595 antibody.

2) For further *in vitro* and *in vivo* experiments, it will be important to have more information about the size, stability and concentration of synthesized nanoparticles. To this end, we will carry out additional characterization tests concerning size; micelle aggregation number, payload and encapsulation efficiency of Gd(III) complexes or 1-methylpyrene fluorophore. To estimate the stability of nanoparticles in the blood circulation and in body tissues, we will verify their stability in the presence of physico-chemical conditions mimicking blood circulation, i.e. pH, temperature and serum proteins.

3) To test the efficiency of the SM3 antibody for targeting micelles to breast cancer cells expressing underglycosylated MUC1, micelles will be conjugated with this antibody. Then, SM3-conjugated and non-conjugated micelle concentration will be estimated and then equal concentrations will be incubated with breast cancer cell lines to quantify their targeting ability by fluorescence microscopy and flow cytometry. For fluorescence microscopy experiments, MUC1-expressing cancer cells stained with a red fluorescence dye will be used to accurately distinguish them from MUC1-negative cells and so determine which cells incorporate 1-methylpyrene. In addition, we will use fluorescent dyes that specifically stain different endocytic vesicles to understand better the nanoparticle uptake mechanism.

4) To determine the targeting ability of antibody conjugated and unconjugated nanoparticles, we will implement an MDA-MB-468 breast cancer xenograft mouse models. Tumors will develop in these mice and after nanoparticle injection in their circulation, MRI is going to be performed to detect cancer cells.

5) To know the *in vivo* behavior of our newly developed targeted and non-targeted nanoparticles, the pharmacokinetics, release mechanism and the active *in vivo* targeting of MUC1-expressing mouse tumors will be determined using 1.5T MRI.

6) To verify whether this contrast agent can be used universally for cancer detection, we will conjugate nanoparticles with an antibody recognizing another tumor marker, for example the follicle-stimulating hormone receptor (FSHR) protein, which is expressed almost exclusively in tumors.

REFERENCES

Aime, S., Botta, M., Crich, S., Giovenzana, G., Palmisanod, G., & Sistie, M. (1999). A macromolecular Gd(III) complex as pH-responsive relaxometric probe for MRI applications. *Chemical Communications , 9*: 1577–1578.

Aime, S., Cabella, C., Colombatto, S., Crich, S., Gianolio, E., & Maggioni, F. (2002). Insights into the Use of Paramagnetic Gd(III) Complexes in MR-Molecular Imaging Investigations. *Journal of magnetic resonance imaging , 16*: 394–406.

Aime, S., Digilio, G., Fasano, M., Paoletti, S., Arnelli, A., & Ascenzi, P. (1999). Metal Complexes as Allosteric Effectors of Human Hemoglobin: An NMR Study of the Interaction of the Gadolinium(III) Bis(m - boroxyphenylamide) diethylenetriaminepenta acetic Acid Complex with Human Oxygenated and Deoxygenated Hemoglobin. *Biophysical Journal , 76*: 2735–2743.

Akewanlop, C., Watanabe, M., Singh, B., Walker, M., Kufe, D., & Hayes, D. (2001). Phagocytosis of Breast Cancer Cells Mediated by Anti-MUC-1 Monoclonal Antibody, DF3, and its Bispecific Antibody1. *Cancer Research , 61*: 4061–4065.

Allen, T. (2002). Ligand targeted therapeutics in anticancer Therapy. *Nature Reviews - Cancer , 2*: 750-763.

Bafna, S., Kaur, S., & Batra, S. (2010). Membrane-bound mucins: the mechanistic basis for alterations in the growth and survival of cancer cells. *Oncogene , 29*: 2893–2904.

Barros, A., & Barros, M. (2009). Formação e Desenvolvimento do carcinoma de Mama. In V. Aguilar, S. Bauab, & N. Maranhão, *Mama - Diagnóstico por imagem* (pp. 29-39). Rio de Janeiro: Revinter.

Bechara, G., Leygue, N., Galaup, C., Mestre, B., & Picard, C. (2009). An efficient route to pyridine and 2,20-bipyridine macrocycles incorporating a triethylenetetraminetetra acetic acid core as ligand for lanthanide ions. *Tetrahedron Letters , 50*: 6522–6525.

Berge, R., Snijdewint, F., von Mensdorff-Pouilly, S., Poort-Keesom, R., Oudejans, J., Meijer, J., et al. (2001). MUC1 (EMA) is preferentially expressed by ALK positive anaplastic large cell lymphoma, in the normally glycosylated or only partly hypoglycosylated form. *Journal of Clinical Pathology , 54*: 933–939.

Bernard-Marty, C., Cardoso, F., & Piccart, M. (2004). Facts and Controversies in Systemic Treatment of Metastatic Breast Cancer. *The Oncologist , 9*: 617-632.

Bertini, I., Bianchini, F., Calorini, L., Colagrande, S., Fragai, M., Franchi, A., et al. (2004). Persistent Contrast Enhancement by Sterically Stabilized Paramagnetic Liposomes in Murine Melanoma. *Magnetic Resonance in Medicine , 52*: 669-672.

Bhalerao, G., Sinha, A., Srivastava, H., & Srivastava, A. (2009). Synthesis and studies of growth kinetics of monodispersed iron oxide nanoparticles using ferrocene as novel precursor. *Applied Physics A , 95*: 373–380.

Bhujwalla, Z., Artemov, D., Natarajan, K., Ackerstaff, E., & Solaiyappan, M. (2001). Vascular differences detected by MRI for metastatic versus nonmetastatic breast and prostate cancer xenografts. *Neoplasia , 3*: 143–153.

Bon, G., von Mensdorff-Pouilly, S., Kenemans, P., van Kamp, G., Verstraeten, R., Hilgers, J., et al. (1997). Clinical and technical evaluation of ACSYBR serum assay of MUC1 gene-derived glycoprotein in breast cancer, and comparison with CA 15-3 assays. *Clinical Chemistry , 43* (4): 585–593.

Bristow, R., & Hil, R. (2008). Hypoxia, DNA repair and genetic instability. *Nature Reviews - Cancer , 8*: 180 - 192.

Brooks, M. (2009). Breast Cancer Screening and Biomarkers. *Methods of Molecular Biology - Cancer Epidemiology , 472*: 307-321.

Brown, M., & Semelka, R. (2003). *MRI - Basic Principles and Applications* (3 rd ed.). Canada: Wiley - Liss.

Bulte, J., & Modo, M. (2008). Introduction: The emergence of Nanoparticles as Imaging Platform in Biomedicine. In J. Bulte, & M. Modo, *Nanoparticles in Biomedical Imaging - Emerging Technologies and Applications* (pp. 1-5). USA: Springer.

Burchell, J., Gendler, S., Taylor-Papadimitriou, J., Girling, A., Lewis, A., Millis, R., et al. (1987). Development and Characterization of Breast Cancer Reactive Monoclonal Antibodies Directed to the Core Protein of the Human Milk Mucin. *Cancer Research , 47*: 5476-5482.

Burchell, J., Taylor-Papadimitriou, J., Boshell, M., Gendler, S., & Duhig, T. (1989). A short sequence, within the amino acid tandem repeat of a cancer-associated mucin, contains immunodominant epitopes. *International Journal of Cancer , 44* (4): 691- 696.

Burstein, H. (2005). The Distinctive Nature of HER2-Positive Breast Cancers. *New England Journal of Medicine , 353* (16): 1652-1654.

Bushong, S. C. (2003). *Magnetic Resonance Imaging - Physical and Biological Principles* (3rd ed). USA: Mosby.

Cardone, R., Casavola, V., & Reshkin, S. (2005). The role of disturbed pH dynamics and the Na+/H+ exchanger in metastasis. *Nature Reviews - Cancer , 5*: 786-794.

Carter, P. (2001). Improving the efficacy of antibody-based cancer therapies. *Nature reviews - Cancer , 1*: 118-129.

Carvalho, F. M. (2009). Carcinoma Mamário - Anatomia Patológica. In V. Aguilar, S. Bauab, & N. Maranhão, *Mama - Diagnóstico por Imagem* (pp. 57-81). Brasil: Revinter.

Chen, T., Cheng, T., Chen, C., Hsu, S., Cheng, T., Liu, G., et al. (2009). Targeted Herceptin–dextran iron oxide nanoparticles for noninvasive imaging of HER2/neu receptors using MRI. *Journal of Biological Inorganic Chemistry , 14*: 253–260.

Chen, Z., Yu, D., Wang, S., Zhang, N., Ma, C., & Lu, Z. (2009). Biocompatible Nanocomplexes for Molecular Targeted MRI Contrast Agent. *Nanoscale Research Letters , 4*: 618–626.

Cheng, A., Su, H., Wang, Y., & Yu, H. (2009). Aptamer-Based Detection of Epithelial Tumor Marker Mucin 1 with Quantum Dot-Based Fluorescence Readout. *Analytical Chemistry , 81* (15): 6130–6139.

Chiefari, J., Chong, I., Ercole, F., Krstina, J., Jeffery, J., Le, T., et al. (1998). Living Free-Radical Polymerization by Reversible Addition-Fragmentation Chain Transfer: The RAFT Process. *Macromolecules , 31*: 5559-5562.

Choi, C., Alabi, C., Webster, P., & Davis, M. (2010). Mechanism of active targeting in solid tumors with transferrin-containing gold nanoparticles. *PNAS , 107* (3): 1235–1240.

Choi, Y., & Baker, J. (2007). Nanoparticles in Medical Diagnosis and Therapeutics. In T. Vo-Dinh, *Nanoatechnology in Biology and Medicine: Methods, Devices and Applications* (pp. 1-22). USA: Taylor and Francis Group.

Cooper, S., Visser, S., Hergenrother, R., & Lamba, N. (2004). Polymers. In B. Ratner, A. Hoffman, F. Schoen, & J. Lemons, *Biomaterials Science: An Introduction to materials in Medicine* (pp. 67-79). UK: Elsevier.

Corot, C., Robert, F., Idée, J., & Port, M. (2006). Recent advances in iron oxide nanocrystal technology for medical imaging. *Advanced Drug Delivery Reviews , 58*: 1471–1504.

Couvreur, P., & Vauthier, C. (2006). Nanotechnology: Intelligent Design to Treat Complex Disease. *Pharmaceutical Research , 23*: 1417 - 1450.

Daldrup, H., Shames, D., Wendland, M., Okuhata, Y., Link, T., Rosenau, W., et al. (1998). Correlation of Dynamic Contrast Enhanced MR Imaging with HistologicTumor Grade: Comparisonof Macromolecular and Small-MolecularContrast Media. (A. R. Society, Ed.) *American Journal of Roentgenology , 171*: 941-949.

Dawson, S., Provenzano, E., & Caldas, D. (2009). Triple negative breast cancers: Clinical and prognostic implications. *European Journal of Cancer , 45* (1): 27-40.

Draheim, K., Chen, H., Tao, Q., Moore, N., Roche, M., & Lyle, S. (2010). ARRDC3 suppresses breast cancer progression by negatively regulating integrin b4. *Oncogene* , 1–16.

Elias, A., & Dias, S. (2008). Microenvironment Changes (in pH) Affect VEGF Alternative Splicing. *Cancer Microenvironment , 1*: 131–139.

Engel, J., Eckel, R., Kerr, J., Schmidt, M., Furstenberger, G., Richter, R., et al. (2003). The process of metastasisation for breast cancer. *European Journal of Cancer , 39*: 1794–1806.

Erdogan, S., Medarova, Z., Roby, A., Moore, A., & Torchilin, V. (2008). Enhanced Tumor MR Imaging with Gadolinium-Loaded Polychelating Polymer-Containing Tumor-Targeted Liposomes. *Journal of Magnetic Resonance Imaging , 27*: 574–580.

Fass, L. (2008). Imaging and cancer: A review. *Molecular Oncology , 2*: 115–152.

Ferreira, C., Papamichael, K., Guilbault, G., Schwarzacher, T., Gariepy, J., & Missailidis, S. (2008). DNA aptamers against the MUC1 tumour marker: design of aptamer–antibody sandwich ELISA for the early diagnosis of epithelial tumours. *Analytical and Bioanalytical Chemistry* ,1-12.

Folkman, J. (2007). Angiogenesis: an organizing principle for drug discovery? *Nature Reviews - Drug Discovery , 6*: 273-286.

Freimoser, F., Jakob, C., Aebi, M., & Tuor, U. (1999). The MTT [3-(4,5-Dimethylthiazol-2-yl)-2,5-Diphenyltetrazolium Bromide] Assay Is a Fast and Reliable Method for Colorimetric Determination of Fungal Cell Densities. *Applied and Environmental Microbiology , 65* (8): 3727–3729.

Galindo-Rodriguez, S., Allémann, E., Fessi, H., & Doelker, E. (2004). Physicochemical Parameters Associated with Nanoparticle Formation in the Salting-out, Emulsification-Diffusion, and Nanoprecipitation Methods. *Pharmaceutical Research , 21* (8): 1428-1439.

Gambarota, G., van Laarhovenb, H., Philippens, M., Lok, J., van der Kogel, A., Punt, C., et al. (2006). Assessment of absolute blood volume in carcinoma by USPIO contrast-enhanced MRI. *Magnetic Resonance Imaging , 24*: 279–286.

Gandhi, S., Brown, M., Wong, J., Aguirre, D., & Sirlin, C. (2006). MR Contrast Agents for Liver Imaging: What, When, How. *RadioGraphics , 26*: 1621–1636.

Gao, H., Shi, W., & Freund, L. (2005). Mechanics of receptor-mediated endocytosis. *PNAS , 102* (27): 9469–9474.

Gasco, M., Shami, S., & Crook, T. (2002). The p53 pathway in breast cancer. *Breast Cancer Research , 4* (4): 70-76.

Gatenby, R., & Gillies, R. (2004). Why do cancers have high aeribic glycolysis? *Nature Reviews - Cancer , 4*: 891-899.

Gendler, S. (2001). MUC1, The Renaissance Molecule. *Journal of Mammary Gland Biology and Neoplasia , 6* (3): 339-353.

Gillies, E., & Fréchet, J. (2005). pH-Responsive Copolymer Assemblies for Controlled Release of Doxorubicin. *Bioconjugate Chemistry , 16*: 361-368.

Gillies, R., Raghunand, N., Garcia-Martin, M., & Gatenby, R. (2004). pH imaging: A Review of pH Measurement Methods and applications in cancers. *IEEE Engineering in Medicine and Biology Magazine* , 57-64.

Gillies, R., Raghunand, N., Karczmar, G., & Bhujwalla, Z. (2002). MRI of the Tumor Microenvironment. (Wiley-Liss, Ed.) *Journal of Magnetic Resonance Imaging , 16*: 430–450.

Gillies, R., Schornack, P., Secomb, T., & Raghunand, N. (1999). Causes and Effects of heterogeneous Perfusion in Tumors. *Neoplasia , 1* (3): 197-207.

Glogard, C., Stensrud, G., & Aime, S. (2003). Novel radical-responsive MRI contrast agent based on paramagnetic liposomes. *Magnetic Resonance in Chemistry , 41* (8): 585-588.

Goldenberg, D. (2002). Targeted Therapy of Cancer with Radiolabeled Antibodies. *The Journal of Nuclear Medicine , 43*: 693–713.

Goldenberg, D., Abdel-Nabi, H., Sullivan, C., Serafini, A., Seldin, D., Barron, B., et al. (2000). Carcinoembryonic Antigen Immunoscintigraphy Complements Mammography in the Diagnosis of breast carcinoma. *Cancer , 89* (1): 104-115.

Goshima, S., Kanematsu, M., Kondo, H., Shiratori, Y., Onozuka, M., Moriyama, N., et al. (2009). Optimal Acquisition Delay for Dynamic Contrast-Enhanced MRI of Hypervascular Hepatocellular Carcinoma. *American Journal of Roentgenology , 192*: 686–692.

Hanaoka, K., Kikuchi, K., Urano, Y., Narazaki, M., Yokawa, T., Sakamoto, S., et al. (2002). Design and Synthesis of a Novel Magnetic Resonance Imaging Contrast Agent for Selective Sensing of Zinc Ion. *Chemistry & Biology , 9*: 1027–1032.

Harmer, A., Mckenna, M., Sutton, J., Snow, R., Ruell, P., Booth, J., et al. (2000). Skeletal muscle metabolic and ionic adaptations during intense exercise following sprint training in humans. *Journal of Applied Physiology , 89*: 1793–1803.

Hartman, K., Laus, S., Bolskar, R., Muthupillai, R., Helm, L., Toth, E., et al. (2008). Gadonanotubes as Ultrasensitive pH-Smart Probes for Magnetic Resonance Imaging. *Nano Letters , 8* (2): 415-419.

Hawthorn, L., Luce, L., Stein, L., & Rothschild, J. (2010). Integration of transcript expression, copy number and LOH analysis of infiltrating ductal carcinoma of the breast. *BiomedCentral - Cancer , 10* (460): 1-16.

Heller, J., & Hoffman, A. (2004). Drug Delivery Systems. In B. Ratner, A. Hoffman, F. Schoen, & J. Lemons, *Biomaterials Science: An Introduction to materials in Medicine* (2nd ed., pp. 629-648). UK: Elsevier.

Hobbs, S., Monsky, W., Yuan, F., Roberts, W., Griffith, L., Torchilin, V., et al. (1998). Regulation of transport pathways in tumor vessels: Role of tumor type and microenvironment. *Proceedings of the National Academy of Sciences of the United States of America , 95*: 4607–4612.

Hoffman, A. (2004). Applications of "Smart Polymers" as Biomaterials. In B. Ratner, A. Hoffman, F. Schoen, & J. Lemons, *Biomaterials Science: An Introduction to materials in Medicine* (2nd ed., pp. 107-114). UK: Elsevier.

Hong, G., Yuan, R., Liang, B., Shen, J., Yang, W., & Shuai, X. (2008). Folate-functionalized polymeric micelle as hepatic carcinoma-targeted, MRI-ultrasensitive delivery system of antitumor drugs. *Biomed Microdevices , 10*: 693–700.

Hrubý, M., Konák, C., & Ulbrich, K. (2005). Polymeric micellar pH-sensitive drug delivery system for doxorubicin. *Journal of Controlled Release , 103*: 137–148.

Huang, L., Chen, D., Liu, D., Yin, L., Kharbanda, S., & Kufe, D. (2005). MUC1 Oncoprotein Blocks Glycogen Synthase Kinase 3B–Mediated Phosphorylation and Degradation of B-Catenin. *Cancer Research , 65* (22): 10413 - 10422.

Hughes, O., Perkins, A., Frier, M., Wastie, M., Denton, G., Price, M., et al. (2001). Imaging for staging bladder cancer: a clinical study of intravenous 111indium-labelled anti-MUC1 mucin monoclonal antibody C595. *British Journal of Urology International , 87*: 39-46.

Hunter, G., Hamberg, L., Choi, N., Jam, R., McCloud, T., & Fischman, A. (1998). Dynamic Ti-weighted Magnetic Resonance Imaging and Positron Emission Tomography in Patients with Lung Cancer: Correlating Vascular Physiology with Glucose Metabolism. *Clinical Cancer Research , 4*: 949-955.

Hwang, H., Barke, L., Mendelson, E., & Susnik, B. (2008). Atypical lobular hyperplasia and classic lobular carcinoma in situ in core biopsy specimens: routine excision is not necessary. *Modern Pathology , 21*: 1208–1216.

Jones, M., & Leroux, J. (1999). Polymeric micelles - a new generation of colloidal drug carriers. *European Journal of Pharmaceutics and Biopharmaceutics , 48*: 101 - 111.

Kairemo, K., Erba, P., Bergström, K., & Pauwels, E. (2008). Nanoparticles in Cancer. *Current Radiopharmaceuticals , 1*: 30-36.

Ke, S., Wen, X., Gurfinkel, M., Charnsangavej, C., Wallace, S., Sevick-Muraca, E., et al. (2003). Near-Infrared Optical Imaging of Epidermal Growth Factor Receptor in Breast Cancer Xenografts. *Cancer Research , 15*: 7870–7875.

Knudson, A. (2001). Two genetic hits (more or less) to cancer. *Nature reviews - Cancer , 1*: 157-162.

Kozlowska, D., Foran, P., MacMahon, P., Shelly, M., Eustace, S., & O'Kennedy, R. (2009). Molecular and magnetic resonance imaging: The value of immunoliposomes. *Advanced Drug Delivery Reviews , 61*: 1402–1411.

Krishnan, A., Neves, A., de Backer, M., Hu, D., Davletov, B., Kettunen, M., et al. (2008). Detection of Cell Death in Tumors by Using MR Imaging and a Gadolinium-based Targeted Contrast Agent. *Radiology , 246* (3): 854-862.

Kufe, D. (2009). Mucins in cancer: function, prognosis and therapy. *Nature Reviews , 9* : 874-884.

Kufe, D. (2008). Targeting the human MUC1 oncoprotein: a tale of two proteins. *Cancer Biology & Therapy , 7* (1): 81-84.

Kuhl, C. (2007). The Current Status of Breast MR Imaging: Part I. Choice of Technique, Image, Interpretation, Diagnostic Accuracy, and Transfer to Clinical Practice. *Radiology , 244* (2): 356-378.

Kwon, G., & Okano, T. (1999). Soluble Self-Assembled Block Copolymers for Drug Delivery. *Pharmaceutical Research , 16* (5): 597-600.

Lee, C., MacKay, J., Fréchet, J., & Szoka, F. (2005). Designing dendrimers for biological applications. *Nature Biotechnology , 23* (12): 1517 - 1526.

Lee, E., Na, K., & Bae, Y. (2005). Doxorubicin loaded pH-sensitive polymeric micelles for reversal of resistant MCF-7 tumor. *Journal of Controlled Release , 103*: 405–418.

Lee, E., Na, K., & Bae, Y. (2003). Polymeric micelle for tumor pH and folate-mediated targeting. *Journal of Controlled Release , 91*: 103–113.

Levitin, F., Stern, O., Weiss, M., Gil-Henn, C., Ziv, R., Prokocimer, Z., et al. (2005). The MUC1 SEA Module Is a Self-cleaving Domain. *The Journal of Biological Chemistry , 280* (39): 33374–33386.

Li, W., Fraser, S., & Meade, T. (1999). A Calcium-Sensitive Magnetic Resonance Imaging Contrast Agent. *J. Am. Chem. Soc. , 121*: 1413-1414.

Li, X., Du, X., Huo, T., Liu, X., Zhang, S., & Yuan, F. (2009). Specific Targeting of Breast Tumor by Octreotide-Conjugated Ultrasmall Superparamagnetic Iron Oxide Particles Using a Clinical 3.0-Tesla Magnetic Resonance Scanner. *Acta Radiologica , 50* (6): 583 — 594.

Liu, J., Zeng, F., & Allen, C. (2007). In vivo fate of unimers and micelles of a poly(ethylene glycol)-block-poly(caprolactone) copolymer in mice following intravenous administration. *European Journal of Pharmaceutics and Biopharmaceutics , 65*: 309–319.

Liu, Z., Kiessling, F., & Gatjens, J. (2010). Advanced Nanomaterials inMultimodal Imaging: Design, Functionalization, and Biomedical Applications. *Journal of Nanomaterials* , 1-15.

Livak, K., & Schmittgen, T. (2001). Analysis of Relative Gene Expression Data Using Real-Time Quantitative PCR and the $2^{-\Delta\Delta CT}$ Method. *Methods , 25*: 402–408.

Lyons, S. (2005). Advances in imaging mouse tumour models in vivo. *Journal of Pathology , 205*: 194–205.

Macey, D., Grant, E., Kasi, L., Rosenblum, M., Zhang, H., Katz, R., et al. (1997). Effect of Recombinant a-Interferon on Pharmacokinetics,Biodistribution, Toxicity, and Efficacy of 131I-Labeled Monoclonal Antibody CC49 in Breast Cancer: A Phase II Trial. *Clinical Cancer Research , 3*: 1547-1555.

Maeda, H., Sawa, T., & Konno, T. (2001). Mechanism of tumor-targeted delivery of macromolecular drugs, including the EPR effect in solid tumor and clinical overview of the prototype polymeric drug SMANCS. *Journal of Controlled Release , 74*: 47–61.

Maeda, H., Wu, J., Sawa, T., Matsumura, Y., & Hori, K. (2000). Tumor vascular permeability and the EPR effect in macromolecular therapeutics: a review. *Journal of Controlled Release , 65*: 271–284.

Mahanta, S., Fessler, S., Park, J., & Bamdad, C. (2008). A Minimal Fragment of MUC1 Mediates Growth of Cancer Cells. *PLoSONE , 3* (4): 1-12.

Mankoff, D. (2007). A Definition of Molecular Imaging. *The Journal of Nuclear Medicine , 48* (6): 18-21.

Masri, A., & Gendler, S. (2005). Muc1 affects c-Src signaling in PyV MT-induced mammary tumorigenesis. *Oncogene , 24*: 5799–5808.

Massoud, T., & Gambhir, S. (2003). Molecular imaging in living subjects: seeing fundamental biological processes in a new light. *Genes & Development , 17*: 545–580.

Matsumura, Y., & Maeda, H. (1986). A New Concept for Macromolecular Therapeutics in Cancer Chemotherapy:Mechanism of Tumoritropic Accumulation of Proteins and the Antitumor Agent Smancs1. *Cancer Research , 46*: 6387-6392.

Mattrey, R., & Aguirre, D. (2003). Advances in Contrast Media Research. *Academic Radiology , 10* (10): 1450–1460.

McAuley, J., Linden, S., Png, C., King, R., Pennington, H., Gendler, S., et al. (2007). MUC1 cell surface mucin is a critical element of the mucosal barrier to infection. *The Journal of Clinical Investigation , 117*: 2313–2324.

McDonald, D., & Choyke, P. (2003). Imaging of angiogenesis: from microscope to clinic. *Nature Medicine , 9* (6): 713-725.

McPherson, K., Steel, C., & Dixon, J. (2000). Breast cancer - epidemiology, risk factors, and genetics. *British Medical Journal , 321*: 624-628.

McRobbie, D., Moore, E., Graves, M., & Prince, M. (2006). *MRI from Picture to Proton.* USA: Cambridge University Press.

Medarova, Z. (2009). Noninvasive imaging of breast cancer. *Biotechnology & Biotechnological Equipment , 23* (4): 1453-1461.

Medarova, Z., Pham, W., Kim, Y., Dai, G., & Moore, A. (2006). In vivo imaging of tumor response to therapy using a dual-modality imaging strategy. *International Journal of Cancer , 118*: 2796–2802.

Meijnen, P., Peterse, J., Antonini, N., Rutgers, E., & van de Vijver, M. (2008). Immunohistochemical categorisation of ductal carcinoma in situ of the breast. *British Journal of Cancer , 98*: 137 – 142.

Moats, R., Fraser, S., & Meade, T. (1997). A "Smart" Magnetic Resonance Imaging Agent That Reports on Specific Enzymatic Activity. *Angewandte Chemie - International Edition , 36* (7): 726–728.

Mommers, E., Leonhart, A., Von Mensdorff-Pouilly, S., Schol, D., Hilgers, J., Meijer, C., et al. (1999). Aberrant expression of MUC1 mucin in ductal hyperplasia and ductal carcinoma in situ of the breast. *International Journal of Cancer , 84*: 466–469.

Moore, A., Medarova, Z., Potthast, A., & Dai, G. (2004). In Vivo Targeting of Underglycosylated MUC-1 Tumor Antigen Using a Multimodal Imaging Probe. *Cancer Research , 64*: 1821–1827.

Morris, S., & Carey, L. (2007). Molecular profiling in breast cancer. *Reviews in endocrine and metabolic disorders , 8*: 185–198.

Mouffouk, F., Chishti, Y., Jin, Q., Rosa, M., Rivera, M., Dasa, S., et al. (2008). Polymeric micelle-based bioassay with femtomolar sensitivity. *Analytical Biochemistry , 372*: 140–147.

Mulder, W., Strijkers, G., van Tilborg, G., Griffioen, A., & Nicolay, K. (2006). Lipid-based nanoparticles for contrast-enhanced MRI and molecular imaging. *NMR in Biomedicine , 19*: 142–164.

Murakami, K., Nawano, S., Moriyama, N., & Onuma, Y. (1998). Usefulness of Magnetic Resonance Imaging with Dynamic Contrast Enhancement and Fat Suppression in Detecting a Pancreatic Tumor. *Japanese Journal of Clinical Oncology , 28* (2): 107-111.

Murray, A., Simms, M., Scholfield, D., Vincent, R., Denton, G., Bishop, M., et al. (2001). Production and Characterization of 188Re-C595 Antibody for Radioimmunotherapy of Transitional Cell Bladder Cancer. *The Journal of Nuclear Medicine , 42* (5): 726-732.

Nakamura, E., Makino, K., Okano, T., Yamamoto, T., & Yokoyama, M. (2006). A polymeric micelle MRI contrast agent with changeable relaxivity. *Journal of Controlled Release , 114*: 325–333.

Natarajan, A., Xiong, C., Gruettner, C., DeNardo, G., & DeNardo, S. (2008). Development of Multivalent Radioimmunonanoparticles for Cancer Imaging and Therapy. *Cancer Biotherapy and radiopharmaceuticals , 23* (1): 82 - 91.

Nitz, W., & Reimer, P. (1999). Contrast mechanisms in MR imaging. *European Radiology , 9*: 1032-1046.

Ocak, I., Bernardo, M., Metzger, G., Barrett, T., Pinto, P., Albert, P., et al. (2007). Dynamic Contrast-Enhanced MRIof Prostate Cancer at 3 T: A Study of Pharmacokinetic Parameters. *American Journal of Roentgenology , 189*: 192–201.

Orive, G., Reshkin, S., Harguindey, S., & Pedraz, J. (2003). Hydrogen ion dynamics and the Na+/H+ exchanger in cancer angiogenesis and antiangiogenesis. *British Journal of Cancer , 89*: 1395 – 1399.

Osborne, C., & Schiff, R. (2005). Estrogen-Receptor Biology: Continuing Progress and Therapeutic Implications. *Journal of Clinical Oncology , 23*: 1616-1622.

Padhani, A. (2002). Dynamic Contrast-Enhanced MRI in Clinical Oncology: Current Status and Future Directions. *Journal of Magnetic Resonance Imaging , 16*: 407–422.

Palivan, C., Vebert, C., Axthelm, F., & Meier, W. (2006). Responsive Self-assembled Nanostructures. In T. Vo-Dinh, *Nanotechnology in Biology and Medicine - Methods, Devices, and Applications* (Vol. 32, pp. 1-26). USA: Taylor and Francis Group.

Panyam, J., & Labhasetwar, V. (2004). Targeting Intracellular Targets. *Current Drug Delivery , 1*: 235-247.

Park, J., & Lakes, R. (2007). *Biomaterials: An Introduction* (3rd ed). USA: Springer.

Peer, D., Karp, J., Hong, S., Farokhzad, O., Margalit, R., & Langer, R. (2007). Nanocarriers as an emerging platform for cancer therapy. *Nature Nanotechnology , 2*: 751-759.

Penet, M., Glunde, K., Jacobs, M., Pathak, A., & Bhujwalla, Z. (2008). Molecular and Functional MRI of the Tumor. *The Journal of Nuclear Medicine , 49* (5): 687-690.

Perou, C., Sùrlie, T., Eisen, M., van de Rijn, M., Jeffreyk, S., Rees, C., et al. (2000). Molecular portraits of human breast tumours. *Nature , 406*: 747-752.

Pinder, S., & Ellis, I. (2003). Ductal carcinoma in situ (DCIS) and atypical ductal hyperplasia (ADH) — current definitions and classification. *Breast Cancer Research , 5*: 254-257.

Porter, A., & Youtie, J. (2009). Where does nanotechnology belong in the map of science? *Nature Nanotechnology , 4*: 534-536.

Price, M. (1988). High molecular weight epithelial mucins as markers in breast cancer. *European Journal of Cancer and Clinical Oncology , 24* (12):1799-1804.

Price, M., Crocker, G., Edwards, S., Nagra, I., Robins, R., Williams, M., et al. (1987). Identification of a monoclonal antibody-defined breast carcinoma antigen in body fluids. *European Journal of Cancer and Clinical Oncology , 23* (8): 1169-1176.

Price, M., Pugh, J., Hudecz, F., Griffiths, W., Jacobs, E., Symonds, I., et al. (1990). C595 - a monoclonal antibody against the protein core of human urinary epithelial mucin commonly expressed in breast carcinomas. *British Journal of Cancer , 61*: 681-686.

Priest, A., Ittrich, H., Jahntz, C., Kooijman, H., Weber, C., & Adam, G. (2006). Investigation of atherosclerotic plaques with MRI at 3 T using ultrasmall superparamagnetic particles of iron oxide. *Magnetic Resonance Imaging , 24*: 1287–1293.

Que, E., & Chang, C. (2006). A Smart Magnetic Resonance Contrast Agent for Selective Copper Sensing. *Journal of American Chemical Society , 128*: 15942-15943.

Rahbarizadeh, F., Rasaee, M., Moghadam, M., Allameh, A., & Sadroddiny, E. (2004). Production of Novel Recombinant Single-Domain Antibodies against Tandem Repeat Region of MUC1 Mucin. *Hybridoma and Hybridomics , 23* (3):151-159.

Rakha, E., Reis-Filho, J., & Ellis, I. (2010). Combinatorial biomarker expression in breast cancer. *Breast Cancer Research and Treatment , 120*: 293–308.

Rausch, D., & Hendrick, E. (2006). How to Optimize Clinical BreastMRImaging Practices and Techniques on Your 1.5-T System. *RadioGraphics , 26*: 1469–1484.

Reddick, W., Wang, S., Xiong, X., Glass, J., Wu, S., Kaste, S., et al. (2001). Dynamic Magnetic Resonance Imaging of Regional Contrast Access as an Additional Prognostic Factor in Pediatric Osteosarcoma. *Cancer* , 2230-2237.

Reshkin, S., Bellizzi, A., Caldeira, S., Albarani, V., Malanchi, I., Poingnee, M., et al. (2000). Na+/H+ exchanger-dependent intracellular alkalinization is an early event in malignant transformation and plays an essential role in the development of subsequent transformation associated. *The FASEB Journal , 14*: 2185 - 2197.

Rhyner, M., Smith, A., Gao, X., Mao, H., Yang, L., & Nie, S. (2008). Quantum Dots and Targeted Nanoparticle Probes for In Vivo Tumor Imaging. In J. Bulte, & M. Modo, *Nanoparticles in Biomedical Imaging - Emerging Technologies and Applications* (pp. 413-425). UK: Springer Science.

Russell, M., & Anzai, Y. (2007). Ultrasmall superparamagnetic iron oxide enhanced MR imaging for lymph node metastases. *Radiography , 13*: 73-74.

Rutkaite, R., Swanson, L., Li, Y., & Armes, S. (2008). Fluorescence studies of pyrene-labelled, pH-responsive diblock copolymer micelles in aqueous solution. *Polymer , 49*: 1800-1811.

Saloutia, M., Rajabia, H., Babaeib, M., & Rasaeec, M. (2008). Breast tumor targeting with 99mTc-HYNIC-PR81 complex as a new biologic radiopharmaceutical. *Nuclear Medicine and Biology , 35*: 763–768.

Samphao, S., Wheeler, A., Rafferty, E., Michaelson, J., Specht, M., Gadd, M., et al. (2009). Diagnosis of breast cancer in women age 40 and younger:delays in diagnosis result from underuse of genetic testing and breast imaging. *The American Journal of Surgery , 198*: 538–543.

Schneider, B., & Miller, K. (2005). Angiogenesis of Breast Cancer. *Journal of Clinical Oncology , 23* (8): 1782-1790.

Schroeder, J., Adriance, M., Thompson, M., Camenisch, T., & Gendler, S. (2003). MUC1 alters b-catenin-dependent tumor formation and promotes cellular. *Oncogene , 22*: 1324 –1332.

Schroeder, J., Masri, A., Adriance, M., Tessier, J., Kotlarczyk, K., Thompson, M., et al. (2004). MUC1 overexpression results in mammary gland tumorigenesis and prolonged alveolar differentiation. *Oncogene , 23*: 5739–5747.

Simms, M. P., Price, M., Scholfield, H., & Bishop, M. (2001). 99mTechnetium-C595 radioimmunoscintigraphy: a potential staging tool for bladder cancer. *British Journal of Urology International , 88:* 686-691.

Singh, R., & Bandyopadhyay, D. (2007). MUC1: A target molecule for Cancer Therapy. *Cancer Biology and Therapy , 6* (4):481-486.

Smart, C., Hendrick, R., Rutledge, J., & Smith, R. (1995). Benefit of Mammography Screening in Women Ages 40 to 49 Years. *Cancer , 75* (7): 619-626.

Song, E., Qu, C., Rizvi, S., Raja, C., Beretov, J., Morgenstern, A., et al. (2008). Bismuth-213 radioimmunotherapy with C595 anti-MUC1 monoclonal antibody in an ovarian cancer ascites model. *Cancer Biology and Therapy , 7* (1):76-69.

Sood, A. (2009). PDEF and PDEF-induced proteins as candidate tumor antigens for T cell and antibody-mediated immunotherapy of breast cancer. *Immunologic Research* , 1-10.

Sorlie, T., Perou, C., Tibshirani, R., Aas, T., Geisler, S., Johnsen, H., et al. (2001). Gene expression patterns of breast carcinomas distinguish tumor subclasses with clinical implications. *PNAS , 98* (19): 10869–10874.

Stenzel, H. (2008). RAFT polymerization: an avenue to functional polymeric micelles for drug delivery. *Chemical Communications* , 3486–3503.

Suzuki, F., Akimoto, Y., Sasai, K., & Yajima, H. (2003). Cellular radiosensitivity and cell-type-specific activation of apoptosis signaling pathways. *International Congress Series , 1258*: 233– 237.

Tiefenauer, L. (2007). Magnetic Nanoparticles as Contrast Agents for Medical Diagnosis. In T. Vo-Dinh, *Nanotechnology in Biology and Medicine: Methods, Devices and Applications* (pp. 1-20). USA: Taylor and Francis Group.

Torchilin, V. (2007). Micellar Nanocarriers: Pharmaceutical Perspectives. *Pharmaceutical Research , 24* (1): 1-16.

Torchilin, V. (2001). Structure and design of polymeric surfactant-based drug delivery systems. *Journal of Controlled Release , 73*: 137–172.

Turnbulla, L. (2009). Dynamic contrast-enhanced MRI in the diagnosis and management of breast cancer. (W. InterScience, Ed.) *NMR in Biomedicine , 22*: 28–39.

Vermeer, P., Einwalter, L., Moninger, T., Rokhlina, T., Kern, J., Zabner, J., et al. (2003). Segregation of receptor and ligand regulates activation of epithelial growth factor receptor. *Nature , 422*: 322-326.

Villablanca, E., Zhou, D., Valentinis, B., Negro, A., Raccosta, L., Mauri, L., et al. (2008). Selected natural and synthetic retinoids impair CCR7- and CXCR4-dependent cell migration in vitro and in vivo. *Journal of Leukocyte Biology , 84*: 1-9.

Walsh, M., Luckie, S., Cummings, M., Antalis, T., & McGuckin, M. (2000). Heterogeneity of MUC1 expression by human breast carcinoma cell lines in vivo and in vitro. *Breast Cancer Research and Treatment , 58*: 255–266.

Wang, A., Bagalkot, V., Gu, F., Alexis, F., Vasilliou, C., Cima, M., et al. (2007). Novel Targeted Aptamer-superparamagnetic Iron Oxide Nanoparticle Bioconjugates for Combined Prostate Cancer Imaging and Therapy. *International Journal of Radiation Oncology , 69* (3): 110-111.

Weishaupt, D., Kochli, V., & Marincek, B. (2006). *How does MRI work? - An introduction to the physics and function of Magnetci Resonance Imaging* (2nd ed.). Germany: Springer.

Weissleder, R. (2002). Scaling Down Imaging: Molecular Mapping of cancer in mice. *Nature Reviews - Cancer , 2*: 1-8.

Weissleder, R., & Mahmood, U. (2001). Molecular Imaging. *Radiology , 219*: 316–333.

Westbrook, C., & Kaut, C. (2000). *Ressonância Magnética Prática* (2nd ed.). Brasil: Guanabara Koogan.

Winter, P., Caruthers, S., Kassner, A., Harris, T., Chinen, L., Allen, J., et al. (2003). Molecular Imaging of Angiogenesis in Nascent Vx-2 Rabbit Tumors Using a Novel avB3-targeted Nanoparticle and 1.5 Tesla Magnetic Resonance Imaging. *Cancer Research , 63*: 5838–5843.

Winter, P., Caruthers, S., Schmieder, A., Neubauer, A., Lanza, G., & Wickline, S. (2008). Molecular MR Imaging with Paramagnetic Perfluorocarbon Nanoparticles. In J. Bulte, & M. Modo, *Nanoparticles in Biomedical Imaging - Emerging Technologies and Applications* (pp. 163-182). USA: Springer Science.

Xing, Z., Chang, Y., & Kang, I. (2010). Immobilization of biomolecules on the surface of inorganic nanoparticles for biomedical applications. *Science and Technology of advanced materials , 11*: 1-17.

Xiong, C., Natarajan, A., Shi, X., Denardo, G., & Denardo, S. (2006). Development of tumor targeting anti-MUC-1 multimer: effects of di-scFv unpaired cysteine location on PEGylation and tumor binding. *Protein Engineering, Design & Selection , 19* (8): 359–367.

Yan, L., Mao, H., Wang, Y., Cao, Z., Peng, X., Wang, X., et al. (2009). Single Chain Epidermal Growth Factor Receptor Antibody Conjugated Nanoparticles for in vivo Tumor Targeting and Imaging. *Small , 5* (2): 235–243.

Yezhelyev, M., Gao, X., Xing, Y., Al-Hajj, A., Nie, S., & O'Regan, R. (2006). Emerging use of nanoparticles in diagnosis and treatment of breast cancer. *Lancet Oncology , 7*: 657-667.

Young-wook, J., Jae-Hyun, L., & Jinwoo, C. (2007). Nanoparticle Contrast Agents for Molecular Magnetic Resonance Imaging. In C. Mirkin, & C. Niemeyer, *Nanobiotechnology II: More concepts and Applications* (pp. 321-346). Germany: Wiley-VCH.

Yuan, F., Dellian, M., Fukumura, D., Leunig, M., Berk, D., Torchilin, V., et al. (1995). Vascular Permeability in a Human Tumor Xenograft: Molecular Size Dependence and Cutoff Size. *Cancer Research , 55*: 3752-3756.

Yuan, F., Leunig, M., Huang, S., Berk, D., Papahadjopoulos, D., & Jam, R. (1994). Microvascular Permeability and Interstitial Penetration of Sterically Stabilized (Stealth) Liposomes in a Human Tumor Xenograft. *Cancer Research , 54*: 3352-3356.

Zarabi, B., Nan, A., Zhuo, J., Gullapalli, R., & Ghandehari, H. (2008). HPMA Copolymer–Doxorubicin–Gadolinium Conjugates: Synthesis, Characterization,and in vitro Evaluation. *Macromolecular Bioscience , 8*: 741–748.

Zhang, G., Zhang, R., Wen, X., Li, L., & Li, C. (2008). Micelles Based on Biodegradable Poly(L-glutamic acid)-b-Polylactide with Paramagnetic Gd Ions Chelated to the Shell Layer as a Potential Nanoscale MRI-Visible Delivery System. *Biomacromolecules , 9* (1): 36–42.

Zhang, S., Li, J., Lykotrafitis, G., Bao, G., & Suresh, S. (2009). Size-Dependent Endocytosis of Nanoparticles. *Advanced Materials , 21*: 419–424.

Zhang, S., Wu, K., & Sherry, A. (1999). A Novel pH-Sensitive MRI Contrast Agent. *Angewandte Chemie International Edition , 38*: 3192-3194.

Zhao, Q., Guo, W., Nash, G., Stone, P., Hilkens, J., Rhodes, J., et al. (2009). Circulating Galectin-3 Promotes Metastasis by Modifying MUC1 Localization on Cancer Cell Surface. *Cancer Research , 69* (17): 6799-6806.

APPENDIX A

Concentration, purity and quality of RNA isolated from MDA-MB-468, MCF-7, Hela, ARPE19, D407 and 293T cancer cell lines.

Tabela 2: Concentration and purity of RNA.

Cell Line	RNA (ng/µL)	A_{260}/A_{280}
MDA-MB-468	1437.3	1.89
MCF-7	1313.3	1.87
Hela	679.0	1.79
ARPE19	620.5	1.83
D407	1347.1	1.90
293T	2959.4	1.94

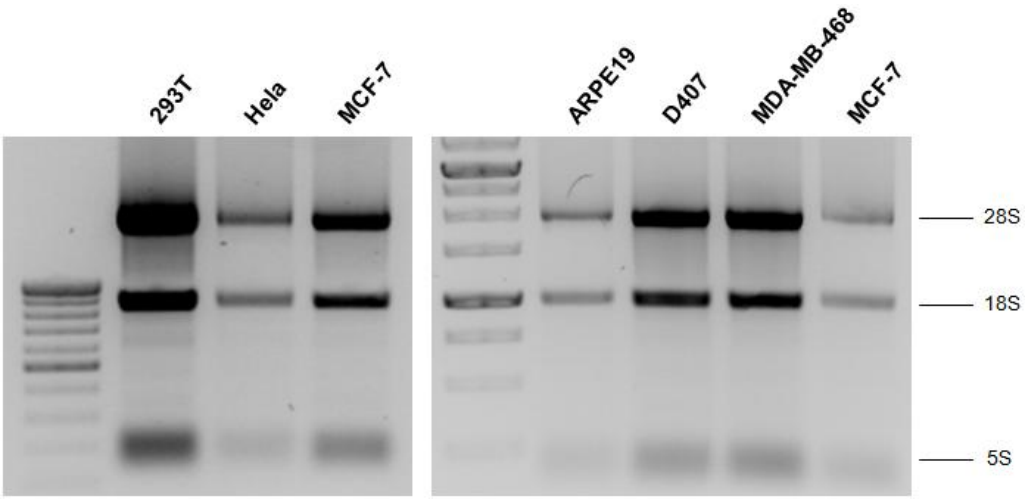

Figure 27 – Visualization of RNA ribosomal bands (28S, 18S and 5S) to assess the quality of RNA isolated from MDA-MB-468, MCF-7, Hela, ARPE19, D407 and 293T cancer cell lines.

APPENDIX B

Detection of α-tubulin in MCF-7 breast cancer cells and DND41 acute lymphoblastic leukemia cells by Western blotting.

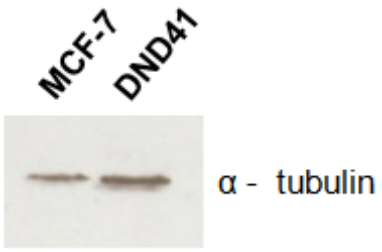

Figure 19 – Detection of α–tubulin protein in homogenates of MCF-7 and DND41 cell lines by SDS-PAGE and Western Blotting.